Seebeck coefficient in organic semiconductors

A dissertation submitted for the degree of Doctor of Philosophy

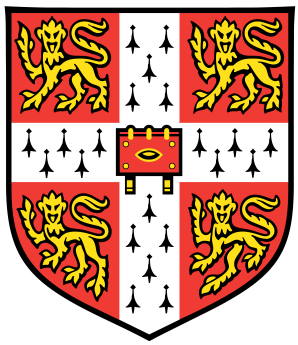

Deepak Venkateshvaran

Fitzwilliam College

&

Optoelectronics Group, Cavendish Laboratory

University of Cambridge

February 2014

"The end of education is good character"

SRI SATHYA SAI BABA

To my parents, Bhanu and Venkatesh,
for being there...always

Acknowledgements

I remain ever grateful to Prof. Henning Sirringhaus for having accepted me into his research group at the Cavendish Laboratory. Henning is an intelligent and composed individual who left me feeling positively enriched after each and every discussion. I received much encouragement and was given complete freedom. I honestly cannot envision a better intellectually stimulating atmosphere compared to the one he created for me. During the last three years, Henning has played a pivotal role in my growth, both personally and professionally and if I ever succeed at being an academic in future, I know just the sort of individual I would like to develop into.

Few are aware that I came to Cambridge after having had a rather intense and difficult experience in Germany as a researcher. In my first meeting with Henning, I took off on an unsolicited monologue about why I was so unhappy with my time in Germany. To this he said, "Deepak, now that you are here with us, we will try our best to make the situation better for you". Henning lived up to this word in every possible way.

Three years later, I feel reinvented. I feel a constant sense of happiness and contentment in my life together with a renewed sense of confidence in the pursuit of academia. For this and more, I shall remain always thankful to Henning.

I also acknowledge and thank Prof. David Emin at the University of New Mexico for his continuous input in helping me explain my scientific results. Although I have not met him in person yet, our correspondence via email has been regular and I attribute a substantial amount of my current knowledge about polarons and charge transport in disordered semiconductors to him. My collaboration with him has been tremendously fulfilling.

Dr. Auke Jisk Kronemeijer was great support for me during my time as a PhD student. Although just a year older than I am, his understanding about charge transport in organic semiconductors was far more comprehensive than my own, and the discussions I had with him helped me make significant progress, quickly. Auke knew about my aspirations to be an academic in future and since publications remain a currency of one's success in academia, he let me get involved in his work so that I could eventually share authorship on papers that he wrote. Academia would be a wonderful environment if each of us bolsters the ambitions of our colleagues, just as Auke did for me.

The support of my mentor and friend in the United Kingdom, Ishver Patel, remains invaluable. Ishver has seen me grow since the time I was little, and has always helped me put a positive spin on my life's experiences.

My extended family in the United Kingdom, Uncle Cumar, Aunty Ranee, Vignesh and Rahul Patel, went out of their way to help me feel settled here. With them in London, I have always felt that there is a home for me within driving distance to go back to. I have been helped by them in ways so many, it has become hard to quantify. Although I know that I may never be able to repay their selfless kindness, I genuinely wish to be able to pay it forward.

I am also indebted to Pritesh Hiralal, a close friend in Cambridge who was there to constantly reassure me that my life was on the right track whenever I got into one of my moods of regret. As third culture adults, we relate to our cultural home India in very similar ways, and he is one of few who completely understood my constant difficulty when posed with the question "Where do you come from?". I am also thankful to him for taking care of all the administrative needs of the flat that we shared in Cambridge. My life was made very easy thanks to his help.

Cambridge has been a very fulfilling experience on all fronts and I have made some excellent friends while here. I have many to thank both at Fitzwilliam College as well as at the Cavendish Laboratory. This list is far from comprehensive but few of those with whom I have shared some excellent times are Tiago Costa, Matt Neal, Yunuen Montelongo, Andreas Teriete, Thomas Strobel, John Moriarty, Carlo Tarantini, Iyad Nasrallah, Mark Nikolka, Chris Warwick, Sai Giridhar Shivareddy, Antony Sou, Vincenzo Pecunia and Lang Jiang.

Special thanks go to Kal Banger, Nick Lambert and Tom Kehoe, postdoctoral friends from work who were more like brothers to me, as well as George Nikiforov and Radoslav Chakalov with whom I shared long hours in the cleanroom. I reckon I may have given Rad the impression that I lived in the Microelectronics Research Center. Well, I didn't!

I also remain very thankful to Mi Jung Lee, whose cheerful attitude to life I found quite contagious. Getting to know her better gave me the chance to look at life in ways I never have before. Mi Jung went on to become a professor in South Korea and I hope she continues to be successful in what she does.

A mention must be made of the good times I enjoyed with Stephen Scott-Fawcett, a dynamic man with unbelievably entertaining life stories. Stephen went out of his way to introduce me to all things quintessentially English, an act for which I shall remain very thankful. He is a man with a big heart, and great dreams for a better world. I really consider myself lucky having met him in Cambridge.

My spiritual mentor, Sri Sathya Sai Baba, has played a key role in the sort of person I have grown up to become. Sri Sathya Sai Baba passed away during the course of my PhD, but his message of the five human values; Love, Peace, Righteous Conduct, Non-Violence and Truth continue to guide my personal decisions.

Finally, I am ever grateful to my parents, Bhanu and Venkatesh, and my older brother Ashwin for having filled my life with inexpressible joy and happiness. Having such a close-knit and loving family is the greatest blessing I have been bestowed with.

Deepak Venkateshvaran

Cambridge, 23 November 2013

Abstract

When a temperature differential is applied across a semiconductor, a thermal voltage develops across it in response. The ratio of this thermal voltage to the applied temperature differential is the Seebeck coefficient, a transport coefficient that complements measurements of electrical and thermal conductivity. The physical interpretation of the Seebeck coefficient is the entropy per charge carrier divided by its charge and is hence a direct measurement of the carrier entropy in the solid state.

This PhD thesis has three major outcomes. The first major outcome is a demonstration of how the Seebeck coefficient can be used as a tool to quantify the role of energetic disorder in organic semiconductors. To this end, a microfabricated chip was designed to perform accurate measurements of the Seebeck coefficient within the channel of the active layer in a field-effect transistor (FET). When measured within an FET, the Seebeck coefficient can be modulated using the gate electrode. The extent to which the Seebeck coefficient is modulated gives a clear idea of charge carrier trapping and the distribution of the density of states within the organic semiconductor.

The second major outcome of this work is the observation that organic semiconducting polymers show Seebeck coefficients that are temperature independent and strongly gate voltage modulated. The extent to which the Seebeck coefficient is modulated in the polymer PBTTT is found to be larger than that in the polymer IDTBT. Taken together with conventional charge transport measurements on IDTBT, the voltage modulated Seebeck coefficient confirms the existence of a vanishingly small energetic disorder in this material.

In the third and final outcome of this thesis, the magnitude of the Seebeck coefficient is shown to be larger for organic small molecules as compared to organic polymers. The basis for this is not yet clear. There are reports that such an observation is substantiated through a larger contribution from vibrational entropy that adds to the so called entropy-of-mixing contribution so as to boost the magnitude of the Seebeck coefficient in organic small molecules. As of now, this remains an open question and is a potential starting point for future work.

The practical implications of this PhD thesis lie in building cost-effective and environmentally friendly waste-heat to useful energy converters based on organic polymers. The efficiency of heat to energy conversion by organic polymers tends to be higher than that for conventional semiconductors owing to the presence of narrow bands in organic polymer semiconductors.

Structure of this PhD thesis

This thesis has been designed and written in a way by which each subsequent Chapter latches on to ideas presented in the preceding Chapters, in an attempt to build a comprehensive picture of charge transport studied from a Seebeck coefficient standpoint.

Chap. 1 introduces established ideas from thermoelectrics and charge transport in organic semiconductors. Chap. 2 illustrates the design of the microfabricated chip using which gate-modulated Seebeck coefficient measurements are performed on solution processed organic semiconductors in this thesis. Chap. 3 documents the outcome of gate-modulated Seebeck coefficient measurements on the polymer PBTTT, and provides two possible explanations for the observations based on the theory laid out in Chap. 1. Chap. 4 is a demonstration of how the Seebeck coefficient is a conclusive probe of an ultra low degree of energetic disorder within the high mobility polymer IDTBT. This chapter compares IDTBT with PBTTT and the ambipolar polymer PSeDPPBT showing how disorder can manifest itself as trends in the Seebeck coefficient. Chap. 5 shows that a measurement of the Seebeck coefficient in the ambipolar polymer PSeDPPBT has signatures from both holes and electrons. Chap. 6 is written to be a speculative attempt at building a universal picture of how measurements of the activation energy combined with the gate-modulated Seebeck coefficient within a field effect transistor build a case for trap-free transport in organic semiconductors, and establish conditions under which band-like transport is likely. Finally, Chap. 7 summarises the important conclusions that are drawn based on the collective experimental observations contained in this thesis.

Funding for this PhD thesis

Between October 2010 and September 2013, My PhD studies at the University of Cambridge were funded entirely through a Cambridge International Student Scholarship (CISS), a gift from the Cambridge Commonwealth Trust for which I shall remain ever grateful. Between October and December 2013, during the writing up period of this thesis, funding in the form of a Lundgren Research Award, a grant from the Fitzwilliam College Hardship Fund and a top-up grant from research funds available to Prof. Henning Sirringhaus, are gratefully acknowledged.

Declaration

Except where specific reference is made to the involvement of others, the work presented herein is my own and contains nothing of which is the result of collaboration. This dissertation has not been submitted in whole or in part for the award of a degree at this, or any other university and does not exceed 60,000 words in length.

Deepak Venkateshvaran

Cambridge, 23 November 2013

Contents

Chapter 1

Introduction

1.1 Thermoelectrics

Thermoelectrics concerns itself with the conversion of heat into electricity. Since heat is a by-product of every electronic and mechanical process, the search for efficient solutions to scavenge the uncontrolled dissipation of heat and convert it into useful energy using high performance thermoelectric materials remains a priority. Complementary thermoelectric generators that function in tandem with conventional heat engines have the potency to increase the overall efficiency of an energy generation process above what the heat engine would have had having worked alone. An example of this is the thermoelectric generator developed by BMW to harvest waste heat from a vehicle's exhaust. Back in 2003, BMW developed a thermoelectric generator capable of generating a power of 80 W from a vehicle's exhaust. In 2011, with improved design and superior thermoelectric materials, BMW demonstrated a 600 W thermoelectric generator for use in their X6 luxury crossover. The electrical energy generated using such thermoelectric generators in automobiles are used to power electrical systems within the vehicle, thus improving the fuel economy. The present target in the automotive sector is an improvement of 10 % in the fuel economy by a concomitant use of high performance thermoelectric generators.

Although the automotive sector's use of thermoelectrics has been the most prominent in the last few years, thermoelectric generators have been very successful in powering our interest in space exploration for decades. As an example, Radioisotope Thermoelectric Generators (RTGs) convert the heat accompanying a nuclear fission process into electrical energy capable of powering a spacecraft. Such an RTG was used in NASA's *Voyager* launched in 1977. Although *Voyager* is now beyond the confines of our solar system, it continues to operate till this day, 36 years later, beaming back data to the Deep Space Network. The Mars rover *Curiosity* launched in 2011 to assess Martian climate and geology also makes use of an RTG to power its onboard electronics. The RTG on *Curiosity*, shown in Fig. 1.1, is an improved version over that used in *Voyager*. It makes use of lead telluride (PbTe) together with tellurides containing antimony, germanium, and silver (TAGS) to harness between 100 and 125 W from Pu-238 fuel pellets [1]. The conversion efficiency of radioisotope heat to electrical energy in these RTGs is normally between 5-9 % [2].

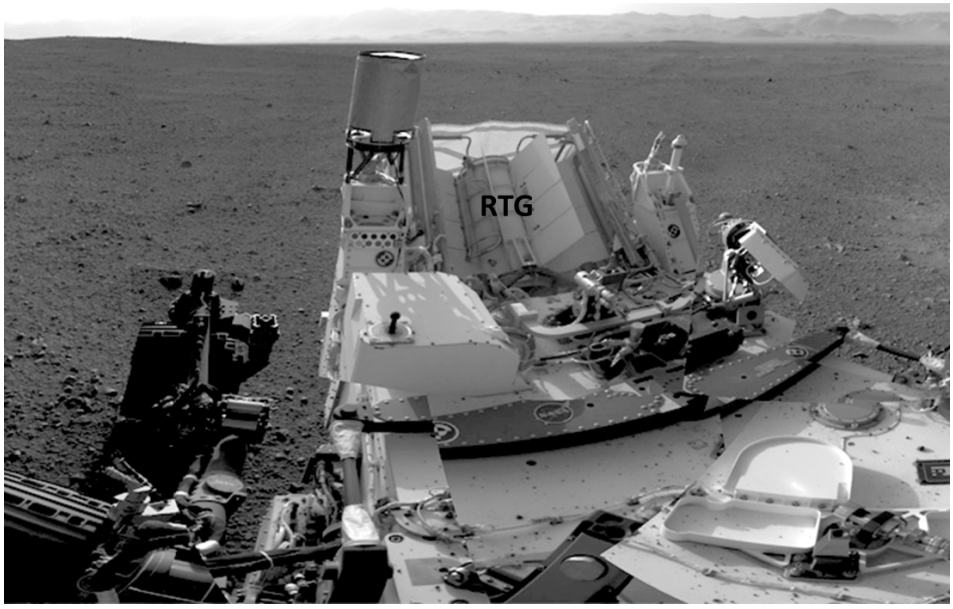

Figure 1.1: Self-portrait of the Mars rover *Curiosity*. The finned barrel shown with the label 'RTG' is the Radioisotope thermoelectric generator on board the rover that runs on improved thermoelectric materials based on PbTe/TAGS.

Applications for thermoelectrics such as those mentioned above are constantly growing, as we pursue all possible pathways to address the need for efficient energy usage on our planet. It hence comes as no surprise that the global market for thermoelectric heat harvesters was recently forecast to be valued at $875 million by 2023, a forecast made by the Cambridge based market research firm IDTechEx in June 2013 [3].

A key quantifiable property in judging the suitability of a proposed thermoelectric material in commercial devices is called the thermoelectric figure of merit ZT,

$$ZT = \frac{\alpha^2 \sigma T}{\kappa}. \tag{1.1}$$

Here, α is a transport coefficient known as the Seebeck coefficient, σ is the electrical conductivity, κ the thermal conductivity and T, the temperature. κ in turn includes two contributions, an electronic contribution and a lattice contribution. Most commercial grade thermoelectric materials today have a ZT that hovers around 1 at 300 K. Interestingly enough, in a review article by Kanatzidis and co-workers published recently [4], it was shown that between 1950 and 2010 there were only stray conclusive accounts of breaking this $ZT = 1$ barrier. This is because in most conventional materials, metals and semiconductors, the electrical conductivity σ is tied to the electronic component of the thermal conductivity κ through the Wiedemann-Franz law [5]. The lattice contribution is weak in comparison to the electronic contribution to the thermal conductivity. Thus, increasing σ creates a proportionate increase in κ so as to clamp the value of ZT. An approach to increase the value of ZT has hence been to try and achieve a phonon-glass electron-crystal behaviour within a thermoelectric material. What this means is that the material should behave like a glass with a small thermal conductivity κ when it

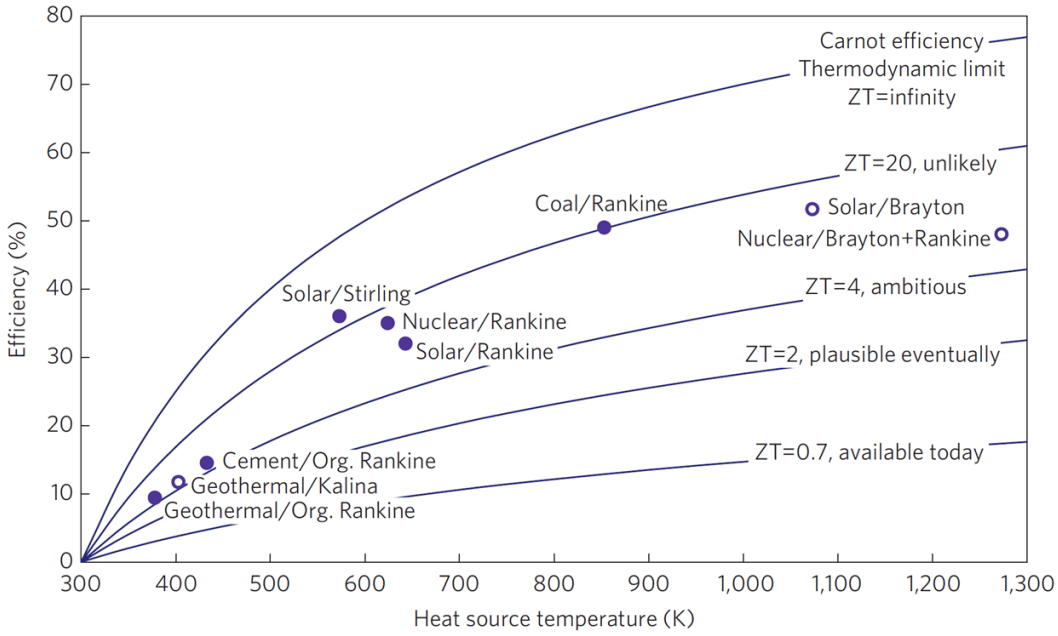

Figure 1.2: Efficiency of thermoelectrics with different figures of merit ZT compared to the performance of conventional heat engines. Image adapted from [10].

comes to heat transport, but should simultaneously behave crystal-like with a high electrical conductivity σ.

Nanostructured thermoelectrics with artificially fabricated superlattices of thermoelectric materials is a promising candidate in achieving a phonon-glass electron-crystal behaviour owing to the raised probability of phonon scattering at the interfaces within the superlattice [6, 7, 8]. Venkatasubramanian and co-workers showed that using a superlattice composed of bismuth and antimony telluride Bi_2Te_3/Sb_2Te_3, the figure of merit ZT could be raised to 2.4 at 300 K, one of the highest values ever reported [7]. Nanostructuring thermoelectric materials into superlattices helps scatter phonons whose mean free paths are on the order of the periodicity of the superlattice. Although very effective in scattering a part of the phonon spectrum to reduce the thermal conductivity and increase ZT, there are still phonons with large mean free paths that remain unscattered. A paradigm for an improved ZT that adopts a panoscopic approach to scattering of phonons of both large and small mean free paths is through an incorporation of nano and mesoscale precipitates within the bulk of a conventional thermoelectric material like lead telluride, PbTe. Using this panoscopic approach, values in excess of $ZT = 2$ were demonstrated at 900 K [9].

Additional paradigms that do not involve nanostructuring have recently emerged that help achieve a $ZT > 1$. Snyder and co-workers, in their recent work "Copper ion liquid-like thermoelectrics" show that complex crystal structures such as Copper chalcogenides show $ZT = 1.6$ at 1000 K in the bulk phase since the crystal stucture of $Cu_{2-x}Se$ intrinsically acts as an ideal phonon-impeding and electron-enabling medium [11]. As of 2013, the regime for which the

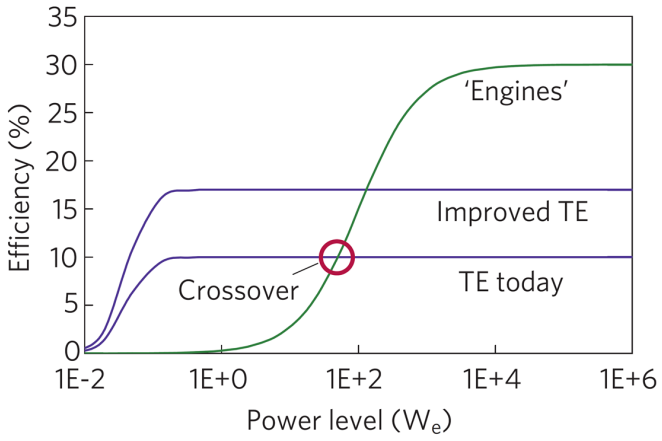

Figure 1.3: Size favours thermoelectrics. For low power requirements on the order of a few mW, the efficiencies of thermoelectric devices outweigh those of conventional large scale engines. Image adapted from [10].

thermoelectric figure of merit $ZT > 3$ remains largely unexplored and has proven very difficult to reach.

Much like a heat engine, a thermoelectric device operates between two temperatures T_{hot} and T_{cold}. The efficiency of heat to electricity conversion in terms of ZT for a thermoelectric is given by

$$\text{Efficiency}(\eta) = \frac{T_{\text{hot}} - T_{\text{cold}}}{T_{\text{hot}}} \times \frac{\sqrt{1+ZT}-1}{\sqrt{1+ZT}+T_{\text{cold}}/T_{\text{hot}}}. \tag{1.2}$$

The efficiency is thus boosted when ZT is as large as possible and the temperature difference across the thermoelectric is maximum. Fig. 1.2 compares the performance of conventional mechanical heat engines to thermoelectric "engines" having different ZT values. It is evident from Fig. 1.2 that with the current state of the art performance $ZT = 1$, the conversion efficiencies are only a few % around 300 K. They begin to approach 10 % around 900 K which is promising, but at the same time not so promising considering that most heat generated by our personal gadgets is not at an industrial scale, and remains low grade heat typically 10s of °C beyond room temperature. It will take an Apollo-like effort to find new paradigms that break the $ZT = 4$ barrier to make thermoelectric technology compete with solar and nuclear rankine engines. As of the moment however, $ZT = 3$ remains the ultimate goal for thermoelectrics and although plausible, has no well defined path to be achieved.

Despite the prospect of thermoelectrics being far from a gifted technology that can play a dominant role in addressing our need for better energy efficiency, scale and specificity are obvious advantages to this technology. As shown in Fig. 1.3, when small powers are needed, thermoelectrics proves to be a better solution than a conventional heat engine. It is only when powers greater than 100 W are required that thermoelectrics begins to fall behind. Size also favours thermoelectrics. As an example, on-chip spot cooling of electronic devices by upto 15 °C can be achieved using thermoelectric coolers [12]. Thermoelectric devices also include no

mechanical parts and tend to be very silent, another plus point for the technology.

Organic semiconductors have been a rather late entrant into the field of thermoelectrics. By virtue of their intrinsic weak van der Waals bonding, organic semiconductors will decompose at temperatures > 400 °C, a temperature regime where most conventional thermoelectrics perform best [13]. Nevertheless, they have shown extremely good promise so far, evidenced by a room temperature $ZT = 0.42$ in the case of the conducting polymer poly(3,4-ethylenedioxythiophene) doped with poly(styrenesulphonate) (PEDOT:PSS) [14]. In an alternate report on PEDOT, its ZT value was controlled depending on its oxidation level, achieving a maximum of $ZT \approx 0.25$ [15]. There are not many reports documenting ZT in many organic polymer semiconductors and small molecules. This said, first principles electronic structure calculations coupled with Boltzmann transport theory was recently used to model the thermoelectric properties of a few molecular semiconductors such as pentacene and rubrene. The predicted ZT values from these simulations were between 0.8 and 1.8 for pentacene at temperatures near room temperature, rivaling some of the best performing inorganic thermoelectrics [16]. The two salient features that distinguish organic semiconductors from inorganic semiconductors and help them perform well from a ZT standpoint are (a) a low thermal conductivity as a consequence of disorder [17] and (b) a narrow band density of states (DOS) [16]. It is also of significance to note that the Wiedemann-Franz law plays a rather unimportant role in clamping the value of ZT in organic semiconductors since the contribution to κ from the lattice thermal conductivity dominates the electronic contribution.

Although a quantification of ZT is important to understand the practical implications and viability of organic semiconductors for thermoelectrics, a complete understanding of one of its constituent parameters, the Seebeck coefficient α, is of equal priority. The Seebeck coefficient in organic semiconductors is a direct probe into the microscopic charge transport mechanisms at play, and an understanding of the physics of the Seebeck helps one re-engineer organic thermoelectric device performance to maximise their commercial viability.

The motivation of the work presented in this thesis has from its early beginnings been to understand the physics of charge transport in organic semiconductors from a standpoint of the Seebeck coefficient and not just a quantification of ZT, important as that might be considered by some.

1.2 Organic semiconductors

Organic semiconductors are a class of materials comprising carbon based molecules and polymers. Of key importance to the performance of organic semiconductors in the electronics industry is the property of π-conjugation that characterises these materials. Rings of carbon atoms with alternating carbon double bonds are associated with π-orbitals that overlap to form a delocalised electron cloud above and below them. Charge transport within π-conjugated organic materials takes place through the delocalised cloud, along the material's backbone. Unlike inorganic semiconductors such as silicon where the atoms that comprise the lattice are covalently bonded, organic semiconducting polymers and molecules are weakly held together in the lattice

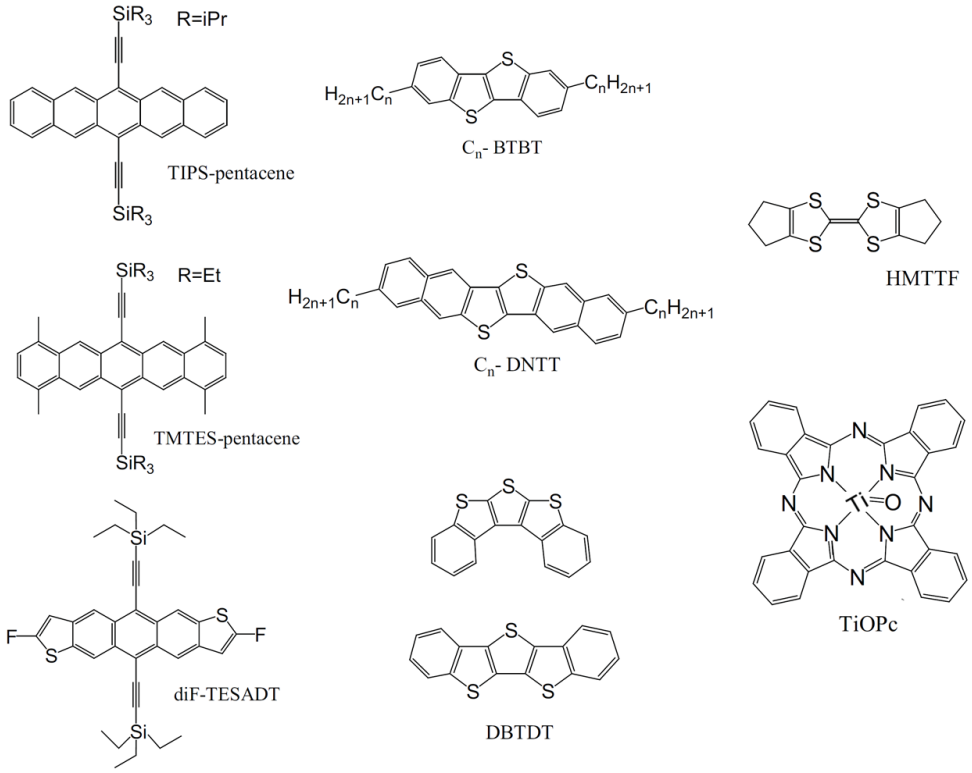

Figure 1.4: Selected forms of organic molecular semiconductors. Image adapted from [21].

by van der Waals interactions as noted earlier. The consequences of this type of bonding reflects itself as reduced hardness, lower melting point and weaker delocalisation of the electronic wavefunction across concomitant molecules in the lattice [18]. Akin to valence and conduction bands in conventional inorganic semiconductors, organic semiconductors have two energy bands called the highest occupied molecular orbital (HOMO) and lowest unoccupied molecular orbital (LUMO) [18, 19]. The HOMO and LUMO levels are but the bonding and anti-bonding orbitals of the π-conjugated cloud. These energy bands do not represent a continuum of energy levels, but rather a set of discrete levels close enough to each other to facilitate charge carrier hopping between them. The HOMO and LUMO levels in organic semiconductors are broadened by disorder into a Gaussian band that has a bandwidth on the order of 0.1 eV. This is in contrast to conventional inorganic semiconductors where the equivalent bandwidth is on the order of 1 to 10 eV. [20]. It is for this reason that organic semiconductors are sometimes referred to as narrow bandwidth systems. Fig. 1.4 and Fig. 1.5 show some examples of π-conjugated organic molecular semiconductors and organic polymer semiconductors, respectively, that are in routine use. Many of these structures contain atoms such as sulphur (S) as well as substituted alkyl chains that are known to affect intermolecular packing within the crystal and solubility in solution.

Organic semiconductors benefit from their ability to be processed into active layers for electronic devices from solution at comparatively low temperatures [22]. The ability to deposit organic semiconductors using conventional printing methods has also attracted interest in them. Although organic semiconductors might never be empowered to the extent where they dominate

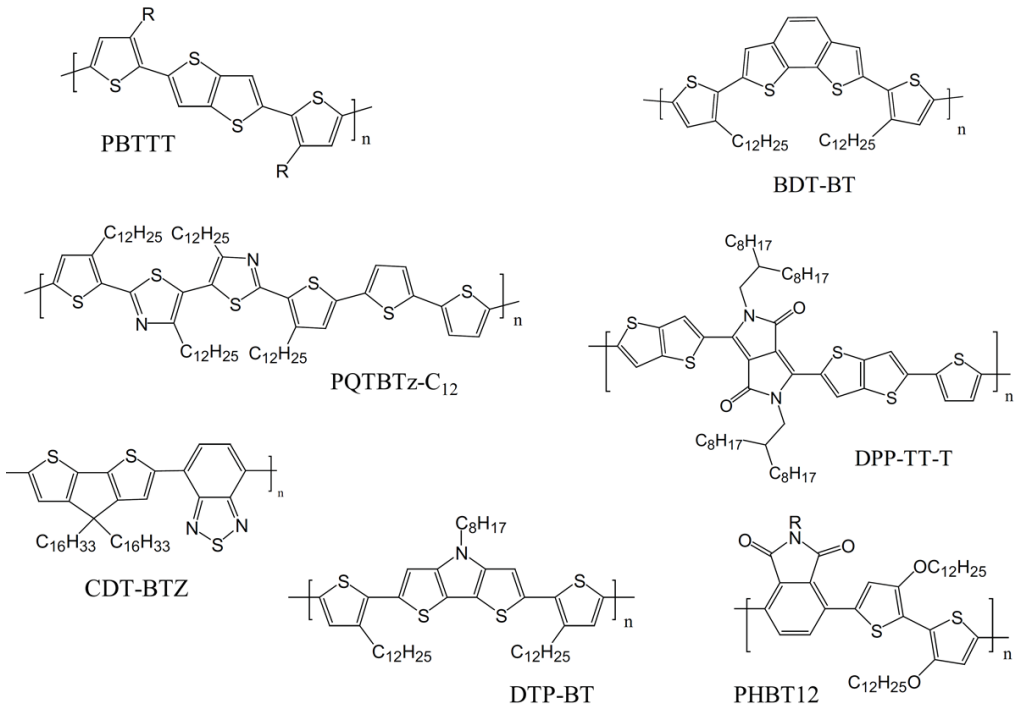

Figure 1.5: Selected forms of organic polymer semiconductors. Image adapted from [21].

the electronics industry, it is hoped that devices based on them would be complementary, due to their ability to suit applications where the use of silicon proves impractical. Two demonstrated examples of such applications are large area bendy displays based on organic light emitting diodes (OLEDs) such as LG's 77-inch Ultra HD curved OLED TV [23] and flexible electronic skin meshed with embedded sensors and actuators [24].

1.3 Organic Field-Effect Transistors

Field-Effect Transistors (FETs) fabricated from organic polymers and small molecules are useful architectures using which the charge carrier mobility within these materials can be measured [25, 22]. Fig. 1.6 shows the schematic of a typical bottom-contact top-gate FET, the architecture used throughout this thesis. The organic semiconductor layer is sandwiched between a substrate and a gate insulator as shown. On application of a voltage at the gate electrode, a conductive channel is created at the interface between the organic semiconductor and the gate dielectric. Under the influence of both a source-drain and gate bias, charge carriers follow the course marked by the dotted line in the Figure. It is of significance to stress that organic semiconductors work in an accumulation mode, where the charge carriers that collect at the interface under a gate field are injected from the metal source and drain electrodes. Unlike FETs based on inorganic semiconductors, organic FETs do not work in an inversion mode owing to the lack of there being free charge carriers within the active organic layer. The source and drain injectors in organic FETs are normally chosen depending on their Fermi level and how

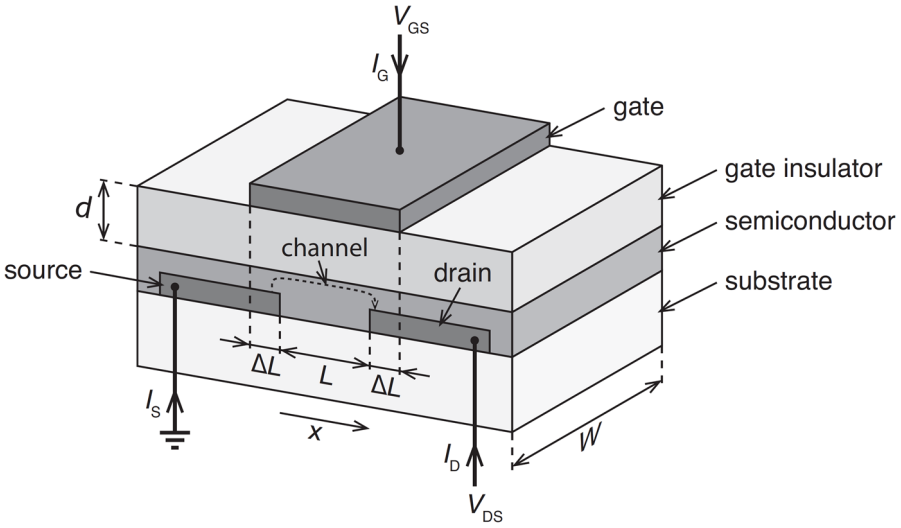

Figure 1.6: Schematic architecture of a bottom-contact top-gate FET. Image adapted from [27].

close it matches with either the LUMO or the HOMO level. If the Fermi level of the metal is close to the HOMO level of the organic semiconductor, holes can be injected into the organic semiconductor with ease. If the Fermi level of the metal is close to the LUMO level of the organic semiconductor, electrons can be injected with ease. If the organic semiconductor has a narrow band-gap and the work-function of the electrodes lies midway between the HOMO and the LUMO, both electrons and holes can be injected into the organic semiconductor depending on the polarity of the gate voltage and the source-drain voltage. Ambipolarity of polymer FETs thus boils down to having a narrow band-gap, ~ 1 eV, with an optimally chosen work-function of the source and drain electrodes [26].

The current voltage characteristics of organic FETs are analysed using the same formalism that governs charge transport in conventional MOSFETs based on silicon. As shown in Fig. 1.7 (a) when the voltage applied to the gate electrode V_{GS} is much larger than the applied voltage between the source and drain V_{DS}, the accumulated carrier concentration at the interface can be considered uniform. In this so called linear regime, the current through the channel is given by

$$I_{D,lin} = \frac{W\mu_{lin}C}{L}(V_{GS} - V_T)V_{DS}. \tag{1.3}$$

W is the channel width, L is the channel length, C is the dielectric capacitance, μ is the mobility and V_T is the threshold voltage of the device. It is customary to apply the voltages V_{GS} and V_{DS} with reference to the source that is kept common. The threshold voltage V_T accounts for the onset of charge accumulation in the channel.

When the applied gate voltage $V_{GS} - V_T$ is equal to the source-drain voltage V_{DS}, the effective voltage between the gate and channel at the drain is zero thus implying zero charge density at this point. The voltage at the source on the other hand is maximum within the channel, thus ensuring the highest charge accumulation there. The point of zero accumulation of charge carrier density is called the pinch-off point shown as P on Fig. 1.7. As long as the applied

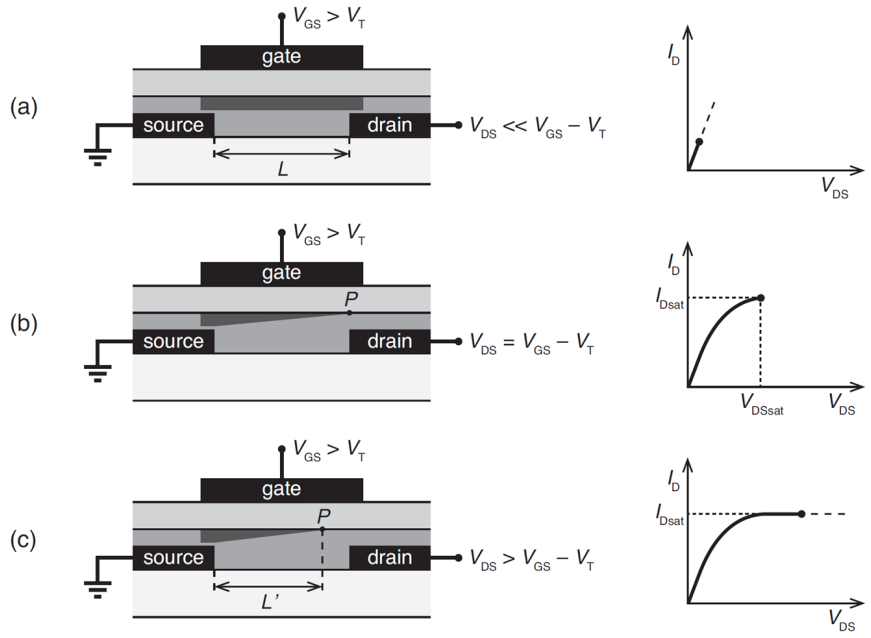

Figure 1.7: Charge distribution within an FET channel under the different operating regimes of the device. (a) the linear regime (b) at the start of saturation, i.e., pinch-off (c) the saturation regime. Image adapted from [27]

source-drain voltage V_{DS} is larger than the applied gate voltage, $V_{\mathrm{GS}} - V_{\mathrm{T}}$, the channel remains pinched-off and the current within the channel remains constant. This transport regime is called the saturation regime. Typical $I_{\mathrm{D}} - V_{\mathrm{DS}}$ characteristics measured under the above circumstances are shown as accompanying figures on the right hand column of Fig. 1.7. In saturation, the current through the channel is given by

$$I_{\mathrm{D,sat}} = \frac{W \mu_{\mathrm{sat}} C}{2L} (V_{\mathrm{GS}} - V_{\mathrm{T}})^2. \tag{1.4}$$

This equation is also used to estimate the threshold voltage within the saturation regime of the FET. The field-effect mobilities derived from the FETs can be measured at various temperatures to extract the *activation energy* responsible for charge transport. In most disordered materials, charge carriers do not move in delocalised energy bands as bloch waves. Rather, they remain localised owing the presence of disorder and hop between localised sites with an average energy known as the activation energy. Among other parameters, the magnitude of the activation energy is an important metric in ascertaining the nature of charge transport within an organic semiconductor.

1.4 Charge transport in organic semiconductors

Charge carrier transport in organic semiconductors is traditionally explained using different frameworks based on the fundamental phenomenon of phonon-assisted carrier hopping between

localised energetic sites. These hopping frameworks can be classified into three categories.

The first, referred to as *polaronic hopping*, takes into account the effects of strong electron-phonon coupling between the charge carrier and its surroundings in the organic semiconductor. It occurs when the so called electronic transfer energies are small enough to facilitate the surrounding atoms' displacement together with the motion of the charge carrier. The activation energy for carrier transport in this case is related to the binding energy of the *polaron*, a quasiparticle whose properties are described in the subsection that will follow.

The second, referred to as *disorder hopping*, discounts the influence of strong electron-phonon coupling. It is based on carrier hopping between energetic sites within an appropriately chosen density of states (DOS) distribution, either an exponential or a Gaussian [28, 29, 19, 30]. A Gaussian DOS is normally adopted when explaining transport in small molecules owing to there being comparatively low energetic disorder, although an exponential DOS has been successfully used to explain transport in both organic small molecules and polymers [30]. The exponential density of states is also sometimes used to model the tail of a Gaussian DOS, thus establishing a link between the two frequently chosen distributions. The activation energy of charge carriers in this model is attributed to the broadening of the density of states as a consequence of static energetic disorder.

The third category of hopping is a concoction of the above two. It involves combining the effects of energetic disorder together with a contribution to the activation energy due to polaron formation [31, 32, 33, 34].

Within the channel of an organic FET, there has been strong experimental evidence for both the presence of energetic disorder from transport measurements [30], as well as the presence of polarons from spectroscopic measurements [35]. The following subsections briefly describe the above mentioned transport models, highlighting their successful predictions as well as their pitfalls.

1.4.1 Polaronic hopping transport

By virture of its mere presence, a localised charge carrier can induce a significant displacement of its surrounding atoms from their equilibrium positions in a solid. This displacement of the surrounding atoms creates a potential well in which the localised charge carrier gets 'self-trapped'. Such a composite quasiparticle self-trapped charge carrier taken together with the polarization cloud that its presence induces on its surrounding is called a *polaron*.

Polarons were first modeled by Holstein in a simplistic 1D molecular crystal [36], a model of which involved three contributions: the lattice, electron and electron-phonon coupling. The lattice component is a sum of harmonic oscillators with the same vibrational frequency. The electron component comes from the electron transfer integral t. When describing the transfer of electrons between two states i and j using quantum mechanical wavefunctions of the two states φ_i and φ_j, the transfer integral is expressed as $t = \langle \varphi_i | V | \varphi_j \rangle$ where V is a perturbation potential. The transfer integral t is proportional to the perturbation. The strength of the electronic coupling

between the initial and final states decides whether the reaction is non-adiabatic or adiabatic. If t is small, hopping is said to be non-adiabatic. As t increases, an energy gap of $2t$ is formed between the higher and lower states and hopping between the two states becomes adiabatic. The electron-phonon coupling contribution is related to the polaron binding energy, E_{P}, which is the energy lowering associated with the deformation of the lattice and the formation of the polarisation cloud. Within approximation, the polaron binding energy $E_{\mathrm{P}} = 2W_{\mathrm{H}}$, where W_{H} is the polaron activation energy.

In π-conjugated organic solids, charge carriers polarise their surroundings too, but the dominant effect comes from the polarisation of the surrounding π-conjugated electron clouds. This principle was illustrated previously by Horowitz in [20] and is reproduced in Fig. 1.8. The π-conjugated molecules are symbolised using hexagonal rings, the vertices of which represent fixed positions of carbon atoms. The circles represent delocalised π-electron clouds over the aromatic carbon rings. The presence of a positive charge on the central molecule causes the delocalised π-electron clouds on the surrounding molecules to get attracted to it, creating an electric dipole that moves together with the positive charge carrier. The spatial shift of the electron clouds from their equilibrium positions are shown using the arrows. If the region over which the displacement is induced in the position of the surrounding atoms (or the polarisation cloud) is short ranged, i.e., on the order of a lattice constant (or the inter-molecular distance), the carrier tends to be severely localised and the resulting polaron is called a small polaron. Polarons fall under two categories, small or *Holstein* polarons [37] and large or *Fröhlich* polarons [38, 39], depending on whether the extent of the accompanying polarisation cloud is on the order of a lattice constant or greater than it, respectively. Although Fröhlich polarons have been observed in organic semiconductors under specific circumstances [40], Holstein polarons are far more common in them [41, 42].

The probability with which polarons are formed in a conducting solid is crucially dependent on its bandwidth. The bandwidth within a solid is an intrinsic measure of how fast charge carriers move within it. This is due to band curvature being inversely proportional to the effective mass of the constrained charge carriers. Narrow band systems are hence associated with "heavy" charge carriers that move slow enough to exercise considerable polarisation on their surroundings thus increasing the probability of polaron formation. A few inorganic crystal systems well known for small polaron formation include crystals of KCl, MnO and UO_2. Organic semiconductors have also demonstrated polaron formation due to their narrow bandwidths, experimentally evidenced through optical absorption [43, 44].

Looked at from a temporal viewpoint, polaron formation is common in organic semiconductors owing to a domination of molecular over crystalline properties stemming from weak van der Waals intermolecular interactions. Giles Horowitz does an excellent back of the envelope calculation in support of polaron formation in organic semiconductors [20]. Horowitz starts by defining two temporal parameters, (a) the residence time τ_{res} which is the time that a charge carrier spends localised on a molecule during transit and (b) the electronic polarisation time τ_{el} which is the time

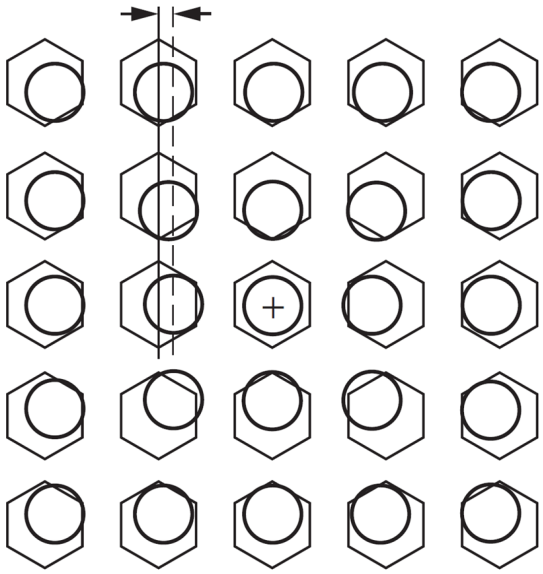

Figure 1.8: Illustration of the formation of an electronic polaron in an organic solid under the presence of a positive charge. The hexagons represent the nuclear cores of the molecules while the circles represent π-conjugated electron clouds. Nuclear polarisation is not included in this graphic, although present in actuality. Image adapted from [20]

it takes for a polarisation cloud to form around the charge. An order of magnitude estimate for the above two quantities can be arrived at by using Heisenberg's uncertainty principle $\tau > \hbar/\Delta E$. When $\Delta E = 0.1$ eV, the typical bandwidth W in organic semiconductors, $\tau_{\text{res}} = 10^{-14}$ s. In an inorganic semiconductor where $W \sim 10$ eV, $\tau_{\text{res}} = 10^{-16}$ s. The electronic polarisation time τ_{el} is calculated based on the time taken for an electronic transition across the band-gap. When $\Delta E \sim 1$ eV, i.e., the typical band-gap for both organic and inorganic materials, τ_{el} is on the order of 10^{-15} s. This implies that a polarisation cloud develops faster than does transit in the case of organic semiconductors, thus favouring the formation of polarons in them. Conventional wide band semiconductors like silicon do not normally succumb to the formation of polarons since the charge carrier residence time is much smaller than the polarisation time [20].

The simple calculation presented above is specific to so called electronic polarons as it concerns the polarisation of the electronic cloud surrounding a charge carrier. In addition to electronic polarons, molecular polarons are an additional feature of molecular semiconductors where the intramolecular vibrational modes of the individual molecule on which a charge carrier sits are modified in addition to the vibrational modes of neighbouring molecules. Molecular polarisation takes into account the effects of nuclear displacement of the atoms in the vicinity of the charge carrier. The molecular relaxation time is comparable to the residence time [20], making molecular polaron formation favourable in organic semiconductors. Lattice polarons are a third entity associated with the polarisation of the entire lattice. Electronic polarisation occurs the fastest, while lattice polarisation occurs the slowest.

Disorder within a system also tends to slow carriers down. This is why most disordered organic semiconductors have carrier mobilities that only approach 1 cm^2/Vs within a typical organic FET, even under the influence of a strong lateral electric field. An introduction of a little disorder to a system whose carriers would not normally form polarons would produce some localised states that sit within the band tail close to the mobility edge. The severity of the localisation grows with progression into the extremes of the band tails. When the localisation becomes quite strong, the band tails collapse into small-polaron states. This was an instability described by Anderson in 1972 and also by Emin and Holstein in 1976. Emin believes that under extreme localisation, non-polaronic localised states are only expected for a small fraction of charge carriers that lie close to the mobility edge, and the hypothesised exponential band tail of electronic states that disorder hopping models use is broken up by the instability of sufficiently localised states into small polaron states. Since the motion of polarons between localised sites requires the concomitant motion of the entire polarisation cloud, a polaron's transfer energy is very small. As a result of this, even in disordered materials, polaron bands are very narrow and are often comparable to $k_{\mathrm{B}}T$.

The mobility of a system of small polarons has an Arrhenius form [45],

$$\mu = \left(\frac{e\omega_0 R^2}{k_{\mathrm{B}}T}\right) \exp\left(-\frac{W_{\mathrm{H}}}{k_{\mathrm{B}}T}\right) \tag{1.5}$$

where e is the magnitude of electronic charge, ω_0 is the characteristic phonon frequency, R is the distance of the hop and W_{H} is the polaron activation energy. The existence of the parameter ω_0 in the expression for small polaron mobility quantifies the role of electron-phonon coupling in this model. The activation energy is the minimum energy needed to establish an energetic coincidence between electron energies at the initial and final sites. Hopping occurs when the atoms surrounding a jump's initial and final sites are displaced so as to bring the electronic energy at these two sites into transitory coincidence. Polaronic hopping is typically seen at high temperatures within disordered materials. As the temperature is lowered, the multiphonon processes that are prevalent at high temperatures ~ 300 K are frozen out and the mobility becomes non-Arrhenius tending to follow a trend described by variable range hopping [46, 47].

Polaron hopping is also discussed within the framework of Marcus' theory of electron transfer, where the transfer of charge from one site to another is considered to be equivalent to a simple bimodal reaction.

Marcus Model

An effective approach to describe charge transport in polarisable materials is to use Marcus' theory of electron transfer (ET). The theory was originally developed to describe the transfer of electrons from a donor to an acceptor in accordance with the following equation,

$$D^- + A \rightarrow D + A^-. \tag{1.6}$$

The approach represents the energy involved in such a reaction using a diagram where the energy of reactants (R) $D^- + A$ is V_{R} and that of the products (P) $D + A^-$ is V_{P}. Such a diagram is

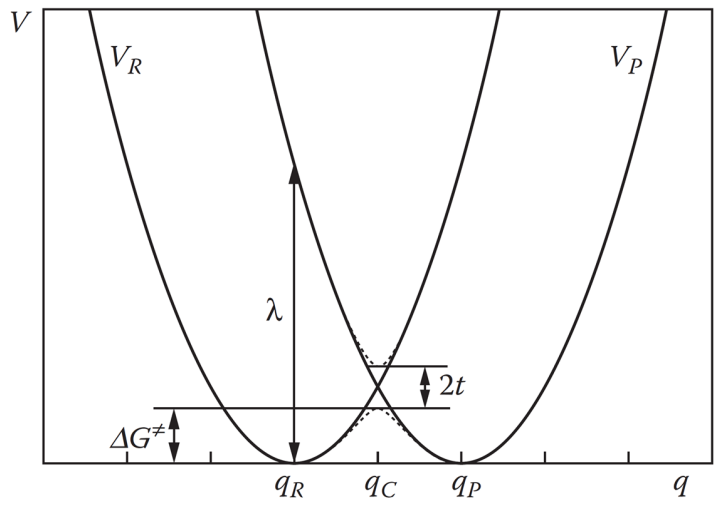

Figure 1.9: Potential energy parabolas in a charge transfer reaction. λ is the reorganisation energy, t the transfer integral, and $\Delta G^{\neq}$ is the energy barrier height. The solid lines are diabatic potential energy surfaces and the dotted lines are adiabatic potential energy surfaces. Image adapted from [20]

shown in Fig. 1.9. The reaction proceeds along a generalised configurational co-ordinate q.

If the electronic transfer between the two states is slower than molecular reorganisation, a case known as non-adiabatic transfer, the path taken by the electron can be decomposed into a vertical activation (λ) from the minimum of V_{R} to the V_{P} curve followed by a relaxation to the product's equilibrium configuration. The parameter λ in Marcus theory is called the reorganisation energy

$$\lambda = \frac{f}{2}(q_{\mathrm{R}} - q_{\mathrm{P}})^2, \tag{1.7}$$

where f is the oscillator strength. The parameter t shown in Fig. 1.9 is the transfer integral and is related to the energy barrier height $\Delta G^{\neq}$ shown in the Figure by

$$\Delta G^{\neq} = \frac{(\lambda - 2t)^2}{4\lambda} = \frac{\lambda}{4} - t \quad \text{for} \quad t < \lambda. \tag{1.8}$$

The transfer integral is dependent on the structural organisation of the organic solid. Using these definitions, Marcus theory arrives at an expression for the rate of electron transfer k_{ET} with a classical Arrhenius behaviour [48, 20],

$$k_{\mathrm{ET}} = \frac{2\pi}{\hbar}\frac{t^2}{\sqrt{4\pi\lambda k_{\mathrm{B}}T}}\exp\left[-\frac{\lambda/4 - t}{k_{\mathrm{B}}T}\right] \tag{1.9}$$

Marcus theory is connected to the polaron model through the carrier mobility which is dependent on the electron transfer rate by [49]

$$\mu = \frac{qR^2}{k_{\mathrm{B}}T}k_{\mathrm{ET}} \tag{1.10}$$

where R represents the lattice constant of the molecular crystal and the other parameters retain their usual meanings. In accordance with Marcus theory, activationless or band-like transport

takes place when $2t > \lambda$ and localised hopping transport takes place when $2t < \lambda$. A connection is made with molecular polarons when the reorganisation energy is linked with the molecular polarisation time and the transfer integral to the residence time. In this case, $\tau_{\text{res}} < \tau_{\text{el}}$ is the same as $2t > \lambda$ and $\tau_{\text{res}} > \tau_{\text{el}}$ is the same as $2t < \lambda$. As an example, delocalised transport is expected in pentacene since its reorganisation energy is 97 meV while its transfer integral is 98 meV thus satisfying the criterion $2t > \lambda$. Other molecular semiconductors like naphthalene have a reorganisation energy of 187 meV while the transfer integral is 37 meV thus satisfying the criteria for localised hopping conduction $2t < \lambda$.

Fundamentally, the rate of electronic transfer such as k_{ET} in the case of Marcus theory, governs the activation of carrier mobility. The polaron theory predicts a mobility activation that is Arrhenius at temperatures $\sim$ 300 K, and an Arrhenius behaviour is experimentally observed in many organic semiconductors [19, 44, 50]. Hence, in the absence of other sources of activation, such an observation is a strong indicator that charge transport in them rests on polaronic reorganisation. The polaron theory however neglects the contribution from disorder that may be either structural, positional or energetic.

1.4.2 Disorder hopping transport

Disorder hopping models normally used to explain charge carrier transport in organic semiconductors invoke the concept of thermally activated hopping between localised sites. In these models, site localisation is not a consequence of strong electron-phonon coupling as is the case for polaronic hopping. Nevertheless, inter-site hopping is assumed to take place due to an exchange of energy with phonons. One widely used disorder model, discussed below, assumes hopping via a variable range hopping mechanism using an expression for the electron transition rate originally developed by Allen Miller and Elihu Abrahams [51] to explain charge transport in lightly doped n-type silicon and germanium at low temperatures. In the Miller-Abrahams rate, the molecular details are usually neglected and instead of transfer integrals, only the "attempt-to-escape frequency" is approximated. In addition, only energetic site differences derived from a density of states distribution are taken into account instead of the reorganisation energy.

The use of such a disorder hopping model to explain charge transport in organic semiconductors at room temperature using an electron transition rate originally developed to explain transport in lightly doped inorganics at cryogenic temperatures has been a long lasting debate. Despite this, such disorder models have made some successful predictions. In this thesis, the Vissenberg-Matters disorder model is used to explain charge transport in PBTTT. The model, together with its successes and pitfalls, is described below. Its description will be followed by a model by Brondijk and co-workers that introduces a small modification to the Vissenberg-Matters model.

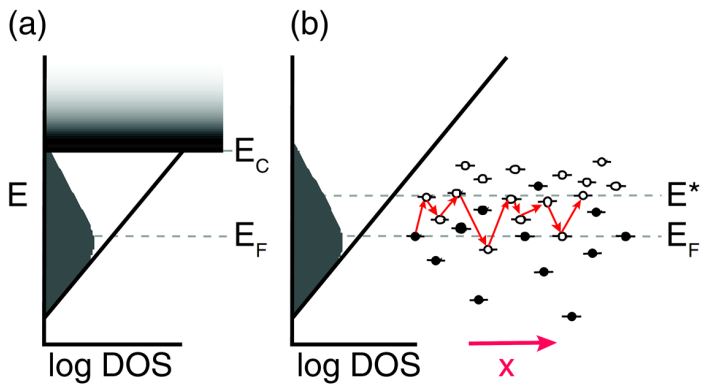

Figure 1.10: Schematic showing two accepted transport models within organic semiconductors. (a) A mobility edge model with an exponential density of tail states leading into a continuum of states and (b) A hopping model within an exponential density of states where transport is presumed to occur at the transport energy E^*. Image adapted from [52]

Vissenberg-Matters 3D transport model

The model of Vissenberg and Matters [30], henceforth refered to as the VM model, was developed in the late 1990s to explain charge transport in organic field effect transistors. This model was used within reasonable agreement to explain the measurements of the FET mobility in pentacene and polythienylene vinylene (PTV) as a function of carrier concentration and temperature. The VM model was very successful in describing two salient features of charge transport in organic FETs. (a) A super-linear increase in the device conductivity with an increasing density of charge carriers in the channel and (b) an Arrhenius behaviour of the conductivity with temperature. Its success on these two accounts unfortunately overshadowed the fact that the model totally neglected electron-phonon coupling, an effect known to be important in organic semiconductors at temperatures close to room temperature. In addition, it assumed that charges hop between localised energy states within an exponential distribution using a hopping mechanism, known as Variable Range Hopping (VRH), originally developed to explain transport in inorganic semiconductors at cryogenic temperatures. As a consequence of the above mentioned assumptions, the use of the VM Model has caused much debate and the need for a more complete model that takes into account inter-site hopping transport as well as electron-phonon coupling using a realistic hopping rate, unlike the one used in VRH, is looming.

The VM Model assumes an exponential density of energetic states (DOS) of the form

$$g(\epsilon) = \frac{N_{\mathrm{T}}}{k_{\mathrm{B}}T}\exp\left(\frac{\epsilon}{k_{\mathrm{B}}T_0}\right) \text{ for } -\infty < \epsilon \leq 0, \tag{1.11}$$

where N_{T} is the number of states per unit volume, k_{B} is Boltzmann's constant, and T_0 is a parameter that indicates the width of the exponential distribution. At any given temperature, a fraction of this exponential density of states, δN_{T} will be filled with charge carriers. The fraction

of occupied states is computed using the Fermi-Dirac distribution function as

$$\delta = \frac{1}{N_{\mathrm{T}}} \int g(\epsilon) f(\epsilon, \epsilon_{\mathrm{F}}) d\epsilon \cong \exp\left(\frac{\epsilon_{\mathrm{F}}}{k_{\mathrm{B}} T_0}\right) \Gamma(1 - T/T_0)\Gamma(1 + T/T_0) \tag{1.12}$$

with Γ being the gamma funtion $\Gamma(z) = \int_0^\infty \exp(-y) y^{z-1} dy$. In Eq. 1.12, the assumption has been made that carriers occupy sites with $\epsilon \ll 0$, i.e., $-\epsilon_{\mathrm{F}} \gg k_{\mathrm{B}} T_0$. This model breaks down for $T \geq T_0$ where the gamma functions in Eq. 1.12 diverge. At such temperatures, a majority of charge carriers are located close to $\epsilon = 0$.

According to Variable Range Hopping, a carrier may choose to either hop over a small distance with a high activation energy or over a long distance with a low activation energy. The VM Model invokes this idea by using a 'hopping rate' between two energetic states i and j of the form

$$\exp\left[-s_{ij}\right] = \exp\left[-\left(2aR_{ij} + \frac{|\epsilon_i - \epsilon_{\mathrm{F}}| + |\epsilon_j - \epsilon_{\mathrm{F}}| + |\epsilon_i - \epsilon_j|}{2k_{\mathrm{B}}T}\right)\right]. \tag{1.13}$$

The first term describes a tunneling process which depends on the overlap of the electronic wave functions of the sites i and j. Tunneling takes place across a distance R_{ij}. a is called the effective overlap parameter. The second term in Eq. 1.13 accounts for the activation for a hop from i to j upwards in energy. Conductivity within a system demonstrating percolative transport is described by

$$\sigma = \sigma_0 \exp(-s_{\mathrm{c}}), \tag{1.14}$$

σ_0 being an unknown prefactor. With the above definition for percolative transport using variable range hopping within an exponential density of states, the VM model derives an expression for the critical number of bonds $B_c(T_0, T, s_{\mathrm{c}}, a, \epsilon_{\mathrm{F}}, N_{\mathrm{T}})$ that are required for the onset of percolation. Using this, the conductivity turns out to be

$$\sigma(\delta, T) = \sigma_0 \left(\frac{\pi N_{\mathrm{T}} \delta (T_0/T)^3}{(2a)^3 B_{\mathrm{c}} \Gamma(1 - T/T_0)\Gamma(1 + T/T_0)}\right)^{T_0/T}. \tag{1.15}$$

The conductivity has an Arrhenius-like temperature dependence with $\sigma \propto \exp(-E_{\mathrm{A}}/k_{\mathrm{B}}T)$. The Arrhenius-like relation evolves when Eq. 1.12 for δ is substituted in Eq. 1.15 to cancel out the effect of the gamma functions and exponentiate T_0/T. The activation energy E_{A} is weakly temperature dependent. This behaviour of the conductivity within an exponential density of states contrasts the VRH conductivity within a constant density of states given by the Mott formula $\sigma \propto \exp(-T_1/T)^{1/4}$. Eq. 1.15 also shows that the conductivity increases superlinearly with carrier density, i.e., $\sigma \propto \delta^{(T_0/T)}$. This super-linearity is a consequence of filling up the exponential density of states. In the absence of such an exponential density of states, the conductivity is directly proportional to the carrier density.

In computing the carrier mobility μ within the channel of an organic transistor, the VM model assumes that the distribution of carriers at the interface between the organic semiconductor and the dielectric tapers away exponentially within the organic semiconductor (Fig. 1.11), i.e.,

$$\delta(x) = \delta_0 \exp\left(\frac{eV(x)}{k_{\mathrm{B}} T_0}\right), \tag{1.16}$$

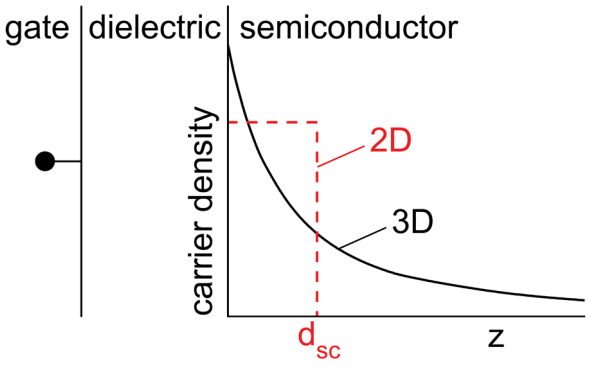

Figure 1.11: Schematic showing two possible approximations of the spatial distribution of charge carrier density at the interface between the organic semiconductor and the dielectric within an FET. Image adapted from [53]

with $V(x)$ being the gate induced potential at the interface. $V(x)$ and $\delta(x)$ can be deduced using the Poisson equation. Because the carrier distribution within the transistor channel in the VM model is assumed to decay exponentially from the interface, this VM model will be refered to as a 3D-disorder model.

Using the distance dependent occupation $\delta(x)$ from Eq. 1.16 in Eq. 1.15, the source-drain current in the FET's linear regime ($|V_{\mathrm{D}}| < |V_{\mathrm{G}}|$) is

$$I_{\mathrm{lin}} = \frac{WV_{\mathrm{D}}}{L} \int_0^t \sigma\left[\delta(x), T\right]. \tag{1.17}$$

W and L are the width and length of the channel of the FET. The field-effect mobility is computed from the expression for the current in the linear regime of the FET from Eq. 1.17 using the transconductance,

$$\mu_{\mathrm{FE}} = \frac{L}{CWV_{\mathrm{D}}} \frac{\partial I}{\partial V_{\mathrm{G}}}, \tag{1.18}$$

with C the dielectric capacitance and is stated in their work as being,

$$\mu_{\mathrm{FE}} = \frac{\sigma_0}{e} \left(\frac{\pi (T_0/T)^3}{(2a)^3 B_{\mathrm{c}} \Gamma(1 - T/T_0)\Gamma(1 + T/T_0)} \right)^{T_0/T} \times \left[\frac{(CV_{\mathrm{G}})^2}{2k_{\mathrm{B}} T_0 \epsilon_s} \right]^{T_0/T - 1}. \tag{1.19}$$

Eq. 1.19 was used in [30] to fit the measured linear field-effect mobility in pentacene and PTV. The results of the fit are shown in Fig. 1.12. The parameters used in the case of the pentacene fit were $\sigma_0 = 1.6 \times 10^{10}$ S/m, $a^{-1} = 2.2$ Å and $T_0 = 385$ K. In the case of PTV the fitting parameters were $\sigma_0 = 0.7 \times 10^{10}$ S/m, $a^{-1} = 0.8$ Å and $T_0 = 380$ K.

As a matter of fact, what is puzzling about these values is that even though the field-effect mobility of pentacene is two orders of magnitude higher than that of PTV, Fig. 1.12 (a), and the activation energy of pentacene differs from PTV by a factor of two, Fig. 1.12 (b), the metric of disorder T_0 is about the same for the two organic semiconductors.

In doing a fit to the temperature dependent field effect mobility got from a measurement, appropriate values for the parameters T_0, a and σ_0 have to be chosen in addition to the threshold

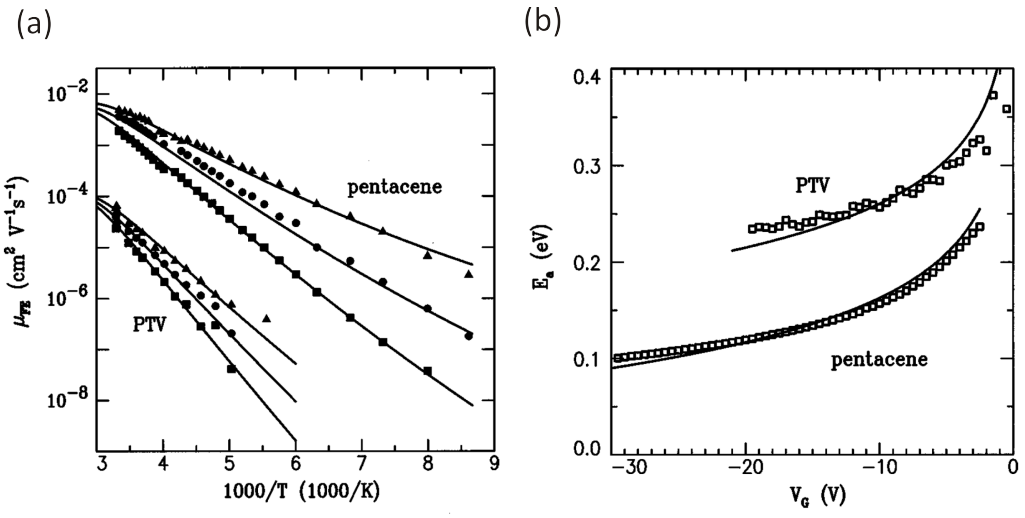

Figure 1.12: Fits of the VM model to pentacene and PTV. (a) Model predictions fit to the temperature dependent field-effect mobility in pentacene and PTV for three different gate voltages, $V_{\mathrm{G}} = -20$ V (triangles), -10 V (circles) and -5 V (squares) (b) Activation energy E_{A} for the field effect mobility in pentacene and PTV thin film transistors. Images adapted from [30]

voltage V_{th} of the transistor. It can be shown that a spectrum of T_0, a, and σ_0 values can be chosen to get a good fit and that the solution is unfortunately not unique. For this reason, although the model works reasonably in making its predictions of transport in organic semiconductors, the T_0 extracted from the fit to the transistor transfer curves must be treated only as a ballpark figure, and not as absolute.

Brondijk 2D transport model

J. J. Brondijk, in his 2012 paper to Physical Review Letters [53], modelled charge transport in Self-Assembled-Monolayer FETs (SAMFETs). The idea was that the active layer in a SAMFET can be treated as two dimensional (2D) owing to there being conduction only within a single monolayer. In this model, the density of charge carriers within the channel of the organic FET is assumed to be confined entirely to a thickness d_{sc} as shown in Fig. 1.11. The charge carrier concentration in the channel is proportional to the applied gate voltage and is given by

$$p = \frac{CV_{\mathrm{x}}}{ed_{\mathrm{sc}}}. \tag{1.20}$$

The thickness chosen in their work was $d_{\mathrm{sc}} = 2$ nm. The sheet conductance is calculated by integrating the conductance over the semiconductor thickness, d_{sc}. The source-drain current was obtained by integrating the sheet conductance over the potential V_{x} between the source and drain. The current in the linear regime was derived to be

$$I_{\mathrm{D}}{}^{\mathrm{2D}} = A\frac{W}{L}(d_{\mathrm{sc}})^{(1-T_0/T)}\left(\frac{C}{e}\right)^{T0/T}\frac{T}{T_0+T}\left[(V_{\mathrm{th}}-V_{\mathrm{G}})^{T_0/T+1} - (V_{\mathrm{th}}-V_{\mathrm{G}}+V_{\mathrm{D}})^{T_0/T+1}\right]. \tag{1.21}$$

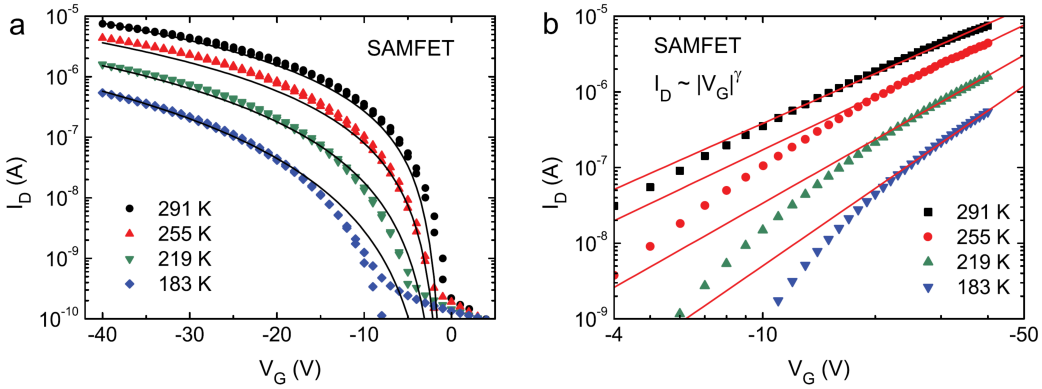

Figure 1.13: A fit of the temperature dependent transfer curves of a SAMFET using Brondijk's 2D model. Image adapted from [53].

Brondijk and co-workers also derive an expression for the current in an FET when the charge concentration in the channel is not strictly 2D, but falls off from the interface as a function of distance z from the interface as shown in Fig. 1.11,

$$p(z) = \frac{2k_{\mathrm{B}}T_0\epsilon_0\epsilon_{\mathrm{sc}}}{e^2(z+z_0)^2}. \tag{1.22}$$

In this 3D case, the linear source-drain current takes a slightly different form:

$$\begin{aligned} {I_{\mathrm{D}}}^{\mathrm{3D}} = \frac{A}{e}\frac{W}{L}\left(\frac{1}{2k_{\mathrm{B}}T_0\epsilon_0\epsilon_{\mathrm{sc}}}\right)^{T_0/T-1} C^{2T_0/T-1}\frac{T}{2T_0}\frac{T}{2T_0-T} \\ \times\left[(V_{\mathrm{th}}-V_{\mathrm{G}})^{2T_0/T}-(V_{\mathrm{th}}-V_{\mathrm{G}}+V_{\mathrm{D}})^{2T_0/T}\right]. \end{aligned} \tag{1.23}$$

In the above equations, A is a constant that includes the percolation parameter B_c, the inverse localisation length a^{-1}, the width of the exponential density of states T_0, and the conductivity prefactor σ_0. Once again, when these equations for the source-drain current are used to fit the measured currents in the device, there are many parameters that can be tweaked to get a good fit. In the 2D model explained very briefly here, an additional fitting paramter is the thickness of confined carriers in the channel, d_{sc}. Brondijk's work in Fig. 1.13 shows the use of the 2D model in interpreting charge transport within a SAMFET.

The parameters used in getting a good fit to the data were $\sigma_0 = 4 \times 10^6$ S/m, $a^{-1} = 4.3$ Å, $T_0 = 627$ K, $d_{\mathrm{sc}} = 2$ nm and a threshold voltage $V_{\mathrm{th}} = -1$ V. The index of disorder, T_0, is typically larger when transistor transfer curves are fit to a 2D model than when they are fit to a 3D model.

In the same paper, Brondijk used Eq. 1.23 to fit transistor linear transfer curves of a few semiconducting polymers, P3HT and PTV. Once again, the fits look reasonable at high gate fields. Despite this, it is interesting to note that the T_0 value of PTV was stated here to be 441 K, a value different from $T_0 = 380$ K reported for the same material by Vissenberg and Matters in 1998. It is also striking to note that the T_0 value for pentacene was reported to be 385 K in [30], but 1000 K in [52]. These inconsistencies prove that the disorder as quantified by T_0

within the exponential DOS description of the same material can disparately differ depending on the other fitting parameters chosen.

A. J. Kronemeijer, in this recent paper [54], took a step further and adapted Brondijk's 2D model for charge transport to fit FET transfer curves in the saturation regime of a spectrum of semiconducting polymers such as PBTTT, P3HT, PTAA and N2200. The expression derived by him for the source-drain current in the saturation regime was achieved by substituting V_{D} with $V_{\mathrm{G}} - V_{\mathrm{th}}$ in Brondijk's Eq. 1.21 above to get,

$$I_{\mathrm{D}}{}^{\mathrm{2D}} = A\frac{W}{L}(d_{\mathrm{sc}})^{1-(T_0/T)}\left(\frac{C}{e}\right)^{T0/T}\frac{T}{T_0+T}(V_{\mathrm{G}}-V_{\mathrm{th}})^{T_0/T+1} \tag{1.24}$$

with the parameter A defined as

$$A = \sigma_0\left(\frac{\left(\frac{T_0}{T}\right)^4 \sin\left(\pi\frac{T}{T_0}\right)}{(2a)^3 B_c}\right)^{T0/T} \tag{1.25}$$

The T_0 values extracted from these polymers ranged between 366 K and 670 K. In fact, for PBTTT T_0 was shown to be 670 K while for P3HT, T_0 equaled 585 K. This is despite the fact that PBTTT is known to have greater order within its films than does P3HT [55].

For the various reasons highlighted at different stages above and the experience gained by playing with both the 2D and 3D disorder models to fit transistor transfer curves measured for this thesis, it is hard not to be convinced that these disorder models are only approximate. The values of the fitting parameters used to simulate the experimental data are never necessarily unique and the T_0 values can vary over several 100 K. There is hence an immediate need to either improve these models to make predictions of the T_0 values of different organic semiconductors more robust, perhaps by including the effects of electron-phonon coupling, or by using more realistic hopping rates that hold true for soft semiconductors at temperatures close to 300 K.

The ad-hoc scheme known as disorder hopping is based on the Miller-Abrahams jump rate developed to explain cryogenic hopping conduction in lightly doped conventional semiconductors. The disorder model assumes that hopping is non-adiabatic. However, the Landau-Zener analysis of charge transfer shows that only exceptionally long hops in extremely sparse hopping systems are candidates for non-adiabatic hopping. Thus, having to invoke Mott's variable range hopping among inter-impurity sites at low temperatures to hopping among intrinsic sites at high temperatures is not considered logical by many outside the organic electronics community.

1.4.3 Disorder + Polaronic hopping transport

Chang and co-workers proposed a framework in 2007 that combines a mobility edge model with a model for polaron transport [34]. This model was used to describe transport in FETs based on P3HT of different molecular weight, thus tuning the device mobility. At the heart of this model is the following expression for the FET mobility;

$$\mu\left(V_{\mathrm{G}}, T\right) = \mu_0 \exp\left(-\frac{E_A}{k_{\mathrm{B}}T}\right)\frac{N_{\mathrm{mob}}(V_{\mathrm{G}}, T)}{N_{\mathrm{tot}}}. \tag{1.26}$$

This model ensures that the temperature and gate-voltage dependence of the FET mobility is captured by the ratio of the density of mobile charge carriers N_{mob} to the total density of states N_{tot}, while the total activation energy is bolstered by a polaronic contribution. Polaronic effects do not influence either the temperature or the gate voltage dependence of mobility. In Chang's work, an exponential density of states was chosen to model localised states while a parabolic DOS was chosen to model mobile states.

A more recent form of such concocted disorder-polaron hopping models is outlined in the 2013 paper "Unified description for hopping transport in organic semiconductors including both energetic disorder and polaronic contributions" by Fishchuk and co-workers [56]. This model avoids the phenomenological shortcomings of using the concept of transport energy, percolation and a Millier-Abrahams hopping rate to explain the observed trends in carrier mobility within organic semiconductors. Instead, it uses a Marcus-type jump rate to account for polaron formation in consonance with a Gaussian disorder model that accounts for energetic disorder. The Marcus-type rate used in this model is given by

$$k_{ij} = \frac{J_{ij}^2}{\hbar}\sqrt{\frac{\pi}{4E_{\mathrm{A}}k_{\mathrm{B}}T}}\exp\left[-\frac{E_{\mathrm{A}}}{k_{\mathrm{B}}T} - \frac{\epsilon_i - \epsilon_j}{2k_{\mathrm{B}}T} - \frac{(\epsilon_i - \epsilon_j)^2}{16E_{\mathrm{A}}k_{\mathrm{B}}T}\right]. \tag{1.27}$$

E_{A} is related to the reorganisation energy λ by $E_{\mathrm{A}} = \lambda/4$, $J_{ij} = J_0\exp(-2\gamma R_{ij})$ where γ is the inverse localisation radius between the adjacent sites i and j while R_{ij} is the distance between the two sites. J_0 is the prefactor of the transfer integral.

The nature of the hopping rate chosen when modeling charge transport ultimately influences the variation of conductivity as a function of gate-voltage and temperature in the organic semiconductor. It is hence of utmost importance to use a hopping rate having a form that properly describes all facets of the observed nature of charge carriers in organic semiconductors, and at the same time remains physically plausible. Hence, such a concocted disorder-polaron model based on a Marcus-type hopping rate represents a significant step forward in the description of charge transport within these material systems.

1.5 The Seebeck coefficient

Charge transport in organic field-effect transistors (FETs) is usually addressed by measuring the field-effect mobility of their charge carriers and its dependence on temperature and gate voltage [19, 57]. In addition to the field effect mobility, another potent but underutilised complementary transport coefficient is the Seebeck coefficient. Measurements of charge carriers' Seebeck coefficients as functions of temperature and gate voltage provide a distinct probe of electronic transport mechanisms in organic FETs. If a temperature differential ΔT is applied across a conducting solid, charges within the solid diffuse from the hot to the cold end of the sample and an electric field builds up within the system to oppose any further diffusion of charges. The built-in electric field reveals itself as a measurable thermal voltage, $\Delta V_{\mathrm{thermal}}$. Fig. 1.14 illustrates this build up of a thermal voltage in three stages. The Seebeck coefficient α, also referred to as thermopower, is given by the relation $\alpha = \lim_{\Delta T\to 0}\Delta V_{\mathrm{thermal}}/\Delta T$. It

represents the entropy transported by a carrier divided by its charge q [58]. This transported entropy is the sum of (1) the alteration of a solid's entropy produced by the addition of a charge carrier (refered to as the entropy-of-mixing) plus (2) the heat carried in moving the charge carrier divided by the temperature T [59]. Adding a charge carrier alters (1) the entropy associated with distributing carriers among accessible states, (2) the solids magnetic moments and their alignments, and (3) the atoms' vibrations. The heat transported with a charge carrier is governed by its exchange of energy with atomic vibrations. Of all the contributions to the Seebeck coefficient, only the entropy-of-mixing contribution depends explicitly on the carrier density. In particular, $\alpha_{\mathrm{mix}} = (k/e)\ln\left([N(E) - n(E)]/n(E)\right) = (k/e)[(E-\mu)/kT]$ for $n(E)$ independent Fermion carriers moving among $N(E)$ states of energy E, where k_{B} denotes the Boltzmann constant and μ represents the chemical potential. A semiconductor's Seebeck coefficient is generally large, $> k_{\mathrm{B}}/e$ (86 μV/K), since its carrier density is generally much less than the density of states among which carriers move. By contrast, the Seebeck coefficients of conventional metals are small, $\ll k_{\mathrm{B}}/e$, since the carrier density is comparable to the density of states among which carriers can move. Other contributions to the Seebeck coefficient do not explicitly depend on the carrier density. For example, carriers whose mutual Coulomb repulsion precludes their double occupation of a state possess a two-fold orientation degeneracy of their spins: $\alpha_{\mathrm{spin}} = (k_{\mathrm{B}}/e)\ln(2)$ in non-magnetic solids. A carrier's alteration of surrounding inter-atomic stiffness constants also affects its Seebeck coefficient [59]. Conventional Seebeck coefficient measurements have been used to determine the carrier density [60], its temperature dependence [61] and the carrier-induced softening of atomic vibrations [62]. Modulation of the Seebeck coefficient's spin contribution with an applied magnetic field enables determination of the carrier's magnetic moment [63]. Typically the Seebeck coefficient is only measured as a function of temperature. The carrier density is then just one of the physical parameters that change as the temperature is altered. A different situation exists for Seebeck measurements of an FET, where the carrier density is governed by the gate voltage as it controls the charge that enters the device's accumulation region.

The central theme of this PhD thesis is to measure the Seebeck coefficient within the channel of several organic FETs both as a function of a gate voltage as well as temperature. The ultimate intention of these measurements is to understand charge transport in these materials from the observations.

1.5.1 Generalised description of the Seebeck coefficient

In his classic paper [64], Fritzsche derives a general expression for the Seebeck coefficient without references to a specific conduction process by expressing it as an integral over one electron energy states. He neglects correlation effects and models the conductivity as

$$\sigma = \int \sigma(E) dE. \tag{1.28}$$

Here, $\sigma(E)$ is called the differential conductivity, the fractional contribution of electrons with an energy E to the total conductivity. Π being the Peltier coefficient whose physical meaning is

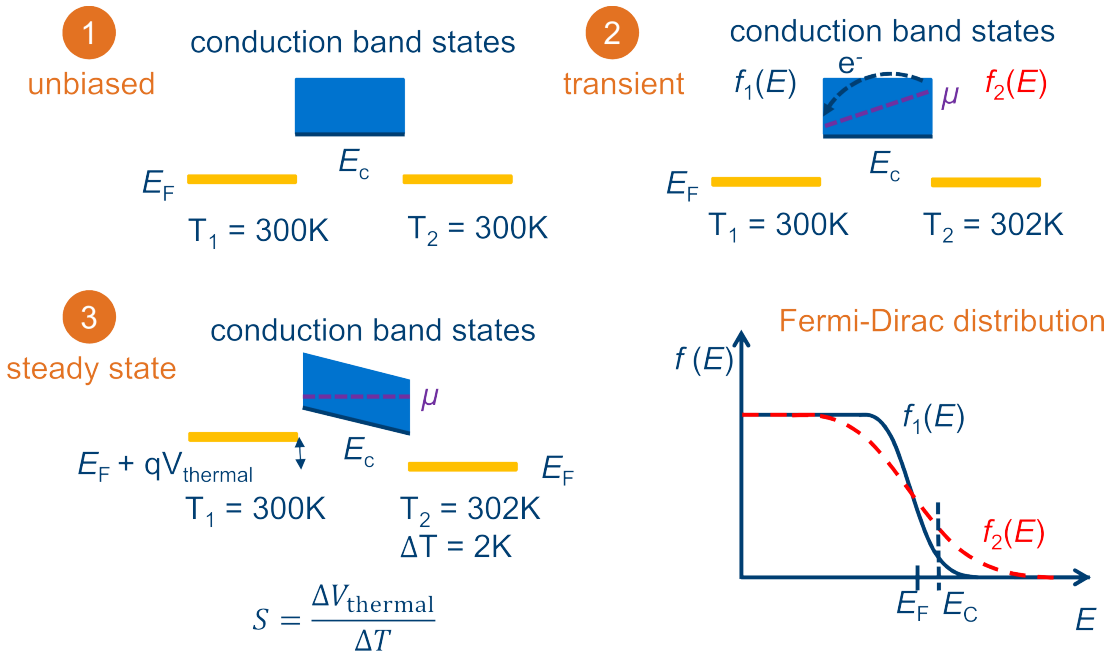

Figure 1.14: The three consecutive stages in the build up of a thermal voltage across a conducting solid. (1) An unbiased situation where the two electrodes on either side of the conducting solid are maintained at the same temperature 300 K. (2) A transient situation where a temperature differential of 2 K is imposed across the conductor which creates an imbalance in the chemical potential μ within the conductor, spurring carrier diffusion from the hot end to the cold end. (3) A steady state situation where a thermal voltage is built-in within the conductor to counter balance the diffusive flow of charge carriers and equalise the chemical potential throughout.

the energy transported per unit charge, the Seebeck coefficient S can be defined by $S = \Pi/T$. Assuming that every electron above the Fermi level contributes to Π in proportion to its contribution to the conductivity, i.e., $\sigma(E)/\sigma$, Fritzsche writes down an expression for the Peltier coefficient as

$$\Pi = -\frac{1}{e}\int (E - E_{\mathrm{F}})\,\frac{\sigma(E)}{\sigma}dE \tag{1.29}$$

The Seebeck coefficient can then be written as

$$S = -\frac{k_{\mathrm{B}}}{e}\int \left(\frac{E - E_{\mathrm{F}}}{k_{\mathrm{B}}T}\right)\frac{\sigma(E)}{\sigma}dE \tag{1.30}$$

It is from here that one can derive the familiar expressions for the Seebeck coefficient in semiconductors. For example, should conduction take place only in a single band of a semiconductor (either conduction E_{C} or valence E_{V}), from Eq. 1.30 one arrives at simplified expressions for the Seebeck as

$$S = -\frac{k_{\mathrm{B}}}{e}\left[\frac{E_{\mathrm{C}} - E_{\mathrm{F}}}{k_{\mathrm{B}}T} + A_{\mathrm{C}}\right] \tag{1.31}$$

$$S = \frac{k_{\mathrm{B}}}{e}\left[\frac{E_{\mathrm{F}} - E_{\mathrm{V}}}{k_{\mathrm{B}}T} + A_{\mathrm{V}}\right] \tag{1.32}$$

with the heat of transport constants A_{C} and A_{V} defined as

$$A_{\mathrm{C}} = \int_0^\infty \frac{\epsilon}{k_{\mathrm{B}}T}\sigma(\epsilon)d\epsilon \Big/ \int_0^\infty \sigma(\epsilon)d\epsilon \text{ with } \epsilon = E - E_{\mathrm{C}} \tag{1.33}$$

$$A_{\mathrm{V}} = \int_{-\infty}^0 \frac{\epsilon}{k_{\mathrm{B}}T}\sigma(\epsilon)d\epsilon \Big/ \int_\infty^0 \sigma(\epsilon)d\epsilon \text{ with } \epsilon = E_{\mathrm{V}} - E \tag{1.34}$$

The above equations can also be derived using the Boltzmann transport equation as will be shown in the next section. The Seebeck coefficient for multiband electron conduction as well as metallic conduction,

$$S = -\frac{\pi^2 k_B^2 T}{3e}\left[\frac{d\ln\sigma(E)}{dE}\right]_{E_F}, \tag{1.35}$$

can also be derived from Eq. 1.30 as done in [64].

1.5.2 Seebeck coefficient from the Boltzmann transport equation

The two fundamental transport coefficients, conductivity and Seebeck coefficient, studied in this work can be derived for crystalline solids with unambiguous band transport by solving the Boltzmann transport equation as done in [65] under particular conditions enumerated in this section. The Boltzmann transport equation is a fundamental law in non-equilibrium statistical mechanics that describes the properties of a statistical system that is driven out of thermodynamic equilibrium. A good example of such a system is a solid, fluid or gas under an

applied electric field or a thermal gradient. The equation represents a balance between driving fields and scattering processes and in the presence of an applied electric field **E** is given by:

$$\frac{\partial f}{\partial t} + \mathbf{v} \cdot \nabla_{\mathbf{r}} f + \frac{q}{\hbar} \mathbf{E} \cdot \nabla_{\mathbf{k}} f = \left(\frac{\partial f}{\partial t} \right)_{collision} \tag{1.36}$$

where f, the distribution function, represents the statistical distribution of particles in the system. Bold face alphabets represent vectors. **v** is the particle velocity, **k** the wave vector, q the charge and $\hbar$ the reduced Plank's constant. The terms on the left hand side of the equation characterize driving forces and the one on the right is the collision term. In the absence of a driving force in the solid, the distribution function f_0 is the Fermi-Dirac distribution given by

$$f_0(\mathbf{k}) = \frac{1}{\exp\left(\frac{E(\mathbf{k}) - E_{\mathrm{F}}}{k_{\mathrm{B}} T} \right) + 1} \tag{1.37}$$

E(**k**) being the energy of particles with wave vector **k** and E_{F} being the chemical potential. k_{B} is the Boltzmann constant. Under the relaxation time approximation, i.e, an assumption that the system is driven towards equilibrium within a relaxation time τ, the collision term becomes

$$\left(\frac{\partial f}{\partial t} \right)_{collision} = -\frac{f(E) - f_0(E)}{\tau} \tag{1.38}$$

One can recast the derivatives in Eq. 1.36 into:

$$\nabla_{\mathbf{k}} f = \frac{\partial f}{\partial E} \hbar \mathbf{v} \quad \text{and} \quad \nabla_{\mathbf{r}} f = \frac{\partial f}{\partial T} \nabla_{\mathbf{r}} T. \tag{1.39}$$

Under an additional assumption that the perturbation in the system due to the external driving force is small,

$$\frac{\partial f}{\partial E} \approx \frac{\partial f_0}{\partial E} \quad \text{and} \quad \frac{\partial f}{\partial T} \approx \frac{\partial f_0}{\partial T}. \tag{1.40}$$

Using the expression for the Fermi-Dirac distribution function Eq. 1.37,

$$\frac{\partial f_0}{\partial T} = -\frac{\partial f_0}{\partial E} \frac{E - E_{\mathrm{F}}}{T}. \tag{1.41}$$

Clubbing Eqs. 1.38, 1.39, 1.40 and 1.41 together with the Boltzmann transport Eq. 1.36 in the steady state ($\frac{\partial f}{\partial t} = 0$), one arrives at the following equation:

$$f \approx f_0 + \tau \frac{\partial f_0}{\partial E} \left[(\mathbf{v} \cdot \nabla_{\mathbf{r}} T) \frac{E - E_F}{T} - q(\mathbf{v} \cdot \mathbf{E}) \right]. \tag{1.42}$$

One can then proceed from here to derive expressions for the conductivity and the Seebeck coefficient. $g(E)$ being the density of states, the charge carrier density n, the charge current density **j** and the heat current density $\mathbf{j}_Q$ are defined by

$$n = \int_0^\infty g(E) f(E, E_{\mathrm{F}}) dE \tag{1.43}$$

$$\mathbf{j} = q \int_0^\infty \mathbf{v} g(E) f(E, E_{\mathrm{F}}) dE \tag{1.44}$$

$$\mathbf{j}_Q = \int_0^\infty (E - E_F)\mathbf{v}g(E)f(E, E_\mathrm{F})dE \tag{1.45}$$

Using Ohm's law $\mathbf{j} = \sigma\mathbf{E}$, and substituting Eq. 1.42 with $\nabla_\mathbf{r}T = 0$ into Eq. 1.44, the following equation is arrived at,

$$\mathbf{j} = -q^2 \int_0^\infty \tau\mathbf{v}(\mathbf{v}\cdot\mathbf{E})g(E)\frac{\partial f_0}{\partial E}dE \tag{1.46}$$

assuming that the energy of charge carriers $E = \frac{d}{2}m_e v^2$, m_e being the effective mass. v the velocity and d the dimensionality of the system, we arrive at an expression for the conductivity

$$\mathbf{j} = \left(-\frac{2q^2}{dm_e}\int_0^\infty \tau E g(E)\frac{\partial f_0}{\partial E}dE\right)\mathbf{E} = \sigma\mathbf{E} \tag{1.47}$$

To get the Seebeck coefficient, one needs to set the charge current $\mathbf{j} = 0$ in Eq. 1.44 after having substituted for f from Eq. 1.42. In essence,

$$\mathbf{j} = q\int_0^\infty \mathbf{v}g(E)\left(f_0 + \tau\frac{\partial f_0}{\partial E}\left[(\mathbf{v}\cdot\nabla_\mathbf{r}T)\frac{E - E_\mathrm{F}}{T} - q(\mathbf{v}\cdot\mathbf{E})\right]\right)dE = 0 \tag{1.48}$$

Solving for the electric field $\mathbf{E}$, in the above equation one meets with the following result:

$$\begin{aligned}\mathbf{E} = \nabla_\mathbf{r}T\frac{1}{qT}\left(\int_0^\infty E^2 g(E)\tau\frac{\partial f_0}{\partial E}dE - E_\mathrm{F}\int_0^\infty Eg(E)\tau\frac{\partial f_0}{\partial E}dE\right)\\ \times\left(\int_0^\infty Eg(E)\tau\frac{\partial f_0}{\partial E}dE\right)^{-1}\end{aligned} \tag{1.49}$$

r being an integer, the integrals in the above equation are of the form

$$\int_0^\infty E^r g(E)\tau\frac{\partial f_0}{\partial E}dE \tag{1.50}$$

One then defines integrals K_i of the form

$$K_i = -\frac{2T}{dm_e}\int_0^\infty E^{i+1}g(E)\tau(E)\frac{\partial f_0(E)}{\partial E}dE \tag{1.51}$$

where d is the dimensionality of the system defined earlier. The expressions for σ and S can be expressed in terms of these integrals K_i as

$$\sigma = \frac{q^2}{T}K_0 \text{ and } S = -\frac{1}{qT}\left(E_\mathrm{F} - \frac{K_1}{K_0}\right) \tag{1.52}$$

One can take a further step and recast S in Eq. 1.52 for electronic conduction in the conduction band (E_C) as:

$$S = \frac{1}{qT}\left(E_\mathrm{C} - E_\mathrm{F} - E_\mathrm{C} + \frac{K_1}{K_0}\right) = -\frac{k_\mathrm{B}}{e}\left(\frac{E_\mathrm{C} - E_\mathrm{F}}{k_\mathrm{B}T} + A_\mathrm{C}\right) \tag{1.53}$$

with

$$A_\mathrm{C} = \frac{1}{k_\mathrm{B}T}\left(\frac{K_1}{K_0} - E_\mathrm{C}\right) \tag{1.54}$$

In a similar way, one can write down S for hole conduction in the valence band as:

$$S = \frac{k_B}{e}\left(\frac{E_F - E_V}{k_B T} + A_V\right) \tag{1.55}$$

with

$$A_V = \frac{1}{k_B T}\left(E_V - \frac{K_1}{K_0}\right) \tag{1.56}$$

The Seebeck coefficient is negative (positive) for materials where electrons (holes) are the dominant charge carriers. The constants A_C and A_V are dimensionless parameters that account for the asymmetric distribution in energies of charge carriers around the conduction band or valence band. There is a claim that the magnitude of A, gives an independent insight into the nature of conduction, being either band-like as in Si and Ge, or hopping-like as in many amorphous semiconductors. As documented by Pernstich and co-workers [66], a value of A that is small and positive, typically between 2 and 4, is normally observed in conventional band semiconductors. When A is much larger, the role of a different transport mechanism is expected. An example of this is the amorphous semiconductor As_2Se_3 with A between -7 and -11. This said, within an alternative hopping framework that will be described in the next section, the constant A is often neglected in the case of disordered semiconductors and insulators [67].

The take home message from this quasi-rigorous derivation is as follows. The transport coefficients are derivable from the Boltzmann transport equation and are chained to each other through the integral K_0 in such a way that an increase in the conductivity manifests itself as a decrease in the Seebeck coefficient. This is however true only for semiconductors where conduction occurs in well defined bands. For conductors where conduction takes place through mechanisms such as thermally activated hopping or variable range hopping (VRH), the same need not hold true.

1.5.3 Seebeck coefficient within the disorder model

Charge transport in organic polymers is typically described using various hopping theories and the concept of transport energy E^*. E^* represents the energy level within the disordered density of states that contributes most to conduction within the material. Within a multiple trap and release model, it plays the same role as the mobility edge does in amorphous inorganic semiconductors. Within the theoretical framework for charge transport in disordered materials developed by Roland Schmechel [68], the Seebeck coefficient within a hopping system is defined in terms of E^* as

$$\alpha = \frac{k_B}{e}\left(\frac{E_F - E^*}{k_B T}\right). \tag{1.57}$$

In a nutshell, Schmechel arrives at this equation as follows. First, the differential conductivity $\sigma'(E)$ within the transport band is defined as

$$\sigma'(E)dE = en'(E)\mu(E)dE \tag{1.58}$$

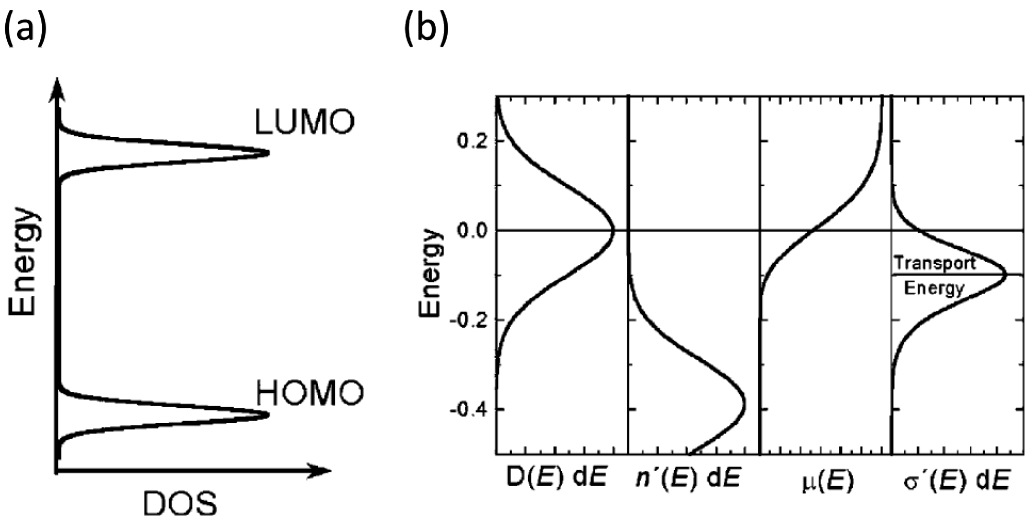

Figure 1.15: (a) HOMO and LUMO levels within an organic semiconductor described using a Gaussian. (b) The differential transport parameters that aid in the description of the transport energy level E^*. Image adapted from [68]

which is a prerequisite for defining the differential current density distribution by Ohms law,

$$j'(E)dE = \sigma'(E)FdE \tag{1.59}$$

where $n'(E)$ is the differential carrier density, $\mu(E)$ is the mean mobility of charge carriers at energy E, e is the elementary charge and F is the applied field strength. The differential carrier distribution $n'(E)dE$ is in turn expressed through a chosen density of states distribution $D(E)$ and the Fermi-Dirac distribution in thermal equilibrium $f(E) = 1/[\exp(E - E_\mathrm{F})/k_\mathrm{B}T + 1]$,

$$n'(E)dE = D(E)f(E)dE. \tag{1.60}$$

Although Schmechel chose the density of states distribution to have a Gaussian form (Fig. 1.15 (a)), the same description can be applied to an exponential density of states. The interplay between the different differential transport quantities $D(E)dE$, $n'(E)dE$, $\mu(E)$ and $\sigma'(E)dE$ is shown in Fig. 1.15 (b). The transport energy shown in Fig. 1.15 (b) is E^* and need not coincide with the maximum of the differential density of states $D(E)dE$. Technically, the definition of E^* is "the averaged energy weighted by the current density $j'(E)$ or the conductivity $\sigma'(E)$ within the disordered density of states", i.e.,

$$E^* = \frac{\int_{-\infty}^{+\infty} E' j(E')dE'}{\int_{-\infty}^{+\infty} j(E')dE'} = \frac{1}{\sigma}\int_{-\infty}^{+\infty} E'\sigma'(E')dE'. \tag{1.61}$$

It hence reflects the energy level where transport is most likely to occur within the disordered DOS of an organic semiconductor and can vary with temperature and gate voltage as will be demonstrated later. As long as the conductivity distribution is symmetric, E^* will lie at the maximum of the conductivity distribution, Fig. 1.15 (b). It is of importance to note that the

Seebeck coefficient in the hopping regime also evolves from the generalised form of the Seebeck coefficient quoted before,

$$S = -\frac{k_B}{e}\int\left(\frac{E-E_F}{k_\mathrm{B}T}\right)\frac{\sigma(E)}{\sigma}dE = \frac{k_\mathrm{B}}{e}\left(\frac{E_\mathrm{F}-E^*}{k_\mathrm{B}T}\right). \tag{1.62}$$

with E^* defined in Eq. 1.61.

The difference between the Seebeck coefficient in a system with hopping conduction, Eq. 1.57, and the Seebeck coefficient in a system with band transport, Eq. 1.55 is most noticeably the absence of the heat of transport constant A for the hopping Seebeck. This is because A in the Seebeck for band transport accounts for the contribution to transport from energy levels beyond the band edge. The model for the hopping Seebeck takes into account transport at only one energy level E^*, neglecting the contribution to transport from energy levels above and below E^* that may also realistically contribute to charge transport.

When modelling the Seebeck coefficient in organic FETs, the only parameters needed are the Fermi level E_F, and the transport level E^*. A demonstration of how these two energy levels are extracted to estimate the hopping Seebeck is done in Chap. 3 on the Seebeck coefficient in PBTTT.

As a final note, it is of paramount importance to understand that although the description of the Seebeck coefficient in the hopping regime discussed above, Eq. 1.57, is defined within a framework of a definite disordered density of states, the form is generic and remains the same even if the imposition of a Gaussian or exponential DOS is removed. David Emin, in his 1975 communication to Physical Review Letters, evolves a similar formula for the Seebeck from first principles where phonon assisted hopping between two sites of unequal energies ϵ_i and ϵ_j is considered [69]. It was shown that the Seebeck coefficient in his description is

$$\alpha_{ij} = \frac{k_\mathrm{B}}{q}\left(\frac{\frac{1}{2}(\epsilon_i+\epsilon_j)+E_T^{ij}-\zeta}{k_\mathrm{B}T}\right). \tag{1.63}$$

where α_{ij} is the thermoelectric power associated with a hop from site i to site j, ϵ_i and ϵ_j are the equilibrium energies of the system when the electron occupies site i or j, E_T^{ij} is a term defined using the relative temperature difference between the two site energies at i and j as well as the rates characterising phonon assisted hops between them. q is the charge of the carrier, which for electrons is $-|e|$ and ζ represents the true equilibrium chemical potential of the system.

1.5.4 Seebeck coefficient in a narrow band (polaron) model

Polaronic bands are known to be very narrow in comparison to the energy bands of crystalline solids, with the width of a polaron band being typically on the order of $k_\mathrm{B}T$. This comes about because the transport of polarons requires both the transport of the charge carrier and its associated polarisation cloud, thus significantly limiting the energy range within which this can occur. The Seebeck coefficient for a system of polarons hence conforms to the description of the Seebeck coefficient in a narrow band system. Starting with the expression for the Seebeck in a wide band hole system, and working with the assumption that the wide band collapses into a

narrow band such that charge transport occurs only within a small distribution of energies, A_V tends to zero and the Seebeck coefficient is given by,

$$S = \frac{k_B}{e}\left[\frac{E_F - E_V}{k_B T}\right]. \tag{1.64}$$

The distribution of n holes over N available states is governed by the Fermi-Dirac distribution

$$n = \frac{N}{\exp\left(\frac{E_F - E_V}{k_B T}\right) + 1}. \tag{1.65}$$

Within a narrow band W such that $W \ll k_B T$, all the sites within the band are thermally accessible at all temperatures. The fraction of the total number of available states N filled by n carriers is hence temperature independent. Under these circumstances, the Seebeck coefficient is not written either as a function of $E_F - E_V$ as is done for band systems or as a function of $E_F - E^*$ for hopping systems with a large energetic disorder. Instead, the Seebeck is written in terms of the fractional occupancy $c = n/N$ using the Fermi-Dirac distribution. In other words,

$$\alpha = \frac{k_B}{e}\left(\frac{E_F - E_V}{k_B T}\right) = \frac{k_B}{e}\ln\left(\frac{1-c}{c}\right). \tag{1.66}$$

Within an organic FET, where the total carrier density introduced in the channel of the device is smaller than the total number of avaliable states, i.e., $n \ll N$. The Seebeck coefficient is recast as

$$\alpha = \frac{k_B}{e}\left(\frac{1-c}{c}\right) = \frac{k_B}{e}\ln\left(\frac{N-n}{n}\right) \approx \frac{k_B}{e}\ln\left(\frac{N}{n}\right) \tag{1.67}$$

The Seebeck coefficient in this form takes into account only the entropy-of-mixing contribution (sometimes also called the configurational entropy). It represents the total number of ways by which n indistinguishable carriers are distributed among a total of N available states. Although in most semiconductors, the entropy of mixing contribution to the Seebeck is the most dominant, the picture is complete only when the additional contributions to the Seebeck coefficient are taken into account. The entropy by virtue of Fermionic spin degeneracy is $(k/e)\ln(2)$. It comes about when spin 1/2 degeneracy is taken into account into the Fermi-Dirac distribution above. The other contribution to the Seebeck stems from an alteration of vibrational modes within a system as a direct consequence of the presence of a charge carrier. This vibronic contribution to the Seebeck is given the notation α_{vib}. α_{vib} is temperature independent and takes the generic form [70, 71]

$$\alpha_{vib} = k_B\left[\sum_j N_j \left|\frac{\Delta\nu}{\nu}\right|_j\right] \tag{1.68}$$

where N_j is the number of softened or hardened vibrational modes and ν_j their frequencies. α_{vib} was shown to be substantial for polarisable organic molecular semiconductors such as pentacene [70] and is on the order of 250 μV/K. There are no documented accounts of α_{vib} for organic polymers to date.

The total Seebeck coefficient for a narrow band system that includes the contributions from configurational entropy, spin and a change in vibronic modes is then;

$$\alpha = \frac{k_B}{e}\ln\left(\frac{N}{n}\right) + \frac{k_B}{e}\ln(2) + \alpha_{vib}. \tag{1.69}$$

If there exists a trap density of states n_{trap} within the system that captures a fraction of the total number of carriers n, the configurational entropy is modified to account for these trap states and the fact that they do not contribute to any transported entropy. Thus, the total Seebeck coefficient in the presence of traps is

$$\alpha = \frac{k_B}{e}\ln\left(\frac{N}{n - n_{trap}}\right) + \frac{k_B}{e}\ln(2) + \alpha_{vib}. \tag{1.70}$$

Eq. 1.70 applies to narrow band systems where all the N thermally available states are accessible by the carrier concentration n, a scenario applicable to polarons owing to their extremely narrow bandwidths. The narrow band Seebeck coefficient is temperature independent, unlike that for wide band crystalline systems where the Seebeck coefficient goes as a function of $1/T$. In disordered systems such as amorphous silicon, the Seebeck coefficient was also measured to be temperature dependent [72, 73]. The Seebeck coefficients of narrow band systems tend to be large, several times k_B/e, when the fractional occupancy $c = n/N$ is relatively small ~ 0.01, a scenario typical for organic FETs. From this equation, the change in the Seebeck coefficient with charge carrier concentration is

$$\frac{\partial\alpha}{\partial\log(n)} = -\frac{k_B}{e}\ln(10)\left(\frac{n}{n - n_{trap}}\right) = -\frac{k_B}{e}\ln(10) \times f, \tag{1.71}$$

where f is a trap dependent factor $f = 1/(1 - n_{trap}/n)$. Thus, by measuring the Seebeck coefficient as a function of varying carrier concentration, a scenario that can be easily created within a gated organic semiconductor device similar to an FET, one can estimate the parameter f and attain an insight into the fraction of trapped charges that do not participate in charge transport.

Important assumptions and applicability of the narrow band model to bandwidths on the order of a few k_BT

The major assumption in arriving at Eq. 1.70 for the Seebeck coefficient in the narrow band limit was that the bandwidth $W \ll k_BT$. As outlined in sufficient detail in the appendices, this model also holds ground when the bandwidth is as wide as 2 or 3 times k_BT, since for a sufficiently small fractional carrier occupancy c (routinely the case for FET devices), the chemical potential associated with such a narrow band remains relatively unchanged. This is the reason why this formula can safely be applied to organic semiconductors.

The trap states n_{trap} in the narrow band model are assumed to be shallow and lie within an energy range of a few k_BT from the states that participate in transport. In the appendices, different trap density of states have been assumed to sit at different distances from the center

of the charge transport band. It is shown that as long as the trap density of states is within a few $k_{\mathrm{B}}T$ of the states contributing to transport, the quantity n_{trap}/n is relatively gate voltage independent. The factor f is hence dependent only on the total density of shallow traps that exist within the organic semiconductor.

It has also been demonstrated in the appendices that increasing the trap density of states causes an increase in the magnitude of the Seebeck coefficient as well as an increase in the parameter f that governs the slope of the measured Seebeck coefficient with varying carrier concentration.

1.6 Summary

In addition to having potential practical applications for harvesting waste heat, the Seebeck coefficient is also an important tool to probe the physics of charge carrier transport. This Chapter briefly introduced the theoretical framework using which measurements of the charge carrier mobility and the Seebeck coefficient within the channel of high mobility organic field effect transistors can be explained. The Seebeck coefficient is directly associated with the entropy of a single charge carrier within a material, and is hence a fundamental property of charge transport within organic devices. The parameter takes different forms depending on whether carrier transport occurs through wide bands, disordered tail states, or within a narrow band. The Seebeck coefficient, governed by the Mott formula [74, 64], decreases with decreasing temperature in conventional metals. In the case of crystalline inorganic semiconductors where transport occurs in well defined wide bands, the Seebeck coefficient varies with temperature as $\alpha \propto 1/T$ [75, 64]. For disordered inorganic semiconductors such as amorphous silicon, a strong variation of the Seebeck coefficient with temperature is also typically observed [72, 73]. The Seebeck coefficient in organic semiconductors, reported in the forthcoming chapters and elsewhere [66, 70], is found to be temperature independent. The absolute magnitude, the temperature dependence, and the extent to which the Seebeck coefficient is modulated under varying charge carrier density point in the direction of the extent of disorder and the fundamental charge transport mechanism at play.

Chapter 2

Experimental Methods

2.1 Materials: semiconductors and dielectrics

Five different organic semiconductors were used in the experiments contained in this thesis. Poly(2,5-bis(3-alkylthiophen-2-yl)thieno[3,2-b]thiophene) (PBTTT), indacenodithiophene-co-benzothiadiazole (IDTBT), A selenium derivative of diketopyrrolopyrrole-benzothiadiazole (PSeDPPBT), 6,13-bis(triisopropylsilylethynyl)pentacene (TIPS-pentacene) and diketopyrrolo pyrrole-benzotriazole (PDPPBTz). PBTTT and TIPS-pentacene were commercially purchased from Sigma Aldrich. IDTBT was secured from Prof. Iain McCulloch at Imperial College London while PSeDPPBT and PDPPBTz were acquired from Prof. Martin Heeney, also at Imperial College London. These semiconductors, together with their chemical structures, will be described in greater detail in the subsequent Chapters dedicated to them. The two dielectrics used in the devices contained herein were a broad spectrum molecular weight PMMA (purchased from Polymer Source, Canada) and Cytop (purchased from Asahi Glass, Japan).

2.2 Microfabricated integrated chip for Seebeck coefficient measurements

This section outlines the integrated microchip design features and measurement sequence developed to quantify the Seebeck coefficient in solution processed organic semiconductors and its modulation with a gate voltage. The on-chip architecture, designed to contain integrated micropatterned temperature sensors and a heater, is in fact the first successful demonstration of its kind for the intended purpose. Similar on-chip architectures were previously used to probe thermoelectric effects in response to a localized source of heating in nanowires [76, 77, 78] and graphene [79] and enables one to perform high accuracy measurements as a function of both gate voltage and temperature.

Fig. 2.1 shows a schematic and an optical micrograph of the representative device with a patterned layer of an organic semiconductor. The optical micrograph shown here is for the very same device on which the Seebeck coefficient was investigated in the polymer PBTTT,

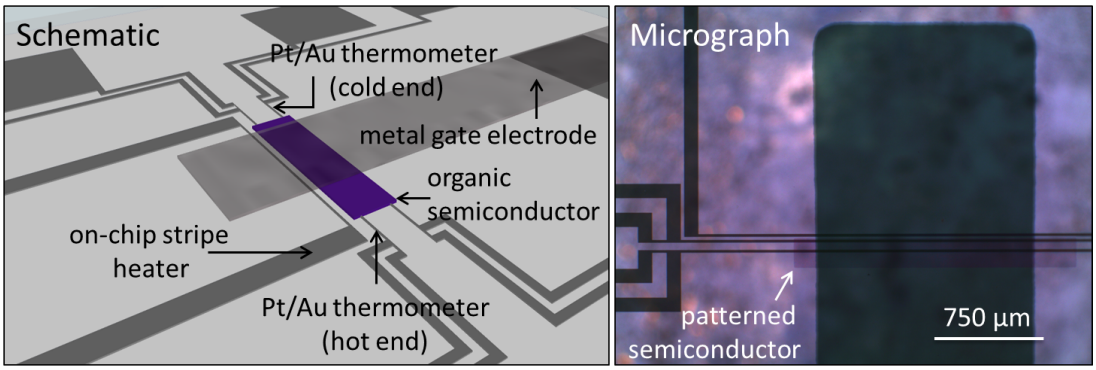

Figure 2.1: Schematic and optical micrograph of the microfabricated integrated chip used to perform measurements of the Seebeck coefficient in solution processed organic semiconductors.

results of which are presented in Chap 3. The micropatterned resistance temperature sensors serve three roles in three separate measurements. In the first measurement, they are used to estimate the temperature difference across the organic semiconductor by measuring their individual resistances as a function of the on-chip heater power. In the second measurement, they are used as thermal voltage probes to measure the built-in thermal voltage across the organic semiconductor as a function of heater power (temperature differential). In the third and final measurement, they are used as source and drain electrodes to measure the transfer and output characteristics of the device when operated as a field-effect transistor in the absence of a temperature gradient. In this Chapter, the steps involved in these three measurements are outlined using the device with a patterned layer of the organic polymer PBTTT as an example. A similar sequence of measurement steps was performed on the other organic semiconductor devices presented in this thesis.

On a glass substrate, the two thermometers and a heater comprising 17 nm platinum (Pt) and 3 nm gold (Au) were patterned using optical lithography. Since the thermometers were also designed to act as source and drain electrodes for charge carrier injection while operating the device as an FET, the specific choice of metal bilayer was necessary. The idea was to have a thermometer whose resistance is dominated by Pt so as to capitalise on Pt's linear variation of resistance with temperature, but also include a surface layer of Au to ensure injection from Au into the organic semiconductor. In the case of the organic semiconductor PBTTT, although in principle Pt should provide good hole injection due to its high work function, we preferred to use Au to make our work directly comparable to studies on PBTTT FETs in literature [80]. It is worth mentioning here that, should the evaporated 3 nm Au layer not be entirely conformal thus necessitating injection from Pt into semiconductors like PBTTT within the FET, injection will not be significantly hindered for the aforementioned reason. A layer of the organic semiconductor was solution processed on the chip containing the heater and sensors. The purple region in Fig. 2.1 shows the patterned layer of the organic semiconductor. It is of paramount importance to pattern the organic semiconductor on the chip to avoid a possible crosstalk between the heater and the thermal voltage probes during a measurement of the thermal voltage. In the case of

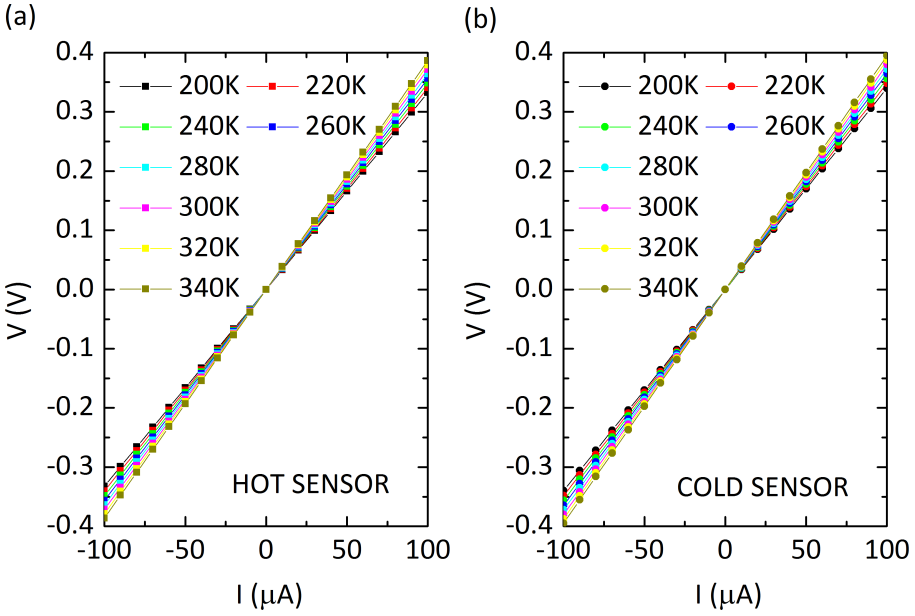

Figure 2.2: Temperature dependent IV curves of the two resistance temperature sensors on the hot and cold ends of the patterned organic semiconductor (shown here for the PBTTT device).

PBTTT and PSeDPPBT, a 300 nm layer of PMMA was used as a dielectric over the patterned organic semiconductor and the device was gated with 20 nm Al, evaporated through a shadow mask. 500 nm Cytop was used for IDTBT and TIPS-pentacene based devices. The broad dark region in the micrograph of Fig. 2.1 is the gate electrode. The channel length between the two thermometers is 50 μm, the distance between the heater and the hot sensor is 20 μm, and the width of each sensor is 20 μm. As a typical example of the dimensions of the patterned organic semiconductor, the PBTTT active layer was 2 mm in width and $\sim$ 200 μm in length.

2.3 Calibration of the on-chip thermometers

Prior to the measurement of the Seebeck coefficient, the two Pt/Au bilayer thermometers on either side of the patterned organic semiconductor were calibrated in two stages. In the first stage, two-point resistances of the sensors on the hot and cold ends were measured using an Agilent Semiconductor Parameter Analyser (SPA) 4155B. The resistances of the on-chip sensors are on the order of several kΩs, thus justifying the use of a two-point measurement. Fig. 2.2 shows the IV characteristics of the hot and cold thermometers at temperatures spanning 200 K - 340 K. The current was swept from -100 μA to $+100$ μA in steps of $+10$ μA and the voltage was measured simultaneously. The slopes extracted from the IV curves shown in Fig. 2.2 are measures of the resistances of the thermometers at various temperatures. These resistances are plotted as a function of temperature shown in Fig. 2.3.

The slope of the resistance versus temperature shown in Fig 2.3 is the temperature coefficient of resistance (TCR) for the on-chip thermometers and is a measure of the change in resistance of

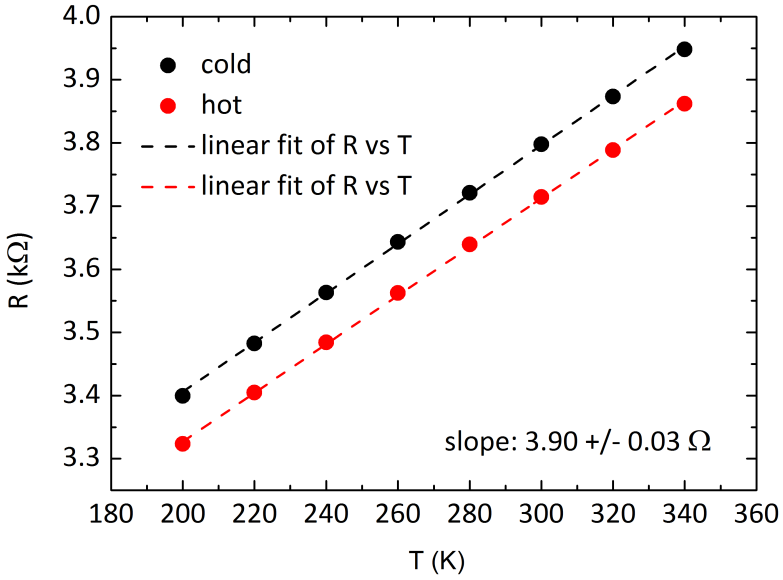

Figure 2.3: Estimation of the temperature coefficient of resistance (TCR) of the two thermometers on-chip (shown here for the PBTTT device).

the hot and cold thermometers on-chip for a degree rise in temperature. For the PBTTT device investigated in this thesis, the TCR was 3.9 ± 0.03 Ω/K. There was a variation in the TCR across different devices and hence every chip needed to be calibrated independently. A linear fit was used to estimate the slope of the data points in Fig. 2.3. This is justified to within a reasonable approximation for the Pt/Au bilayer temperature sensors. Should the sensors have been composed of pure Pt, an ideal fit of the data points would be got by using the Callendar-Van Dusen equation for the change in resistance with temperature in Platinum. The Callendar-Van Dusen equation is a non-linear equation that describes the relationship between resistance and temperature of pure platinum resistance thermometers.

Once the TCR for the two temperature sensors was estimated, the change in the two-point resistance of each sensor was measured using an SPA as a function of the on-chip heater power, shown in Fig. 2.4. The measurement of the on-chip resistances as a function of heater power was performed in sampling mode where the voltage across the heater was set to a specific value thus determining the power. After waiting for five seconds to let the chip achieve thermal equilibrium, twenty data points of the resistance were sampled with a long integration time. This sequence was repeated for every heater power to generate the data shown in Fig. 2.4. It should be mentioned here that the resistance at every heater power was extracted from an IV curve similar to those shown in Fig. 2.2. The resistances measured as a function of heater power were then converted into temperature using the previously determined TCR. These temperatures are shown on the right hand side of Fig. 2.4.

Once the temperatures on the two ends of the organic semiconductor were determined, the next step in estimating its Seebeck coefficient is to determine the thermal voltage built-in for the

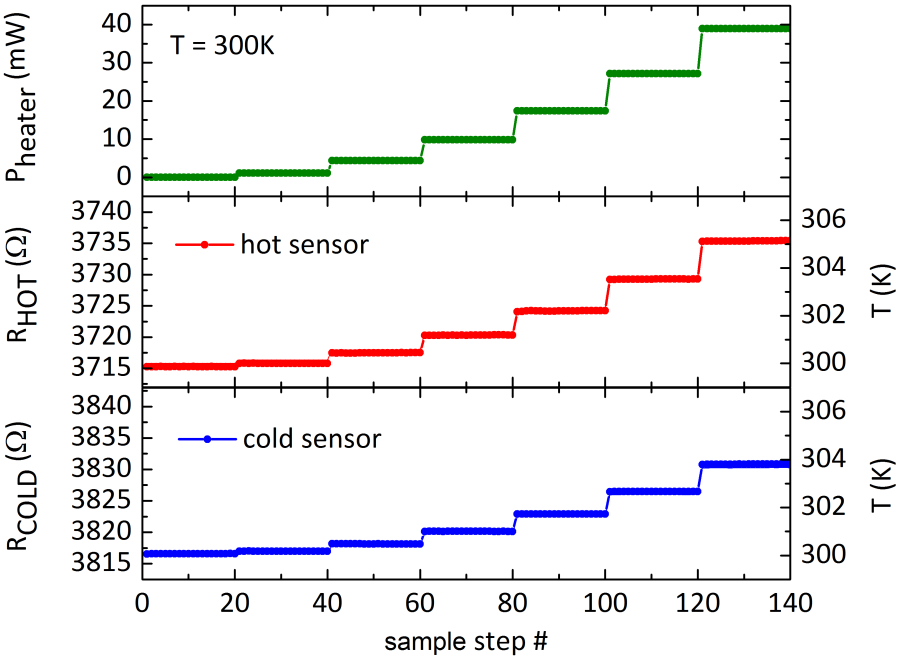

Figure 2.4: Measured resistances of the two thermometers on-chip and their variation with heater power (shown here for the PBTTT device).

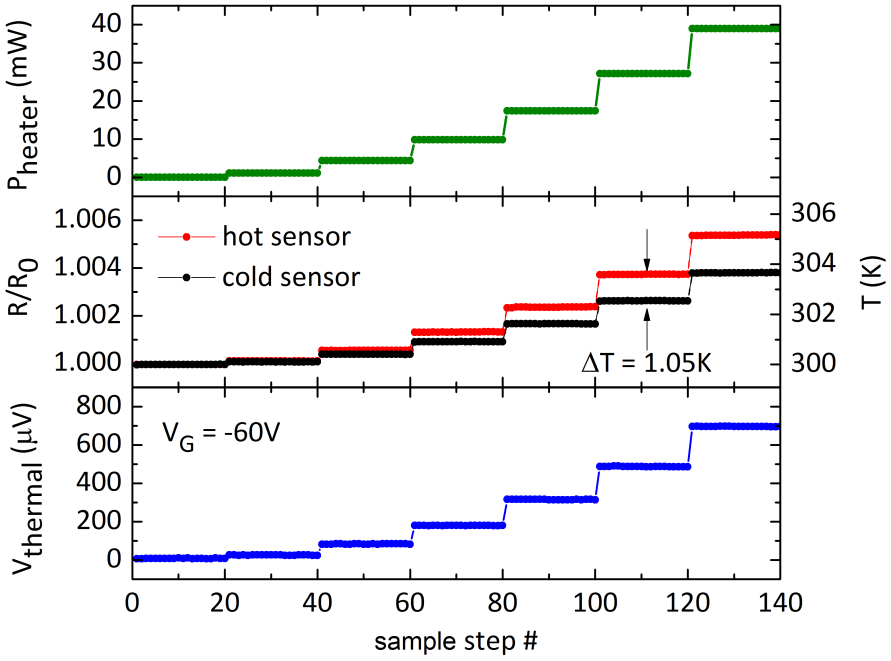

Figure 2.5: Built-in thermal voltage across the organic semiconductor as a function of heater power (shown here for the PBTTT device).

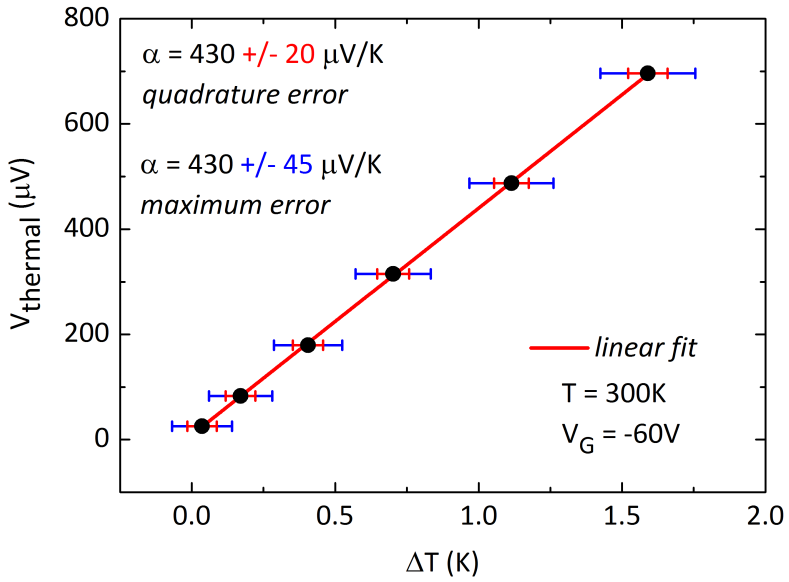

Figure 2.6: The slope of the measured thermal voltage versus the temperature difference yields the Seebeck coefficient (shown here for the PBTTT device).

same sweep in heater power. The thermal voltage is measured across the organic semiconductor, between the same two Pt/Au electrodes previously calibrated as thermometers. The measurement of the built-in thermal voltage is a current-devoid measurement, where one of the voltage probes is set to ground, and the other is left floating. The ground was normally set at the hot end so that the sign of the built-in thermal voltage directly reflected the type of charge carriers within the system, either holes or electrons. The thermal voltage measurements were also performed using the SPA, to take advantage of the high input impedance of the SPA's source measure units (SMUs). Fig. 2.5 shows a measurement of the thermal voltage (blue) as a function of heater power. The sweep in the heater power is modulated parabolically up to 40 mW by increasing the applied voltage across the heater in steps of 2 V. As can be seen, the thermal voltage trace is also parabolic, since it is expected to follow the trace in heater power. The measurement of the thermal voltage shown in Fig. 2.5 was performed under a gate voltage of -60 V. The middle panel of Fig. 2.5 re-plots the resistances shown in Fig. 2.4, to illustrate the magnitude of temperature difference associated with the measured thermal voltage.

Finally, when the thermal voltage and the temperature difference across the patterned organic semiconductor were measured, the slope of the thermal voltage versus the temperature difference is an estimate of the Seebeck coefficient. Fig. 2.6 illustrates this. The same procedure was repeated at different gate voltages and different temperatures to determine the gate voltage modulation and the temperature variation of the Seebeck coefficient of the organic semiconductor film under investigation.

2.4 Measurement errors in the Seebeck coefficient

Two estimates of the error in the measured Seebeck coefficient, α, are quoted in Fig. 2.6, a quadrature error and a maximum error. In estimating these errors on the Seebeck coefficient, the error in every measured contributing quantity to the Seebeck coefficient was determined and propagated bottom-up. The TCR of the thermometers on-chip was measured to be 3.9 with an error of ± 0.03 Ω/K. This error is the standard error computed by the software Origin used to perform a linear fit. Labeling the resistances of the thermometers on the hot and cold ends of the organic semiconductor at 300 K in the absence of a heater power as $R_{\text{hot, 300K}}$ and $R_{\text{cold, 300K}}$, and those measured under a heater power P as $R_{\text{hot, P}}$ and $R_{\text{cold, P}}$, the temperature difference at every heater power P is calculated using Eq. 2.1.

$$\begin{aligned}\Delta T_{\text{P}} &= T_{\text{hot, P}} - T_{\text{cold, P}} \\ &= \left(300 + \frac{R_{\text{hot, P}} - R_{\text{hot, 300K}}}{\text{TCR}}\right) - \left(300 + \frac{R_{\text{cold, P}} - R_{\text{cold, 300K}}}{\text{TCR}}\right)\end{aligned} \tag{2.1}$$

The error in the measurement of resistance was ± 0.1 Ω, and the resistance of the thermometer was on the order of a few kΩs as shown previously. The standard error $\delta V_{thermal}$ in the measurement of the thermal voltage was consistently less than ± 2 μV, smaller than the size of the data points in Fig. 2.6. The maximum error $\delta\alpha$ in the measured Seebeck coefficient $\alpha = \Delta V/\Delta T$ is computed as,

$$\frac{\delta\alpha}{\alpha} = \frac{\delta V_{thermal}}{V_{thermal}} + \frac{\delta\Delta T}{\Delta T} \tag{2.2}$$

while the quadrature error is

$$\left(\frac{\delta\alpha}{\alpha}\right)^2 = \left(\frac{\delta V_{thermal}}{V_{thermal}}\right)^2 + \left(\frac{\delta\Delta T}{\Delta T}\right)^2. \tag{2.3}$$

$\delta\Delta T$ reflects the combined error of the two bracketed quantities in Eq. 2.1, each of which include errors in the measurement of resistance and TCR propagated either using the maximum error admissible, or in quadrature as the case may be. It should be mentioned that the dominant contribution to the error in the Seebeck coefficient α comes from the error estimate of ΔT since the error in the thermal voltage V_{thermal} is insignificant. At 300 K and a gate voltage of $\text{V}_\text{G} = -60$ V, the Seebeck coefficient in PBTTT is about 430 to 460 μV/K, with an error estimate that is between 5-10 % this value. The sign of the Seebeck coefficient is positive, consistent with hole transport. A number of data points per heater power were accumulated in the construction of Fig. 2.5 only to compute the errors and illustrate consistency in the measurement over time.

2.5 Field-effect modulation of the Seebeck coefficient

When performing Seebeck measurements as a function of applied gate voltage, only one data point per heater power was sampled in order to avoid stressing the device. Such a sequence of gate-bias modulated thermal voltage measurements is illustrated in Fig. 2.7. The gate bias is

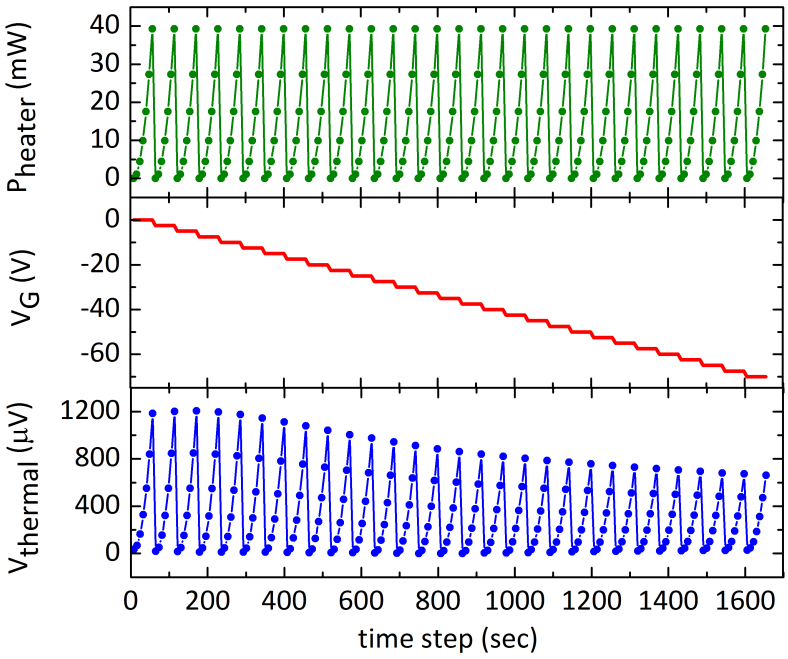

Figure 2.7: Measured thermal voltage as a function of a parabolic sweep in heater power at different gate voltages in PBTTT. For gate voltages more negative than −10 V, the measured thermal voltage reduces with increasing gate voltage. The offsets in the thermal voltage measurement are always less than 20 μV (shown here for the PBTTT device).

ramped in steps of −2.5 V. At every applied gate voltage, the heater is swept parabolically and the thermal voltage measured. The Seebeck coefficients are then extracted from the slope of the measured thermal voltage versus applied temperature differential at every applied gate bias as shown in Fig. 2.8. The result of such a gate bias modulated Seebeck coefficient measurement scan in PBTTT is illustrated in Fig. 2.9.

The physical interpretation of the gate modulated Seebeck coefficient measurements presented here using the PBTTT device as an example, will be the focus of Chap. 3 and in the subsequent Chapters that follow. It will be shown how such a measurement can give an important insight into the quantification of disorder in organic semiconductors.

The next section illustrates the mask design and detailed fabrication steps involved in achieving the Seebeck devices for our measurements.

2.6 Photomask design and fabrication

The photomask for Seebeck devices was designed specifically for this PhD thesis. The CAD software used for this purpose was Layout Editor (http://www.layouteditor.net/), an easy to use program using which MEMS and IC designs can be made. The GDS files of the Seebeck patterns were transferred onto a photomask at the Nanofabrication facility within the Cavendish Laboratory's Semiconductor Physics group using the expertise of Jonathan Griffiths. A snapshot of the GDS file of the entire mask is shown in Fig. 2.10. The four inner circles are only drawing

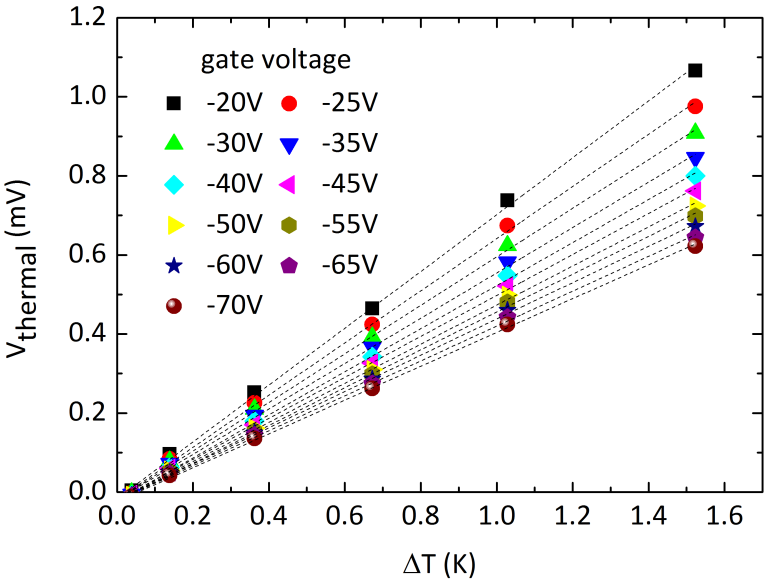

Figure 2.8: V_{thermal} versus ΔT for gate voltages from -20 V to -70 V (shown here for the PBTTT device).

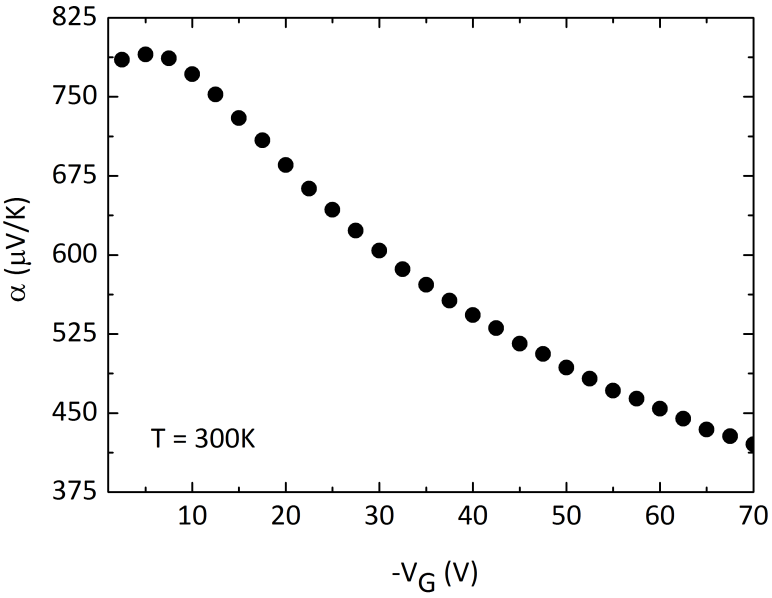

Figure 2.9: Extracted Seebeck coefficient α as a function of applied gate voltage (shown here for the PBTTT device).

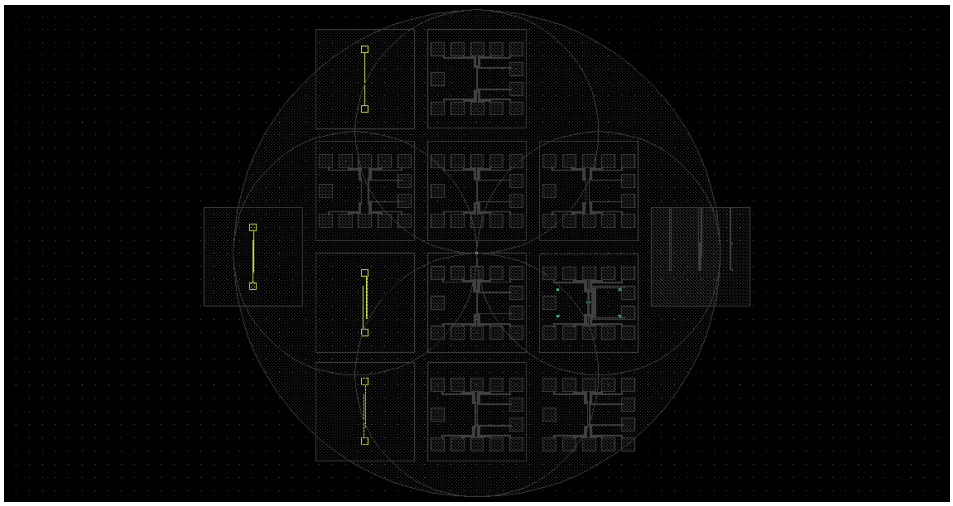

Figure 2.10: Snapshot of the entire photomask GDS file with many Seebeck devices of varying inter-electrode distances. The mask also contains a pattern for a hall bar.

guides for the maximum area that can be exposed at any given time using one of the mask holders at the Karl Suss MJB3 mask aligner. These circles do not appear on the actual photomask. The mask contained many patterns with varying distances between the two sensors/electrodes; 20, 50, 100, 250, 500 and 1000 μm. A stripe heater was positioned 20 μm from one of the electrodes. The allowance was made for doing a four point probe measurement of the resistances of the electrodes. The pattern that was used for all the devices in this thesis had an inter-electrode distance of 50 μm. This specific pattern is shown in Fig. 2.11. In addition to the designs with a stripe heater, other wriggly heater patterns are also included on this photomask.

The photomask also includes a pattern that can be used for Hall and Nernst measurements on solution processed materials. The Hall bar that can be patterned has dimensions of 250 μm in length and 50 μm in width. There are two transverse Hall probes 10 μm wide that reach into the middle of the Hall bar. Fig. 2.12 shows a pattern of the Hall bar, with its transverse probes and a heater on the side for Nernst effect measurements. Fig. 2.13 (a) shows a close up of the Hall bar pattern. The bright green crosses in the center are alignment markers used for subsequent lithographic steps. Fig. 2.13 (b) is the pattern of the oxide or organic layer that overlaps the electrodes shown in Fig. 2.13 (a). The patterns on the GDS file shown here are inverted compared with what is on the actual photomask. The pattern of the oxide or the organic is a vertically dissected-H bar. Charge injection takes place along the 3.5 mm long electrodes and is funneled into the bar in the center.

This pattern was tested on a solution processed oxide device gated with a high-k dielectric and was shown to be a successful design. Proof-of-concept measurements of the Hall effect are included in the appendices, since the focus of the Chapters in this thesis is on Seebeck measurements. It is hoped that the members of the Optoelectronics group interested in Hall measurements will put this design to use in the future. The 13 large square pads that contact the electrodes and the heater on the Hall device, and 11 pads for the Seebeck device, were designed

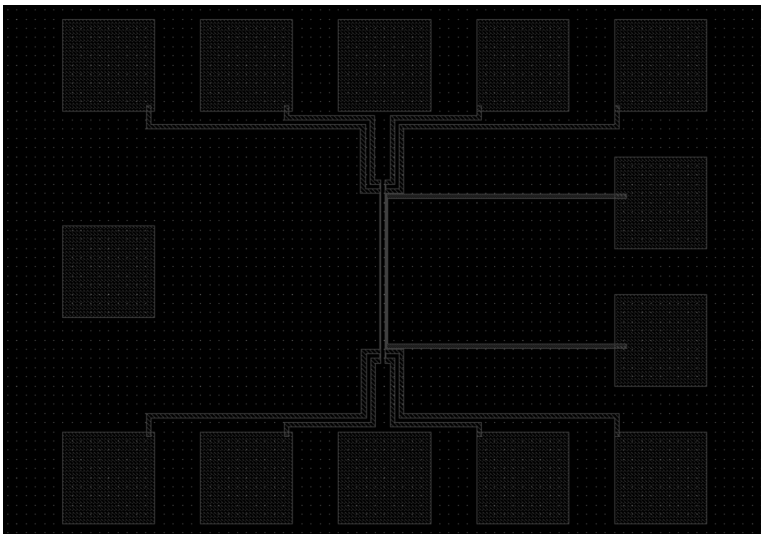

Figure 2.11: Seebeck device design with a stripe heater and a 50 μm inter-electrode distance. It is difficult to resolve the 20 μm gap between the heater and one of the electrodes in the device on this image.

specifically to be compatible with an insert designed and built alongside. This insert, described in more detail in the appendices, was machined in the Cavendish Workshop with the help of Ron Hodierne, formerly at the Cavendish Laboratory.

2.7 Organic device fabrication

This section outlines the various steps used to fabricate organic electronic devices for Seebeck and FET measurements. The outline presented here is written with the intention of being instructional and will hopefully prove useful for those wishing to replicate the results presented herein. The entire fabrication was done in the Microelectronics Cleanroom of the MRC building in the Cavendish Laboratory.

2.7.1 Substrate cleaning

A 1317F 700 μm thick Corning glass slide of 8 cm $\times$ 4 cm was diced into smaller substrates each with an area of 2 cm $\times$ 2 cm using a diamond scriber pen. The individual substrates were then sonicated in a solution containing Decon 90 detergent, followed by DI H_20, Acetone and IPA each for 10 minutes. Samples were then blow dried in N_2, placed on a glass petridish and ashed in a TEGAL oxygen plasma asher for 10 minutes at 250 W. After the plasma ashing step, the samples were once again sonicated in Acetone and IPA for 3 minutes each. They were then blow dried in N_2.

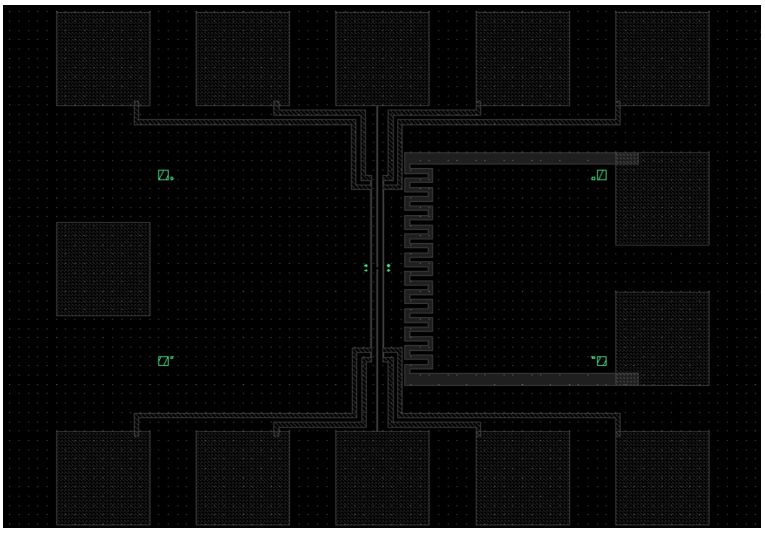

Figure 2.12: Mask design to fabricate Hall bars with a channel length of 250 μm and a channel width of 50 μm. This mask can also potentially be used for Nernst effect measurements for which the wriggly heater was designed next to the hall bar.

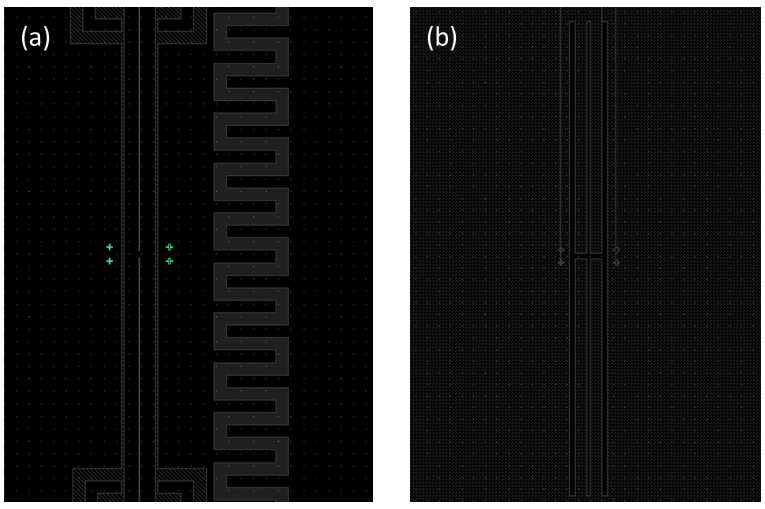

Figure 2.13: Close up of the photomask Hall bar patterns. (a) A close up showing the center of the Hall device electrodes (Fig. 2.12). (b) The mask pattern showing the vertically dissected-H shape of the patterned Hall bar.

2.7.2 Optional layer of polyimide for TIPS-pentacene devices

In the case of TIPS-pentacene devices, a layer of polyimide PI2525 from HD Microsystems was processed into a layer on glass to prevent de-wetting of the organic film. Polyimide was diluted with NMP in a ratio 1:7 and heated at 80 °C for 20 minutes to get a homogeneous solution. The solution was spin coated onto the substrates in air at 2500 rpm for 50 seconds and the substrates placed on a hot plate for a few minutes at 80 °C for the film to dry. The samples were then taken into the N_2 glovebox and cured, first at 160 °C for 1 hour and then at 300 °C for 3 hours. The samples were then cleaned in Acetone and IPA for 5 minutes each and dried in N_2 before photolithography.

2.7.3 Photolithography

Photoresist LOR 5B was spin coated onto the substrates at 6000 rpm for 30 seconds from a solution filtered using a PTFE Filter with 5 μm pores. The substrates with LOR 5B were baked at 190 °C for 5 minutes on a hotplate. S1813 photoresist was then spin coated at 6000 rpm for 30 seconds and baked at 120 °C. The bilayer resist is needed to achieve an undercut necessary for high-throughput photolithography. Using a photomask having a minimum feature size of 10 μm, the required pattern was transferred onto the resist using a Karl Suss MJB3 mask aligner with an exposure time of 12 seconds in the soft contact mode. The samples were then developed in MF319 with slight agitation for 35 seconds, rinsed in H_2O for 1 minute and blow dried in N_2. An optional following step was to place the samples in the plasma asher for a few minutes after this to clean the exposed glass areas of any photoresist.

2.7.4 Fabrication of device electrodes

Bi-layer electrodes of Pt/Au in the case of the PBTTT and PSeDPPBT devices of this thesis were got by first sputtering 17 nm Pt. The vacuum was then broken and the devices were loaded into a four turret evaporator where 3 nm Au was evaporated. The vacuum level of the sputter coater was 2×10^{-6} mbar and that of the evaporator was in the 10^{-7} mbar range. For IDTBT and TIPS-Pentacene devices, a Cr/Au bi-layer was used. 3 nm Cr acted as an adhesion layer followed by 11 nm Au. Both Cr and Au were evaporated in the four turret evaporator. The devices with a uniform coating of the bilayer was then placed in a developer solution MF319 for an hour for the lift off to take place. After successful lift-off, the samples were sonicated in Acetone and IPA for 10 minutes each, followed by blow drying them in N_2.

2.7.5 Optional layer of SAM for TIPS-pentacene devices

A self assembled monolayer (SAM) of Pentafluorothiophenol (PFBT) was used to modify the Au electrodes to improve injection into TIPS-pentacene. For this, the substrate with the Au electrodes was ashed using the oxygen plasma asher for 1 min at 150 W. This modifies the work function of Au for improved hole injection. Right after, PFBT was spin-coated onto the chip

from a solution of 10 μl:4 ml (PFBT:IPA). The solution was first dropped on the chip and left to lay there for two minutes. This helps PFBT self-assemble on the Au electrodes to the extent it can in this short time. The chip was then spin at 1000 rpm for 1 minute. Right after, IPA was splashed with intensity on the chip for 30 seconds to ensure that no solution remains in unwanted regions.

2.7.6 Solution-processed organic semiconductors

The organic active layers were all processed from dissolved solutions of the organic material in a solvent. In the case of PBTTT, PSeDPPBT, IDTBT and the linear and branched PDPPBTz, Dichlorobenzene (DCB) was used as the solvent. For TIPS-Pentacene, the solvent used was 1,2,3,4-Tetrahydronapthalene (Tetralin). 10 mg of the organic material was dissolved in 1 ml solvent. The organic materials were dissolved in the solvent by heating the solution to 80 °C in an N_2 glovebox and stirring the vial manually till complete dissolution was achieved. The process takes between 30 minutes and an hour when on the hot plate.

To achieve a terraced phase active layer of PBTTT, the solution was spin coated at 1000 rpm for 60 seconds from a hot solution of PBTTT using glass pipettes. Both the solution and the pipettes were maintained at 110 °C. The sample was annealed at 180 °C for 5 minutes after which the hotplate was gradually cooled to room temperature. When the hot plate reached 100 °C, the samples were removed from them and placed on a metal slab thus quenching the device. The thickness of the films was about 60 nm.

For an active layer of PSeDPPBT, the samples were spin coated at 1000 rpm for 60 seconds and annealed at 200 °C for two hours.

$l-$ and $b-$ PDPPBTz were spun with the same spinning parameters as PSeDPPBT and annealed at 100, 200 and 300 °C as the work done on them as part of this thesis constituted an opitmisation of device performance.

IDTBT active layers were arrived at by annealing the film at 100 °C for 10 minutes. The spin parameters were again 1000 rpm for 60 seconds.

To get a TIPS-Pentacene active layer, the solution was spin coated at 1000 rpm for 60 seconds in the glovebox followed by an annealing step at 100 °C for 5 minutes.

2.7.7 Device patterning process

In the case where an unpatterned device would serve the purpose, a dielectric layer was directly spin coated onto the organic active layer. The dielectric layers used in this thesis were PMMA in the case of PBTTT, PSeDPPBT and $l-$, $b-$ PDPPBTz or Cytop in the case of TIPS-pentacene and IDTBT. 300 nm PMMA was achieved by spinning it from a solution of n-Butyl Acetate at 1000 rpm for 120 seconds. The concentration of PMMA in n-Butyl Acetate was 45 mg in 1 ml. The PMMA layer was annealed at 80 °C for 30 minutes. 500 nm Cytop was achieved by spinning it from a solution diluted with the Cytop solvent CT-180 in the ratio 3:1. 3 parts of Cytop in 1 part of the Cytop solvent. The solution was spin at 500 rpm for 3 seconds followed immediately

by 2000 rpm for 60 seconds. The ramp to 500 rpm was 1 second and the ramp to 2000 rpm was 3 seconds. The Cytop layer was dried at 90 °C for 20 minutes. The above relevant steps were performed in the N_2 glovebox immediately after solution processing the organic active layer.

In the case of the Seebeck device requiring a patterned organic semiconductor, a sacrificial layer of Cytop from a solution of 1:2, 1 part Cytop in 2 parts Cytop solvent, was spin coated on the active organic layer. The layer was spin at 1000 rpm for 60 seconds and baked at 90 °C for 20 minutes. The device was then taken out of the N_2 glovebox and loaded into the four turret evaporator where 1 nm Al was evaporated onto Cytop. This was needed to change the surface energy of Cytop and make it easier to spin coat a resist layer on it. The 1 nm Al layer was evaporated under a fairly high pressure of 10^{-3} to 10^{-4} mbar. After the deposition of this layer, S1813 was spin coated onto the device at 4000 rpm and baked at 80 °C for 5 minutes. Photolithography was then done using the mask whose pattern was to be transferred onto the organic layer. The exposure was done in four steps of 3 seconds each, rather than one long exposure for 12 seconds. This was proven to minimise the number of air gaps or bubbles that were formed between the organic and Cytop layers owing to a tension that builds in Cytop when S1813 alters on exposure. The device was then subject to development in MF319 for 35 seconds and carefully blow dried in N_2 to avoid accidentally delaminating Cytop. The dimensions of the patterned organic layer on the Seebeck device were either 1 mm $\times$ 200 μm or 2 mm $\times$ 200 μm. The device was then placed on a petridish in the oxygen plasma asher such that the device is directly over one of the metal bars of the cage. Plasma ashing was done at 300 W in steps of 3 minutes with a gap of 5 minutes. This procedure was adopted to avoid heating the device or heating the entire asher. To ash away the sacrificial layer as well as the organic layer for the polymers, a total ashing time of around 8 to 10 minutes was required. In the case of TIPS-pentacene, around 20 minutes in total was required. Once the organic layer was patterned by ashing, 3M Scotch tape was gently laid over the devices and the devices together with the tape were taken back into the glovebox where the Scotch tape was pealed of. The scotch tape takes with it the Cytop-resist bi-layer over the patterned organic. Finally, the organic dielectric was deposited on the device using the parameters outlined at the start of this section.

2.7.8 Evaporation of a gate electrode

After processing the organic semiconductor and the organic dielectric layer, 20 nm Al was evaporated onto the device to define the gate electrode. The evaporation was done through a shadow mask. The width of the gate electrode was 1.5 mm. Fig. 2.14 shows a schematic of a completed Seebeck device fabricated using the sequence of steps described.

2.8 Summary

This Chapter introduced the on-chip device architecture, together with the measurement sequence, developed to perform gate voltage modulated Seebeck coefficient measurements on solution

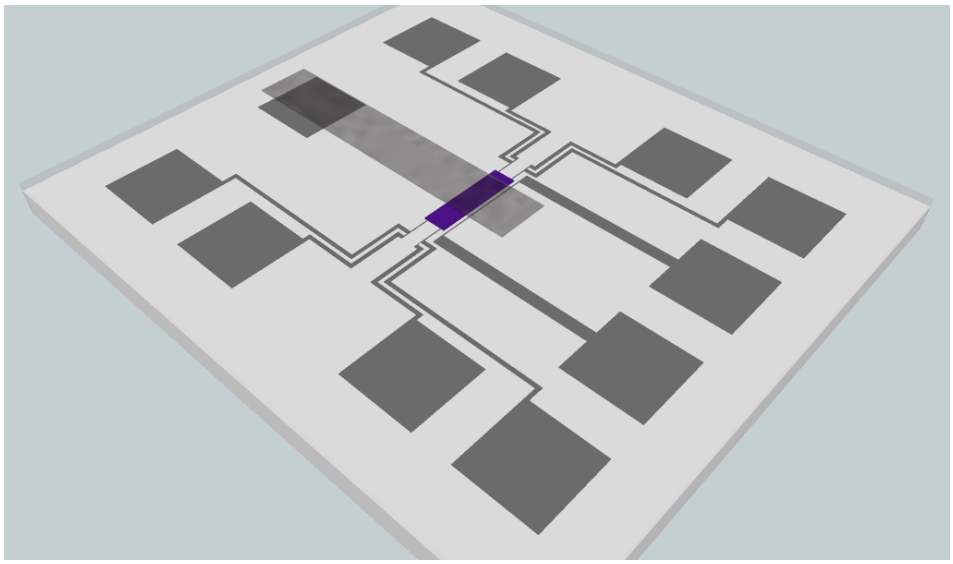

Figure 2.14: Schematic of a complete Seebeck device involving all the outlined fabrication steps. Each of the electrodes is connected to four contact pads and the heater to two. The organic semiconductor is patterned to avoid overlap with the heater. The metal gate electrode lies on either a 300 nm PMMA or a 500 nm Cytop dielectric layer. The two unconnected contact pads are not shown.

processed organic semiconductors. The detailed fabrication steps needed to build these Seebeck devices were also outlined. In the following Chapters, the physical interpretation of the measured Seebeck coefficient in a variety of organic semiconductors will be discussed.

Chapter 3

Seebeck coefficient in PBTTT

3.1 Introduction to PBTTT

Poly(2,5-bis(3-alkylthiophen-2-yl)thieno[3,2-b]thiophene (PBTTT), shown in Fig. 3.1 with a specific alkyl chain $C_{14}H_{29}$, is a liquid crystalline semiconducting co-polymer comprising two monomer units, 4,4-dialkyl 2,2-bithiophene (BT) and thieno[3,2-b]thiophene (TT). Among semiconducting co-polymers based on thiophene units, PBTTT has emerged as a classic example of how the optimisation of inter-molecular packing plays an important role in achieving good electrical transport within a polymer [81].

Within a polymer film, individual PBTTT monomers order into a coplanar stack along the backbone of the monomer. Shown in Fig. 3.2 (a) is a cross-sectional view of such an ordering of PBTTT monomers when looking down along the conjugated backbone of the polymer. The conjugated polymer backbones tend to line up face to face with each other, with a slight tilt of 22° from the substrate normal as shown. The necessity for a tilt in the conjugate backbone is a consequence of energy minimisation within the unit cell of PBTTT, and was predicted using density functional theory [82]. The face to face arrangement, sometimes referred to as π-stacked lamella, is made possible due to the backbone planarity of PBTTT. The alkyl side chains in PBTTT are known to align themselves at an angle of 45° to the substrate normal as determined by near-edge X-ray absorption fine structure (NEXAFS) spectroscopy. Substantial interdigitation of alkyl chains between polymers is another important feature seen in PBTTT as shown in Fig. 3.2 (b), and remains a signature packing motif to achieve high order within a polymer film resulting in improved charge transport.

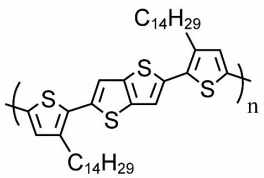

Figure 3.1: Structure of C_{14}-PBTTT.

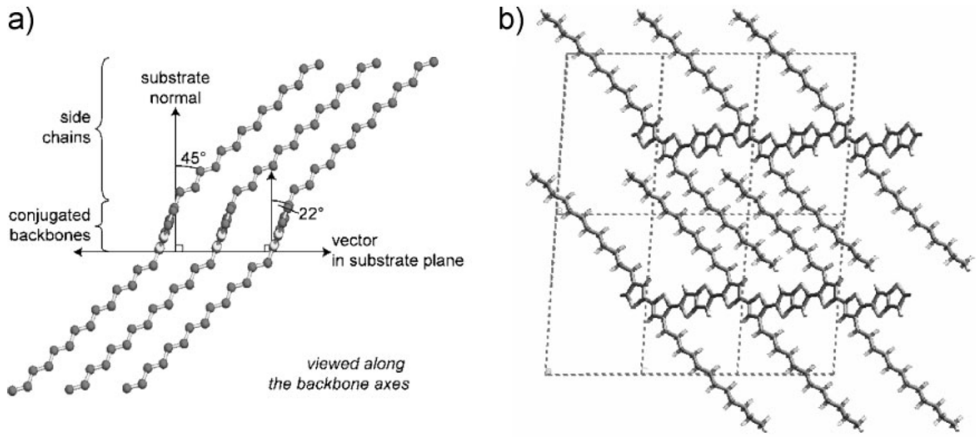

Figure 3.2: (a) Tilted edge-on arrangement of PBTTT monomers on a substrate (b) Interdigitation of the alkyl side chains within a film of PBTTT. The alkyl chains on PBTTT are known to align themselves at 45° to the substrate normal. Image adapted from [81].

PBTTT is known to choose between three possible phases within a film, depending on the temperature at which the film is annealed. Although as cast films of PBTTT have crystalline domains within the film, the texturing is far from ideal [83]. When the film is annealed through a first phase transition to temperatures between 120 °C and 180 °C, a mesophase indicating a smectic-like order can be achieved. This temperature range is known to cause a melting of the side chains, which when crystallized on cooling, pack into a well ordered interdigitated structure. This phase is often referred to as the terraced phase, since large terraces are seen in the morphology of the film upon re-crystallisation. These terraces have domain sizes on the order of many hundred nanometers and are a direct visualisation of the nanoscopic π-stacked lamella within the film. Field-effect mobilities of PBTTT in the terraced phase with a C_{14} side chain have been reported to be between 0.1 and 1 cm^2/Vs in the saturation regime [81, 50].

When PBTTT films are annealed through a second phase transistion to 250 °C, a phase called the ribbon phase can be realised. These high temperatures instigate backbone melting of PBTTT and the formation of crystalline nanoribbons with a width characteristic of a fully extended polymer chain backbone [50]. Mi Jung Lee and co-workers observed field-effect mobilities up to 0.48 cm^2/Vs in ribbon phase PBTTT. It is remarkable to note that in the ribbon phase, a mobility anisotropy is observed where the mobility along the PBTTT backbone can be upto 10 times that along the $\pi - \pi$ stacking direction [50].

Conjugated π-electron rich thiophenes such as PBTTT are also known to be susceptible to thermodynamic electrochemical oxidation. Such an oxidation is known to occur when the HOMO energy level of the polymer is less than 4.9 eV from the vacuum energy level [84]. The theoretical estimate of the HOMO level of PBTTT is 5.1 eV, very close to this theoretical limit thus causing unavoidable oxidation over time. Oxidative doping typically shows its presence as an increased OFF current within a field effect transistor as demonstrated previously [81], as well as in the devices studied in this thesis.

The Seebeck coefficient was never previously measured in a thiophene based crystalline polymer such as PBTTT. In this Chapter, gate modulated Seebeck coefficient measurements using the previously introduced microfabricated integrated chip with a patterned terraced phase PBTTT film will be illustrated, and the physics behind the observations will be the focus of discussion.

3.2 Transition from bulk to accumulation in PBTTT

It was mentioned that the microfabricated chip developed for Seebeck coefficient measurements had the additional functionality of being operated as an FET. Fig. 3.3 and Fig. 3.4 compare the gate-modulated source-drain current with the Seebeck coefficient measured in two different PBTTT FETs. Due to variations in the semiconductor patterning conditions, the device in Fig. 3.3 had a higher mobility (≈ 0.1 cm^2/Vs) than the device in Fig. 3.4 (≈ 0.01 cm^2/Vs) at 340 K. In both devices the Seebeck coefficient is approximately gate-voltage independent at low gate voltages between 0 V and $V_G = -10$ to -20 V. At higher gate voltages the Seebeck coefficient decreases linearly on a semi-log scale. The absolute magnitude of the Seebeck coefficient is several hundred μV/K, typical for semiconductors.

Fig. 3.3 (Fig. 2.9) demonstrates for the first time the presence of a relatively gate-voltage independent regime in the Seebeck coefficient of an organic semiconductor at low gate bias. A similar hump in the Seebeck coefficient at low gate voltage was seen in pulse laser deposited amorphous oxide thin film transistors in the past [85] and was explained in the context of tail states close to the bottom of the conduction band. We offer a different explanation for our PBTTT devices. After the full processing of the on-chip integrated devices, our PBTTT FETs have only a relatively low ON-OFF current ratio of 10^2-10^3, i.e., they exhibit a non-negligible OFF current. This feature is in all likelihood tied to oxidative doping within the organic polymer film. At low gate voltages, the measured drain current has a significant contribution from transport through the unintentionally doped bulk of the semiconductor, which is only weakly affected by the gate voltage (Fig. 3.3 and Fig. 3.4). At higher gate voltages, when the drain current becomes greater than than 10^{-7} A, conduction starts to be dominated by the gate-induced accumulation layer. In such a situation the Seebeck coefficient α can be expressed in the form

$$\alpha = \left(\frac{\alpha_{bulk}\Sigma_{bulk} + \alpha_{accu}\Sigma_{accu}}{\Sigma_{bulk} + \Sigma_{accu}} \right), \tag{3.1}$$

where the subscripts *bulk* and *accu* refer to contributions to the Seebeck coefficient and conductance from the bulk and the accumulation layer of the FET, respectively. At low gate voltage Σ_{bulk} becomes comparable to Σ_{accu} and the measured Seebeck coefficient increasingly reflects α_{bulk} which is expected to be only weakly gate voltage dependent. When the accumulation layer starts to dominate conduction at high gate bias, the total measured Seebeck coefficient is determined by the gate voltage dependent α_{accu}.

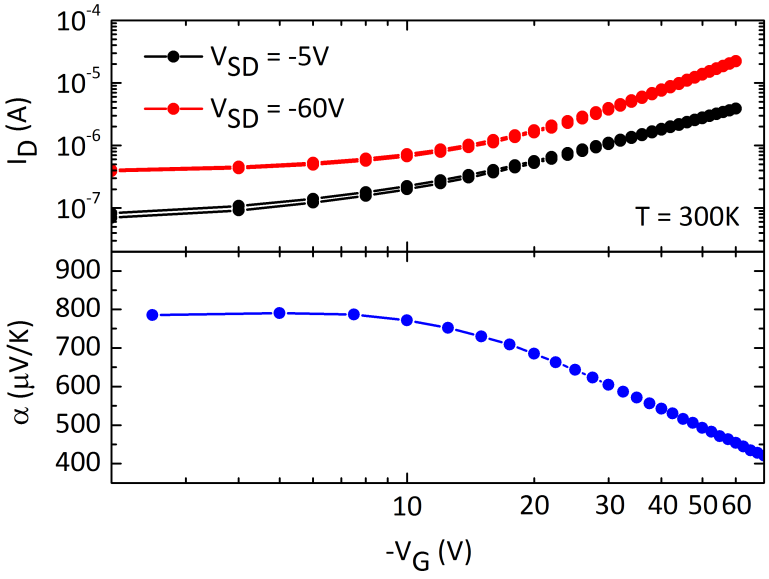

Figure 3.3: Source-drain current in the linear and saturation regime compared with the gate modulated Seebeck coefficient in a typical PBTTT device with a mobility ≈ 0.1 cm^2/Vs.

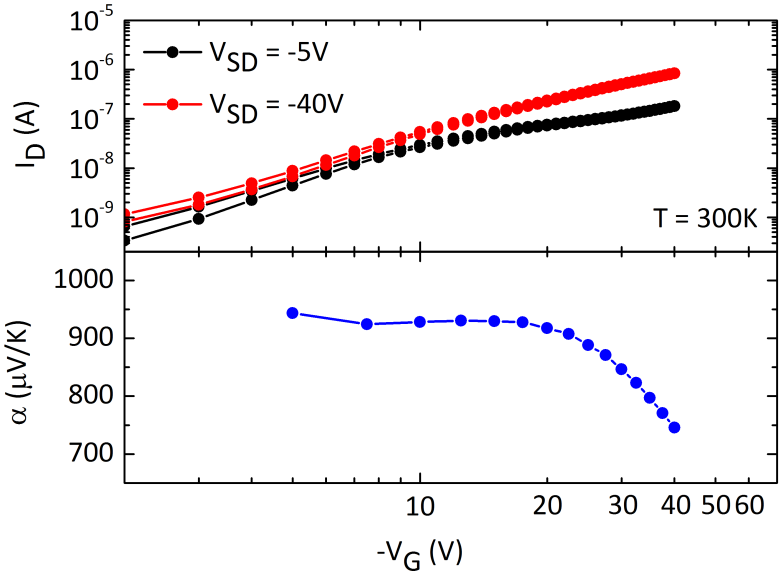

Figure 3.4: Source-drain current in the linear and saturation regime compared with the gate modulated Seebeck coefficient in a low mobility PBTTT device with a saturation mobility ≈ 0.01 cm^2/Vs. The I_D versus V_G characteristics do not show a clear V_{ON} for such low mobility devices.

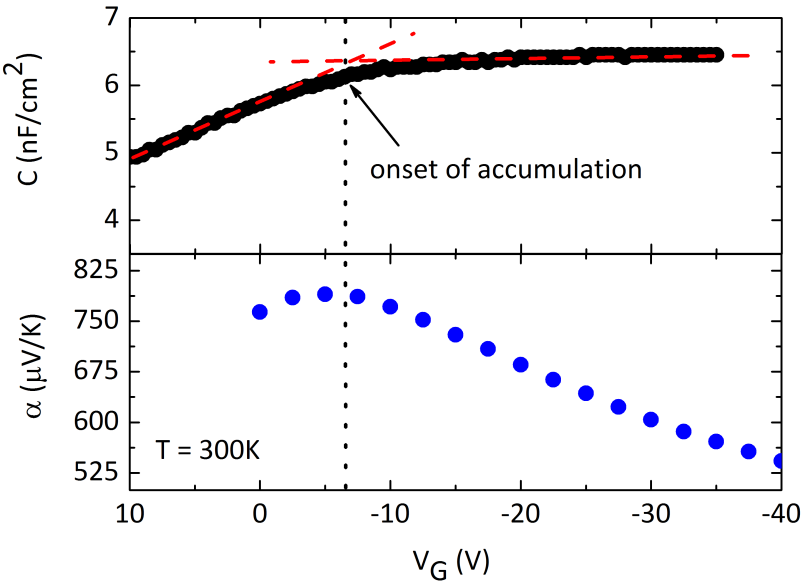

Figure 3.5: Capacitance and gate voltage modulated Seebeck measured within the same PBTTT device. The onset of accumulation from a capacitance measurement correlates well with the point where the effect of the accumulation layer dominates in the Seebeck measurement.

A comparison between the high mobility device (Fig. 3.3) and the low mobility device (Fig. 3.4) shows that the unmodulated behaviour in the Seebeck coefficient extends to higher gate voltages in the low mobility device. In this device, the contribution of the accumulation layer to the Seebeck coefficient dominates only at relatively large gate voltages leading to an extended plateau in the Seebeck coefficient. A similar lack of modulation in α with applied gate voltage was reported in pentacene FETs [70], however the transition into a regime where the effect of the accumulation layer becomes prominent was not reported. We conclude from these measurements that the gate-modulated Seebeck coefficient in an organic semiconductor allows one to identify the transition from bulk-limited conduction to accumulation layer dominated conduction.

3.3 Onset of accumulation from a measurement of capacitance

As has been explained, the onset of charge accumulation within the PBTTT FET occurs at the gate voltage where the Seebeck coefficient transitions from a plateau in Fig. 3.3 into a gradual descent. The source-drain current I_D in Fig. 3.3 represents a similar change from being voltage invariant at low gate voltages to demonstrating an increase on increasing gate voltage. Attention should be drawn to the fact that the measurements of I_D and α are not performed under equivalent conditions. When measuring I_D by doing a measurement of the transfer curve in either the linear regime or the saturation regime, a source-drain voltage V_{DS} is applied to aid the flow of current. The Seebeck coefficient is a current-devoid measurement under the absence

of such a V_{DS}. When doing a Seebeck coefficient measurement on-chip, an accumulation layer is formed on the application of a gate-voltage, while the small applied temperature differential causes a built-in voltage to be developed depending on the concentration of carriers within the accumulation layer. In essence, the conditions under which the Seebeck coefficient is measured are similar to the conditions under which the device capacitance is measured, i.e, no applied V_{DS}. Fig. 3.5 compares the device capacitance with the gate voltage modulated Seebeck coefficient of the same PBTTT device shown in Fig. 3.3. From a measurement of the device capacitance, the voltage representing the onset of accumulation is determined from the intersection of the plateau where full accumulation has taken place and the linear region characterising a build up towards full accumulation. This voltage, V_{ON}, for PBTTT is around -6 to -7 V. The dotted line in Fig. 3.5 demonstrates a good correlation between the onset of interfacial accumulation of charges seen from both measurements of device capacitance as well as from the Seebeck coefficient. The threshold voltage in the saturation regime of the same device is -9.5 V. In the forthcoming sections, when estimating the carrier concentration within the channel for different applied gate voltages for which the Seebeck coefficient is measured, we assume that the onset of accumulation is extracted from the capacitance measurement and not from the threshold voltage of the device.

3.4 Electrical characteristics of the on-chip PBTTT device

Fig. 3.6 (a) shows the FET transfer curves of a PBTTT device whose organic layer was not patterned, while the FET transfer curves shown in Fig. 3.6 (b) correspond to the same patterned device whose Seebeck coefficient was measured (Fig. 3.3). The architecture used for the unpatterned device was based on the same chip shown in Fig. 2.1 to ensure a proper comparision between patterned and unpatterned devices. Two significant advantages to device performance on patterning the organic semiconductor as seen from Fig. 3.6 are a reduced leakage current and a lowered OFF-current. Both these benefit from an elimination of spurious current paths that may otherwise increase their magnitude. A perceivable disadvantage of the patterning process is that the overall current within the device decreases by a small amount. This decrease is most probably down to the slight degredation in the device as a consequence of the relatively harsh processing steps involved in achieving a functional patterned device.

The saturation field-effect mobilities of the FET devices are computed from the derivatives of the square root of the saturation currents I_D shown in Fig. 3.6. These square roots of the saturation currents for the unpatterned and patterned devices are shown in Fig. 3.7 (a), while the mobilities extracted from them are shown in Fig. 3.7 (b). The mobility of the unpatterned PBTTT device at 300 K was around 0.1 cm^2/Vs, while that for the patterned device was 0.05 cm^2/Vs. A factor of two reduction in mobility on device patterning was a universal feature seen in all the devices investigated in this thesis. It is however safe to assume that this patterning-process-associated reduction in mobility will not substantially change the underlying charge transport mechanism within the device that is being probed using the Seebeck coefficient.

Fig. 3.8 (a) shows the square roots of current from the saturation transfer curves in the

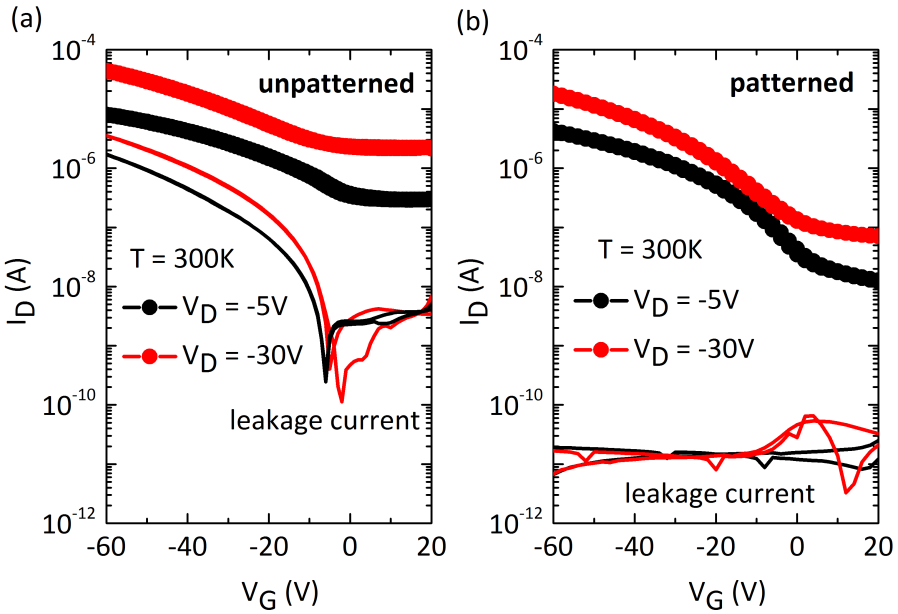

Figure 3.6: (a) Transfer characteristics of a PBTTT FET with an unpatterned organic polymer layer. (b) Transfer characteristics of a PBTTT FET with a patterned organic polymer layer.

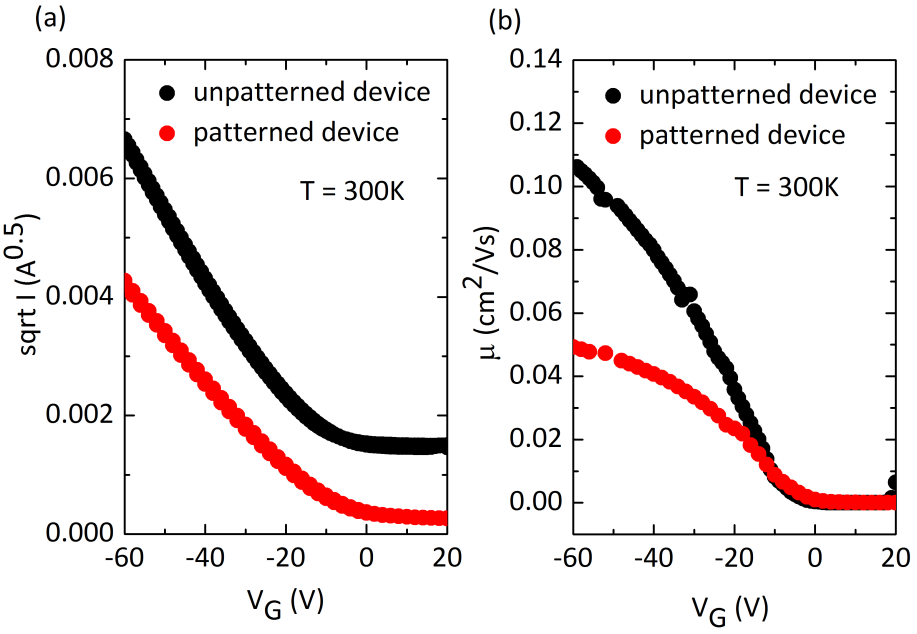

Figure 3.7: (a) Square roots of the source drain current in the saturation regime of an unpatterned and patterned PBTTT device. (b) Gate voltage dependent mobilities of the unpatterned and patterned PBTTT devices, demonstrating a factor of two reduction on patterning.

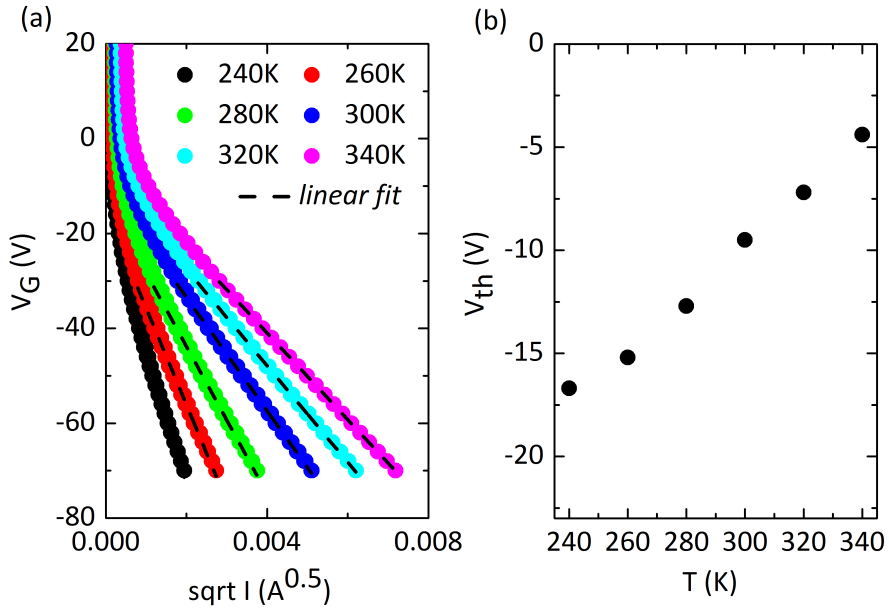

Figure 3.8: (a) Temperature dependent threshold voltages in the FET are extracted from the intercept of the high field data points along the dotted lines with the y-axis (b) The saturation threshold voltage increases within the FET on cooling down from 340 K to 240 K.

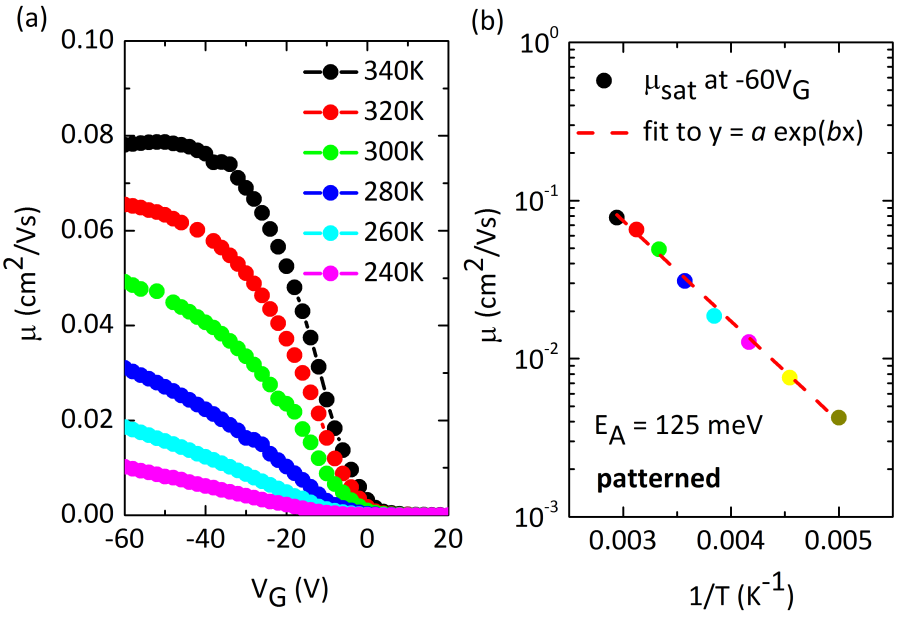

Figure 3.9: (a) Gate voltage dependent saturation mobility in the patterned PBTTT device. (b) Arrhenius behaviour in the mobility versus inverse temperature with an activation energy E_A = 125 meV in the range 340 K to 200 K.

patterned PBTTT device, plotted against the gate voltage in a way by which the saturation threshold voltages can be extracted as the y-intercept. The temperature of the device was swept from 340 K to 240 K. At every temperature, the saturation threshold voltage was extracted as the intercept of the high field region between −70 V and −30 V indicated by the dotted lines on the figure. The extracted threshold voltages are plotted in Fig. 3.8 (b). The threshold voltage increases from −5 V at 340 K to −16.5 V at 240 K. This large change in the threshold voltage on cooling the device to lower temperatures is a usual feature seen in organic FETs, the reason for which can be traced to instabilities and traps at the interface between the organic semiconductor and the dielectric layer. On cooling down the device, dipoles at the organic-dielectric interface are susceptible to being frozen, thus trapping carriers at the interface. Devices with trapped carriers then require a larger gate voltage to be applied so as to turn the device on, thus rationalising the observation of an increasing threshold voltage on reducing temperature.

The high field saturation mobility in our typical patterned PBTTT device was observed to approach 0.1 cm^2/Vs at 340 K, as shown in Fig. 3.9 (a). Shown in the same plot is also the gate voltage dependent saturation mobility at different temperatures. Over the 100 K temperature range investigated, the saturation mobility dropped from 0.08 cm^2/Vs at 340 K to 0.01 cm^2/Vs at 240 K. The reduction in mobility of carriers with temperature was Arrhenius, and the activation energy was extracted from the saturation mobility at $V_G = -60$ V using the equation $\mu = \mu_0 \exp(-E_A/k_B T)$. The activation energy of charge carriers in the patterned PBTTT device investigated here was 125 meV. The mobility prefactor μ_0 is found to be 5.9 cm^2/Vs from Fig. 3.9 (b) in the asymptotic limit $1/T \to 0$. With a phonon energy of 0.1 eV, and a presumed hopping distance $\sim$ 5 nm, the mobility prefactor for the polaron mobility from Eq. 1.5 at room temperature is 2.4 cm^2/Vs. This ballpark estimate is not far off from the experimentally determined prefactor. The magnitude of the experimentally measured mobility prefactor is hence a hint at the presence of small polaron transport in PBTTT.

3.5 Temperature dependence of the Seebeck coefficient

The variation of the Seebeck coefficient with temperature can be used as an indicator of the nature of underlying charge transport, and acts complementary to measurements of the temperature dependent conductivity. For example, the Seebeck coefficient decreases with decreasing temperature in conventional metals governed by the Mott formula [74, 64]. In the case of crystalline inorganic semiconductors where transport occurs in well defined bands, the Seebeck coefficient varies with temperature as $\alpha \propto 1/T$ [75, 64]. For disordered inorganic semiconductors such as amorphous silicon, a strong variation of the Seebeck coefficient with temperature was also observed [72, 73].

In contrast, reports of the Seebeck coefficient in organic semiconductors such as pentacene and rubrene were shown to be temperature independent [66, 70]. An explanation for this trend was however never highlighted in the published reports. The temperature dependent Seebeck coefficient in PBTTT measured for this thesis is plotted in Fig. 3.10 and is clearly

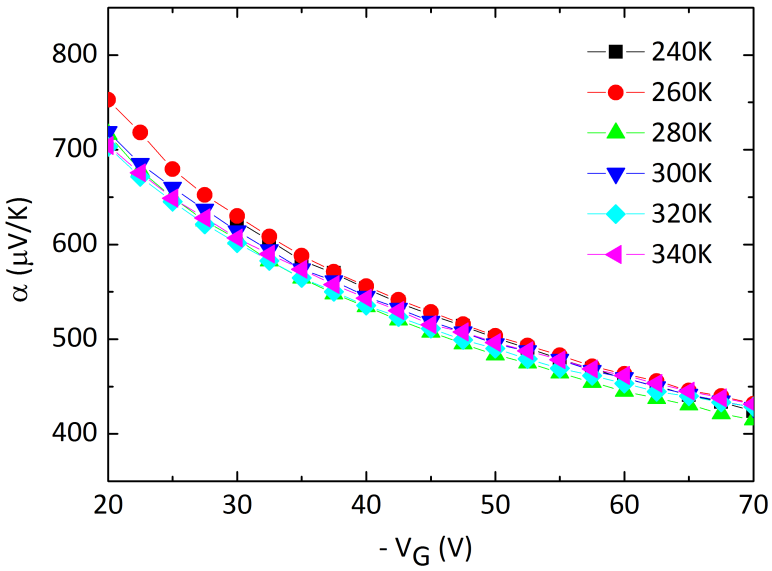

Figure 3.10: Temperature and gate-voltage modulation of the Seebeck coefficient in PBTTT. The maximum error in the measurement of the Seebeck coefficient is about ± 45 μV/K.

also temperature independent. The following sections detail the potential physics governing this temperature independent trend in the Seebeck coefficient for organic semiconductors based on two interpretations. The first interpretation invokes Variable Range Hopping within an exponential density of states while the second is based on transport within narrow bands.

3.5.1 Temperature dependence of the Seebeck coefficient interpreted using a model based on Variable Range Hopping

Fig. 3.10 plots the temperature dependence of the experimentally measured Seebeck coefficient in the high gate-voltage regime. The measurements were done in the temperature range 240 - 340 K. At temperatures lower than 240 K, the samples became increasingly resistive, causing additional offsets in the measurement of the Seebeck coefficient. Such voltage offsets occur when the resistance of the organic semiconductor approaches the input impedance of the voltmeter. As is clear from Fig. 3.10, there is no variation in the Seebeck coefficient with temperature. This lack of dependence in the Seebeck coefficient on temperature was reported in previous studies on organic semiconductors [66, 70] but was seldom a point of discussion. Here, we present a detailed analysis of the origin of this observed temperature invariance of the Seebeck coefficient in PBTTT.

The slope of the Seebeck coefficient at high gate voltages contains information on the DOS of the organic semiconductor [86]. In semiconductors such as silicon with well-defined bands where transport can unambiguously be defined though a mobility edge model, the Seebeck coefficient

for hole carriers in the valence band is given by

$$\alpha = \frac{k_\mathrm{B}}{e}\left(\frac{\mu_\mathrm{C} - E_\mathrm{V}}{k_\mathrm{B}T} + A\right), \tag{3.2}$$

where E_V is the energy of the mobility edge, μ_C the chemical potential and A is the heat-of-transport constant. To recapitulate, it is the average energy above the band edge, measured in units of $k_\mathrm{B}T$, transported by charge carriers in band states. For common values of A Eq. 3.2 generally leads to a strong temperature dependence, because E_V is expected to be temperature independent and μ_C increases only weakly with decreasing temperature due to the so-called statistical shift. Within the measured temperature range Eq. 3.2 predicts an increase in the Seebeck coefficient with decreasing temperature by about 40 % which is clearly inconsistent with the experimental observation.

Alternatively, in systems where conduction is described by a hopping mechanism, the Seebeck coefficient is expressed as

$$\alpha = \frac{k_\mathrm{B}}{e}\left(\frac{\mu_\mathrm{C} - E^*}{k_\mathrm{B}T}\right), \tag{3.3}$$

where E^* is the transport energy, the mean energy of hopping charge carriers. It is also sometimes described as the energy level at which the probability of hops is the highest. The Seebeck coefficient is positive for holes and negative for electrons. In arriving at a comparative theoretical estimate for the Seebeck coefficient using Eq. 3.3, one has to estimate the chemical potential, μ_C, and the transport energy, E^*, within an appropriately chosen DOS. As in the model of Eq. 3.2, the chemical potential, μ_C, within the channel of an organic FET can be extracted using the induced carrier concentration, n, within the accumulation layer since

$$n = \int_{-\infty}^{+\infty} g(E) f(E, \mu_\mathrm{C}) \mathrm{d}E, \tag{3.4}$$

where $g(E)$ is the DOS and $f(E, \mu_\mathrm{C})$ is the Fermi-Dirac distribution. However, in contrast to the mobility edge E_V, the transport level E^* is temperature dependent and is generally expected to move towards the chemical potential μ_C as the temperature is decreased, i.e., the hopping model tends to provide a weaker temperature dependence of the Seebeck coefficient than the mobility edge model.

To obtain an estimate of E^*, we use the concepts that disorder models for hopping are based on, i.e., that transport is assumed to be dominated by hops from the chemical potential μ_C to the transport energy level E^*, where E^* is derived using the percolation criterion

$$B_\mathrm{C} = \frac{4}{3}\pi R^{*3} \int_{\mu_\mathrm{C}}^{E^*} g\left(E\right) dE, \tag{3.5}$$

in combination with the expression for hopping conductivity based on a Miller-Abrahams-type expression for an effective jump rate across a hopping distance R^*,

$$\sigma = \sigma_0 \exp\left(-2a^{-1}R^* - \frac{E^* - \mu_\mathrm{C}}{k_\mathrm{B}T}\right). \tag{3.6}$$

Such a scheme was also used in the work by Germs and co-workers when modelling the Seebeck coefficient in pentacene [52]. $B_C = 2.8$ is the critical number of bonds for percolation and a the effective wavefunction overlap parameter. This effective hopping rate does not take into account the effects of polaronic reorganisation, which are known to be important in conjugated polymers. It nevertheless provides an effective model to investigate the influence of a temperature dependent transport energy on the Seebeck coefficient and its temperature dependence.

As a first step, an exponential density of states is defined in the form

$$g(E) = \frac{N_T}{k_B T_0} \exp\left(\frac{E}{k_B T_0}\right), \tag{3.7}$$

where N_T is the total number of localized states and T_0 is the width of the exponential DOS. The exponent in Eq. 3.6 for hopping conductivity is then optimised by substituting for R^* from Eq. 3.5 and calculating its first derivative with respect to energy, done at $E = E^*$. In other words, the equation

$$\frac{d}{dE}\left(-2a^{-1}\left(\frac{3B_C}{4\pi}\right)^{1/3}\left(\int_{\mu_C}^{E^*} g\left(E\right) dE\right)^{-1/3} - \frac{E-\mu_C}{k_B T}\right) = 0 \tag{3.8}$$

is solved so as to arrive at the master equation from which E^* can be extracted:

$$\frac{\frac{2}{3}a^{-1}\left(\frac{3B_C}{4\pi}\right)^{1/3}(N_T)^{-1/3}\exp\left(\frac{E^*}{k_B T_0}\right)}{\left[\exp\left(\frac{E^*}{k_B T_0}\right) - \exp\left(\frac{\mu_C}{k_B T_0}\right)\right]^{4/3}} = \frac{T_0}{T}. \tag{3.9}$$

A transcendental equation similar to that of Eq. 3.9 can be derived for a Gaussian DOS [87]. The parameters T_0, a, σ_0 and d_{sc} used to estimate E^* are got by using the previously described 2D transport model recently published by A. J. Kronemeijer [54], the crux of which was reproduced in Eq. 1.24. A fit to the transfer curves in the saturation regime of PBTTT using Eq. 1.24 is shown in Fig. 3.11. The parameters used to arrive at this fit are summarised in Table 1.

Table 1: Parameters used in the 2D disorder model simulations

σ_0	2.4×10^8 S/m
N_T	10^{26} m^{-3}
T_0	750 K
a	3.2 Å
d_{sc}	2 nm

To simulate the high OFF currents normally seen in PBTTT, an offset needed to be added to the simulated currents at low gate voltage. Using the parameters of Table 1 in Eq. 3.9, E^* can be extracted and a theoretical estimate for the Seebeck coefficient arrived at. Such a theoretical estimate for the Seebeck is plotted in Fig. 3.12 for $T_0 = 750$ K. The theoretical model reproduces very well the slope of the gate voltage dependence of the Seebeck coefficient, which depends

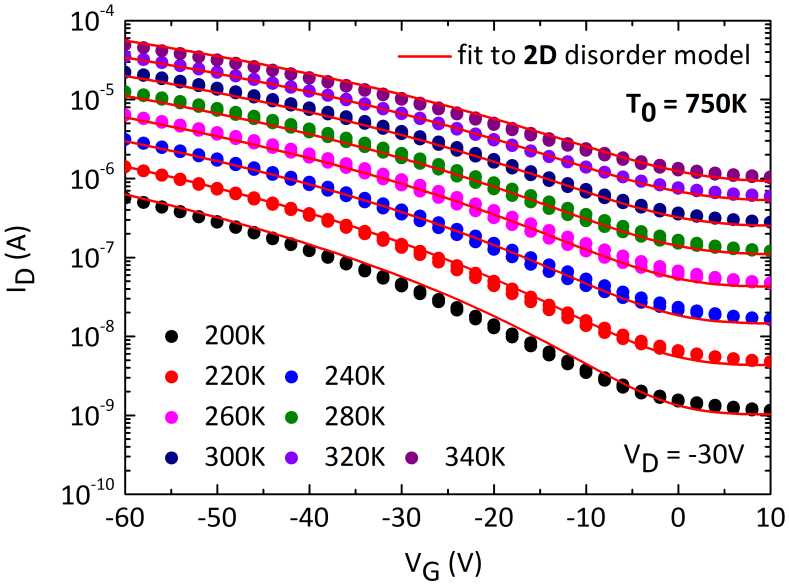

Figure 3.11: Fit of the transfer curves in the saturation regime to a 2D disorder model with $T_0 = 750$ K.

sensitively on the value of T_0. The theory however overestimates the absolute magnitude of the Seebeck coefficient as compared with the measurement. This discrepancy has been noted previously and its origin is currently not well understood. One possible reason is that the theoretical model only accounts for transport at E^* while in a real semiconductor energy levels below E^* also contribute to hopping transport. Taking this into account is expected to reduce the overall magnitude of the Seebeck coefficient. Another factor that will have to be taken into account in a refined model is the electron-phonon coupling and polaronic reorganisation which is known to be important [41], but has been neglected in the present analysis. The effect of the polaronic reorganisation will be to modify the hopping rate from the effective jump rate used above and might also lead to a better agreement with the data. Taking both effects into account will require a more sophisticated model.

The temperature dependent trends expected in the Seebeck coefficient for hopping transport and transport beyond a mobility edge are distinctly different. In the hopping case, the Seebeck is temperature independent while in the case of a mobility edge, the Seebeck is expected to show a considerable variation with temperature. The hopping model predicts only a weak temperature dependence in the Seebeck because E^* decreases with decreasing temperature. Within the above chosen hopping framework, such a weak temperature dependence seen both in experiment and in theory is evidence that our PBTTT FETs can be appropriately described using a hopping transport model, and cannot be described by a mobility edge model. It is notoriously difficult to distinguish between hopping and mobility edge models of transport based on measurements of the temperature dependence of the FET mobility alone. This study hence shows that by combining temperature dependent Seebeck coefficient measurements with mobility

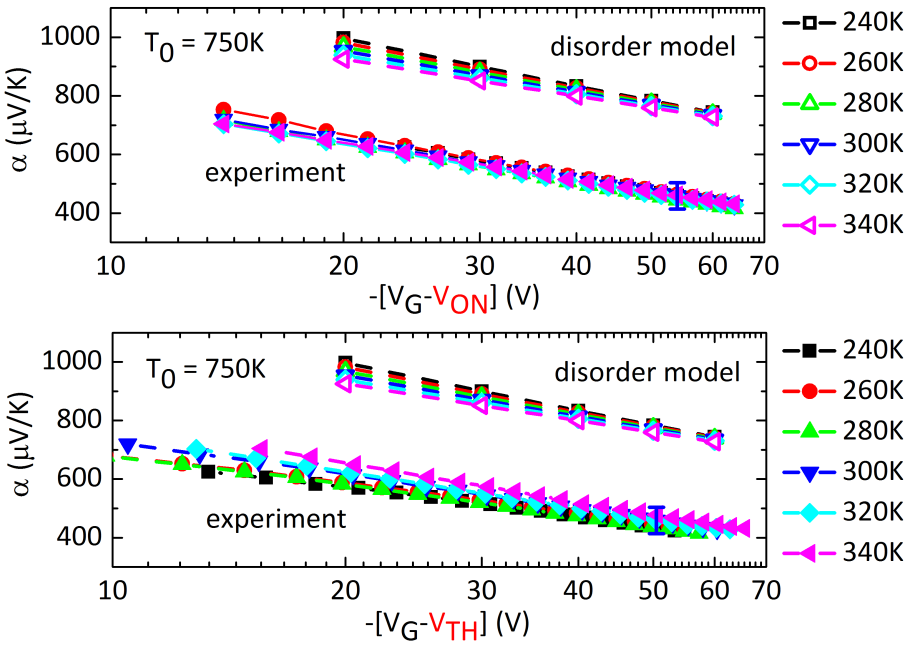

Figure 3.12: Temperature and gate-voltage modulation of the Seebeck coefficient in PBTTT. Top Panel: experimental curves have been shifted by V_{ON}, the onset voltage of accumulation from capacitance measurements. Bottom Panel: experimental curves have been shifted by V_{TH}, the threshold voltages of the saturation transfer curves. An error bar of the maximum error is shown at $V_{\mathrm{G}} = -60$ V for $T = 300$ K. Error bars for other gate voltages and temperatures are comparable and are not shown for clarity.

measurements, such a distinction is possible.

Seebeck as a handle to confirm a measurement of the width of the DOS

When the 2D disorder model is used to fit the temperature dependent transfer curves and extract the width of the density of states T_0, the number of free parameters, σ_0, a, T_0 and d_{sc} in addition to a threshold voltage shift that can be varied to get a satisfactory fit are far too many. In Fig. 3.13, a fit to the temperature dependent transfer curves of PBTTT has been done with another set of fitting parameters summarised in Table 2 below:

Table 2: Parameters used in the 2D disorder model simulations

σ_0	7.5×10^7 S/m
N_{T}	10^{26} m^{-3}
T_0	450 K
a	2.0 Å
d_{sc}	2 nm

Despite using a fairly narrow $T_0 = 450$ K, the fit although not perfect at low temperatures is acceptable for all temperatures in the range 340 K - 240 K. When such an ambiguity arises, a

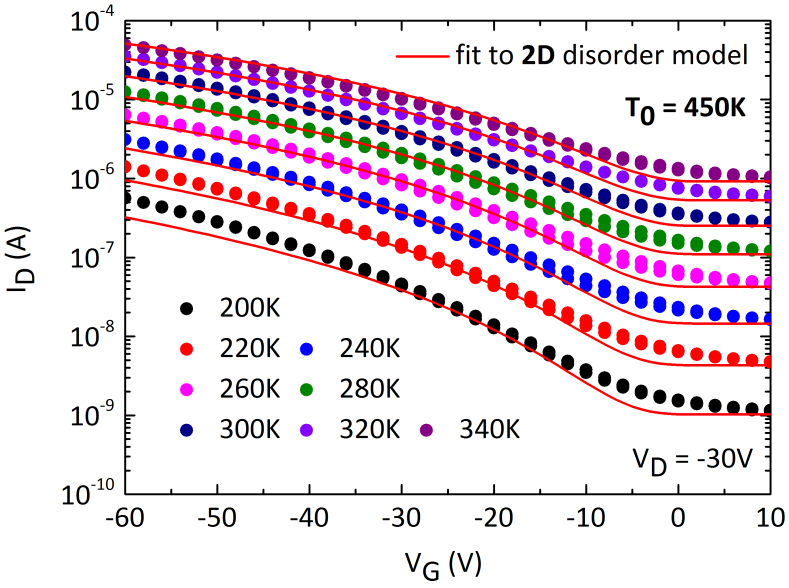

Figure 3.13: Fit of the transfer curves in the saturation regime to a 2D disorder model with $T_0 = 450$ K.

measurement of the Seebeck coefficient can act as a second handle to judge the correctness of the chosen T_0 value. Fig. 3.14 is a comparison between the experimental Seebeck and a calculation of the same with the fit parameters quoted in the Table 2.

It is evident from Fig. 3.14 that the slope of the calculated Seebeck coefficient is shallower than that of the measurement. The change in the Seebeck coefficient from $-[V_G - V_{ON}] = 20$ V to $-[V_G - V_{ON}] = 60$ V is 250 μV/K from of the measurement, while it is only 150 μV/K from the calculation. The agreement between the relative change in the Seebeck coefficient between the experiment and the simulation is superior when $T_0 = 750$ K is chosen (Fig. 3.12). Working strictly within the confines of the 2D Hopping framework, such Seebeck coefficient measurements can be considered to be a complementary probe to confirm the measure of T_0. A good fit to both the saturation transfer curves as well as an agreeable slope in the Seebeck coefficient with gate voltage are simultaneously necessary to provide a robust quantification for the disorder parameter T_0. This said, when considering the predictions of a 3D Hopping framework in addition, contradictory estimates in the prediction of T_0 arise.

Disagreement between 2D and 3D models for transport in their prediction of T_0

The magnitude of T_0 used to characterise the width of the exponential DOS in an organic FET depends on whether the model employs a 2D or a 3D description of carrier density in the channel. Fig 3.15 shows the result of using a 3D model with a source-drain current given by Eq. 1.23. Such a model yields a good fit with $T_0 = 400$ K. The additional parameters used to arrive at this fit are summarised in Table 3.

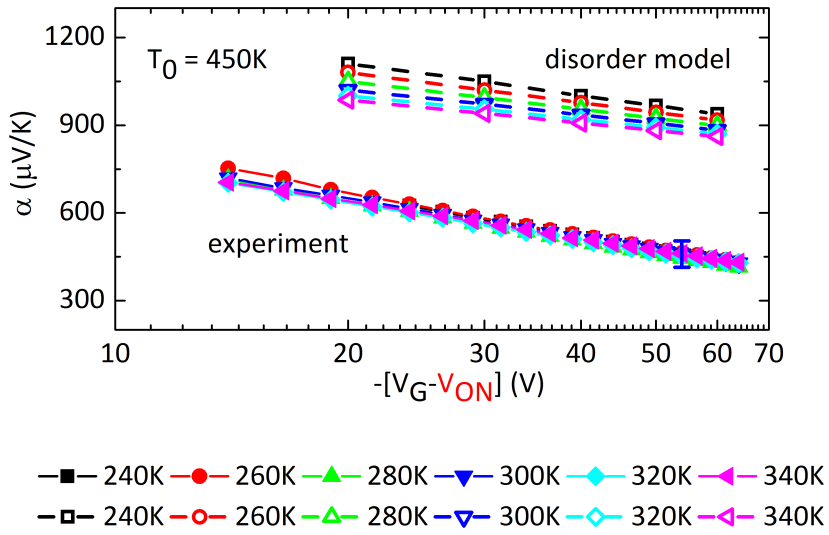

Figure 3.14: Comparision of the experimentally measured Seebeck coefficient with theory for T_0 = 450 K using the 2D model.

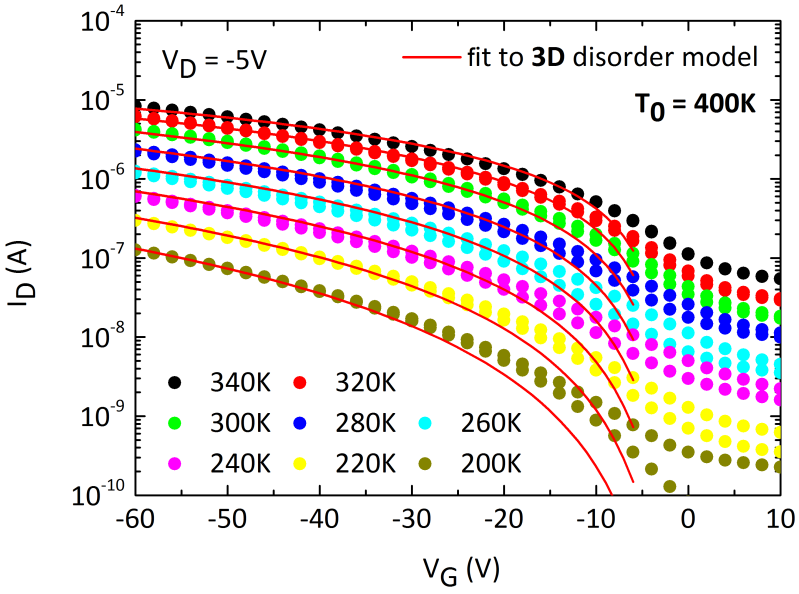

Figure 3.15: Fit of the transfer curves in the linear regime to a 3D disorder model with T_0 = 400 K

Table 3: Parameters used in the 3D disorder model simulations

σ_0	8.5×10^7 S/m
N_T	10^{26} m^{-3}
T_0	400 K
a	1.6 Å

A 3D model predicts values of T_0 that are generally lower than those predicted by a 2D model. This issue was discussed in Chap. 1, highlighting examples from existing literature. It is hence necessary to use these disorder models with extreme care, being aware of the fact that the many fitting parameters render the magnitude of T_0 approximate.

All told, the contradiction in the estimates of disorder T_0 that arise when using 2D and 3D disorder hopping models, added to the fact that these models require many fitting parameters, leave them rather unattractive. It is hence necessary to use an interpretation that overcomes the drawbacks of such disorder models, but still quantifies the role of disorder within the organic semiconductor. One such interpretation, based on the existence of narrow bands, is presented in the next section.

3.5.2 Temperature dependence of the Seebeck coefficient interpreted using a narrow band (polaron) model

The narrow band interpretation does away with all the ambiguous fitting parameters that disadvantage the disorder models. The main assumption made is that disorder is quantified by carrier trapping that occurs within shallow trap states located at energies a few $k_\mathrm{B}T$ from the transport level. This model is referred to here as a narrow band polaron model owing to evidence that transport in organic polymers is mediated by polarons [88] and that polaron bands generally tend to be narrow, i.e., with an energetic spread $\sim k_\mathrm{B}T$.

When n carriers are distributed within N thermally available states all of which are located within a narrow energy band of width $\sim k_\mathrm{B}T$, the Seebeck coefficient including Fermionic spin degeneracy is given by its narrow band approximation discussed in Chap 1,

$$\alpha = \frac{k_\mathrm{B}}{e} \ln\left(2 * \frac{1-c}{c}\right), \tag{3.10}$$

where $c = n/N$ is the fractional occupancy of charge carriers. Assuming that there is one thermally available state per monomer unit, the total number of thermally available states in PBTTT is 8.86×10^{20} cm^{-3}. This is computed using the three dimensions of a monomer unit which are (i) $\pi - \pi$ stacking distance of 0.38 nm, (ii) backbone repeat unit of 1.35 nm and (iii) alkyl-side-chain length of 2.2 nm [82]. The carrier concentration n in the channel of the device was estimated using the capacitance of the 300 nm PMMA dielectric used. The specific case of FETs lays down the condition, $n \ll N$, and the Seebeck takes the form,

$$\alpha = \frac{k_\mathrm{B}}{e} \ln\left(2 * \frac{N}{n}\right). \tag{3.11}$$

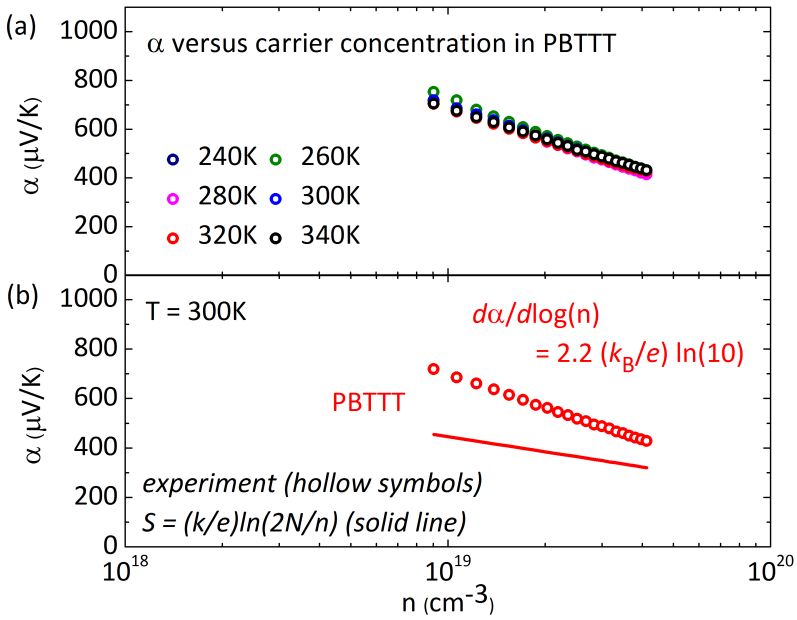

Figure 3.16: (a) Seebeck coefficient versus temperature plotted as a function of carrier concentration in the accumulation layer. (b) Comparison between the measured carrier-concentration-modulated Seebeck coefficient at 300 K and the expectation from a narrow band polaron model.

Fig. 3.16 (a) shows the temperature dependence of the Seebeck plotted as a function of carrier concentration. The data is the same as that plotted in Fig. 3.10, except that the gate voltage has been converted into a carrier density in the channel and a linear-log scale has been used. Fig. 3.16 (b) compares the measured carrier concentration modulated Seebeck coefficient at 300 K (symbols) with the prediction of the narrow band polaron model (straight line).

As explained in Chap. 1, the narrow band polaron model is an ideal estimate of the Seebeck coefficient where all the n carriers contribute to the transport of entropy. If on the other hand, a fraction of the gate-induced charge carriers, n_{trap}, are trapped in states within the narrow band and do not contribute to energy and entropy transport, the narrow band Seebeck formula Eq. 3.11 will need to be modified to include its existence and has the form,

$$\alpha = \frac{k_{\mathrm{B}}}{e}\ln\left(2 * \frac{N}{n - n_{\mathrm{trap}}}\right). \tag{3.12}$$

Eq. 3.12 is used to explain the carrier-concentration modulated Seebeck. From Eq. 3.12, the slope of the curve $\alpha - \log(n)$ deviates from the ideal value $-(k_{\mathrm{B}}/e)\ln(10) \approx -200\ \mu\mathrm{V/K/decade}$ that applies in the absence of traps. The slope of $\alpha - \log(n)$ when shallow traps are included is given by,

$$\frac{\partial\alpha}{\partial\log(n)} = -\frac{k_{\mathrm{B}}}{e}\ln(10)\left(\frac{n}{n - n_{\mathrm{trap}}}\right) = -\frac{k_{\mathrm{B}}}{e}\ln(10) \times f. \tag{3.13}$$

f is an 'enhancement factor' that increases the slope of the measured $\alpha - \log(n)$ so as to include the effect of the shallow trap states. In the case of PBTTT, $f = 2.2$. The enhancement factor f

can then be used to estimate the ratio of shallow trapped states to the total number of induced charge carriers n_{trap}/n, a ratio of which is found to be ≈ 0.5. What this implies is that trapping of charge carriers is dominant within PBTTT and only about 50 % of the charge carriers induced in the channel of the device contribute to energy transport. The situation of course is not so pessimistic when the device is operated as an FET, since the accumulated charge carriers are subject to an additional source-drain electric field (V_{DS}) whose presence may help de-trap charges from shallow traps, thus increasing the number of charge carriers that contribute to current.

The narrow band picture used here is not compatible with the disorder model that is routinely used to explain charge transport in organic semiconductors. It nevertheless provides an alternative explanation of the observations. The narrow band picture does not assume the existence of any particular shape of the density of trap states, be it exponential or Gaussian. The assumption made is that once full accumulation is reached, i.e, beyond V_{ON} in the C-V curve of Fig. 3.5, all the N available states become thermally accessible. Below the onset of accumulation V_{ON}, the deep trap states that may exist at energies far below the polaronic narrow band get filled. The narrow band model was invoked here only to explain transport beyond V_{ON}. Thus the subthreshold regime where the shape of the density of states invoked in the disorder model may have played an important role in charge transport is not considered. In addtion, in PBTTT, the effect of the sub-threshold regime is swamped by the presence of high transistor OFF-currents due to unintentional dopants. This makes it difficult to ascertain the real role sub-threshold energetic disorder will have on the Seebeck coefficient, where there is a definite certainty that the charge transport states live at energies $> k_{\mathrm{B}}T$ thus rendering a narrow band model inapplicable. It has proven difficult to measure the Seebeck coefficient in the sub-threshold regime for the polymers investigated in this thesis as will be shown in the forthcoming Chapters. This is because, the device resistance in the sub-threshold regime is normally high, thus contributing to large offsets in the thermal voltage measurement rendering any estimate of the Seebeck coefficient unreliable.

All told, despite the simplicity of the narrow band interpretation as described by Eq. 3.13, it predicts the three main observations of the gate modulated Seebeck coefficient measurements. It predicts (a) a temperature invariance, (b) large Seebeck coefficients and (c) a modulation of the Seebeck coefficient with increasing charge carrier concentration. Its elegance overrides that of the previously described disorder models and will hence be the chosen model when interpreting Seebeck measurements in the forthcoming Chapters.

3.6 Summary

The on-chip microfabricated device designed to measure the Seebeck coefficient in solution processed organic semiconductors was used to investigate the semiconducting polymer PBTTT. Gate voltage modulated Seebeck measurements in PBTTT show a transition from bulk limited transport to accumulation layer dominated transport. The onset of accumulation corresponds

to the onset of accumulation from device capacitance measurements. A strong temperature dependence of the Seebeck coefficient is absent. Such a trend is a feature predicted using both a disorder hopping model as well as a polaronic narrow band model. Disorder hopping models however estimate the magnitude of the Seebeck coefficient to be several hundred μV/K above the experimentally determined value. The fact that there are many fitting parameters in these disorder models also make them less attractive. Polaron formation in organic semiconductors is well established, and hence using a Seebeck coefficient that describes narrow polaron bands appears to be reasonable. The magnitude of the slope of the Seebeck coefficient versus carrier concentration is an indicator of the extent to which trapping is important in the device. In the case of PBTTT, the measurements establish that upto 50 % of the charge carriers are trapped and do not contribute to energy transport in the accumulation regime. This situation is improved within an FET where a lateral source-drain field coexists. Such a field may help de-trap charge carriers in shallow traps and enhance the total number of carriers that contribute to charge transport.

Chapter 4

Seebeck coefficient in IDTBT

4.1 Introduction to IDTBT

The device performance of conjugated polymer semiconductors has improved greatly over the last 25 years through exploration of a wide range of molecular structures and detailed understanding of the relationship between structure and physical properties [18]. However, several fundamental limitations of these low-temperature, solution-processable and mechanically flexible materials have not been overcome. Most importantly, their transport properties including charge carrier mobilities and exciton diffusion lengths remain limited by pronounced energetic disorder associated with spatial variations of the backbone conformation and intermolecular packing of the polymer chains that occur inevitably in thin polymer films. Disorder-dominated charge transport was first established in low-mobility, amorphous polymers used in xerographic applications whose density of states can be described by a disorder-broadened Gaussian with a width larger than $k_{\mathrm{B}}T$ at room temperature [28]. Higher charge carrier mobilities were achieved in semicrystalline polymers, such as poly-3-hexylthiophene (P3HT) [90] and poly(2,5-bis(3-alkylthiophen-2-yl)thieno(3,2-b)thiophene) (PBTTT) [91]. Their highly ordered, pi-stacked, lamella, with edge-on polymer backbone orientation achieved through self-organisation has

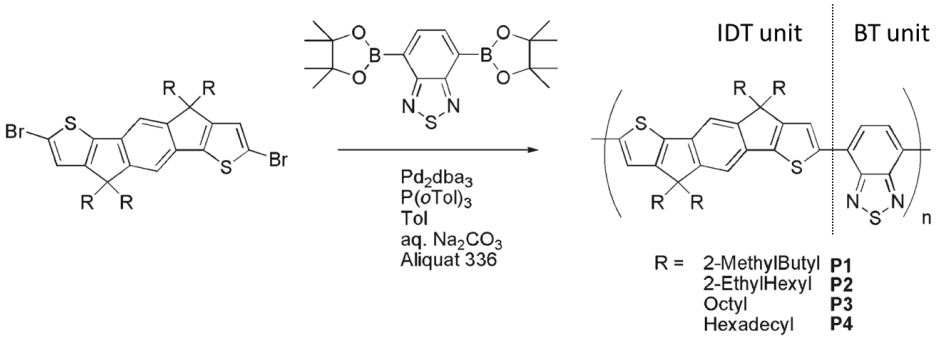

Figure 4.1: Synthesis route for IDTBT polymers by Suzuki polycondensation. Shown using a dotted demarcation are the two units that compose IDTBT, the IDT unit and the BT unit. In this work, C_{16}-IDTBT (R = Hexadecyl) was investigated. Image adapted from [89].

until recently been the main structural leitmotif for achieving high charge carrier mobilities in conjugated polymers. However, even in these highly crystalline polymers, disorder associated with amorphous grain boundary regions and conformational defects within the crystalline domains causes a tail of localized states that limits the charge carrier mobility in field-effect transistors to still relatively low values (< 1 cm^2/Vs) [92].

Much excitement has been caused by the recent discovery of surprisingly high charge carrier mobilities in the range of 1-10 cm^2/Vs for a number of donor-acceptor co-polymers [93, 94, 95]. These polymers have comparatively complex backbone structures comprising an alternating sequence of electron-rich donor and electron-deficient acceptor units, in some cases derived from natural or synthetic dyes/pigments, such as diketopyrrolopyrrole (DPP) or isoindigo (IID) [95, 96, 97, 98]. These polymers have been shown to be semicrystalline as well, but their crystalline domains are not as large and well oriented as in P3HT/PBTTT [92]. In some of these systems the high mobility may be related to a network of long polymer tie chains within a relatively disordered microstructure that provide interconnecting charge transport pathways between crystalline domains and/or the large size of the conjugated units that facilitate intermolecular electron transfer. However, the degree of energetic disorder in these polymers has been found to be higher than in highly crystalline polymers such as P3HT and PBTTT [92]. To date no polymer semiconductor has been discovered in which the energetic disorder is sufficiently small that all molecular sites are thermally accessible at room temperature.

A seldom used, but powerful probe to study the influence of disorder on the transport properties is the Seebeck coefficient and its dependence on the charge carrier concentration. In hopping systems the major contribution to α is the entropy of formation S_f which is defined as the change in the entropy of the system upon addition of a charge carrier [59]. It is independent of the transport mechanism and can be written as $S_\mathrm{f} = S_\mathrm{mixing} + S_\mathrm{vib}$. The entropy of mixing, S_mixing, accounts for the distribution of carriers within the thermally available electronic states. The vibronic contribution, S_vib, may need to be considered, particularly in systems with strong electron-phonon interactions, in which the vibrational modes soften upon addition of a carrier [59]. In non-degenerate semiconductors, S_mixing is usually the dominant contribution because the change in the entropy of mixing upon adding a carrier to a system is large, owing to there being very few carriers per thermally available state. Seebeck measurements as a function of temperature and carrier concentration provide a more direct and unambiguous measure of the density of thermally accessible transport sites and the degree of energetic disorder than measurements of conductivity [86, 99].

In this Chapter, we investigate the transport physics and the role of energetic disorder in one of the new high mobility donor-acceptor co-polymers, indacenodithiophene-co-benzothiadiazole (IDTBT). IDTBT has previously been shown to exhibit high field-effect mobilities of > 1 cm^2/Vs despite a lack of long range crystalline order [93, 94, 89]. As reported by Zhang *et al.*, the high performance observed in IDTBT is thought to originate not from crystallinity but instead, from an extended backbone co-planarity that allows fast in-plane charge transport along the polymer

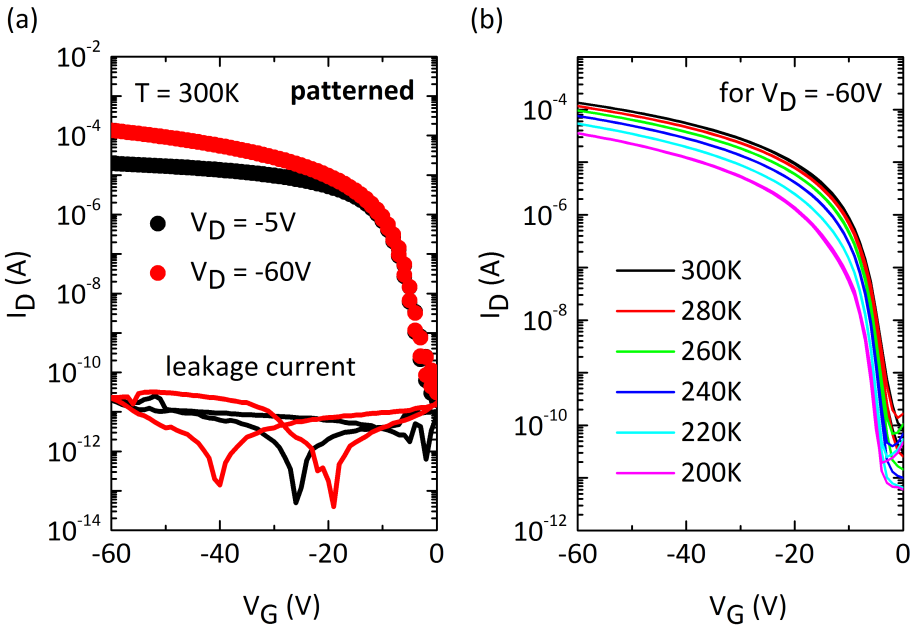

Figure 4.2: (a) Linear and saturation transfer curves of a patterned IDTBT device at 300 K (b) Temperature dependence of the saturation transfer curves between 300 K and 200 K.

backbone with only occasional interchain hopping in regions of close $\pi - \pi$ stacking and from a well-defined molecular orientation across the entire film, i.e., not just in the semicrystalline domains [93]. By combining FET and field-effect modulated Seebeck measurements with optical absorption spectroscopy we demonstrate that IDTBT exhibits an exceptionally low degree of energetic disorder compared to other conjugated polymers and is the first solution-processed conjugated polymer that approaches disorder-free transport near room temperature.

4.2 Electrical characteristics of the on-chip IDTBT device

A careful optimisation of the thin film processing performance of top-gate, bottom-contact IDTBT FETs with Cytop gate dielectric (Asahi Glass) was carried out to achieve devices with textbook-like transfer (Fig. 4.2 (a) and (b)) and output (Fig. 4.3) characteristics displaying a very low parasitic contact resistance. Optimized devices made from IDTBT films annealed at a low temperature of 100 °C exhibited high uniformity, a low saturation threshold voltage at 300 K of $V_{th} \approx -3$ to -5 V and a high saturation mobility in the range of 1.7 - 2.2 cm^2/Vs (for unpatterned devices) extracted from a linear fit of the gate voltage dependence of the square root of the drain current. In addition, the linear mobility was found to be close to the saturation mobility. Somewhat higher mobilities (upto 3 - 4 cm^2/Vs) could be extracted from films annealed at higher temperatures similar to values reported elsewhere [93], but this involved the loss of the textbook-like characteristics, the appearance of contact resistance effects at small drain voltages, high threshold voltages, and may well be an artefact of the mobility extraction procedure [100]. Here, we focus on devices with ideal characteristics processed at low temperatures.

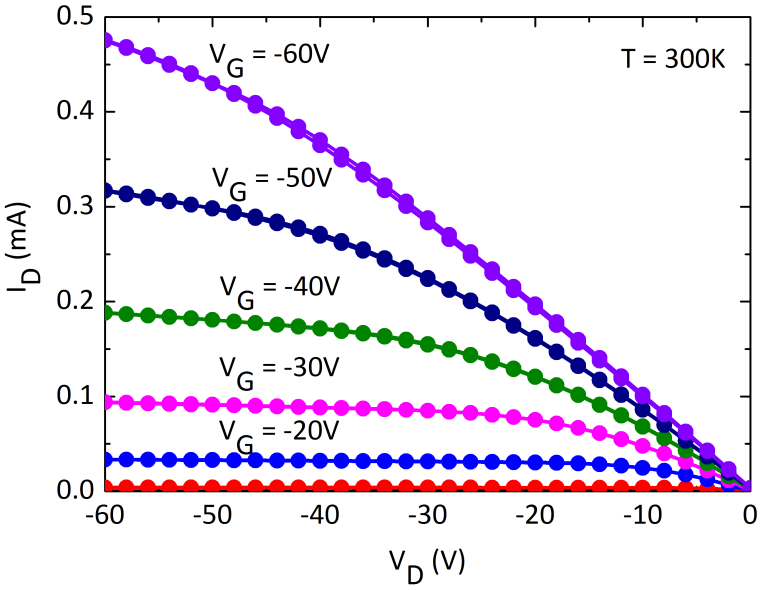

Figure 4.3: Output curves of a typical IDTBT device at 300 K.

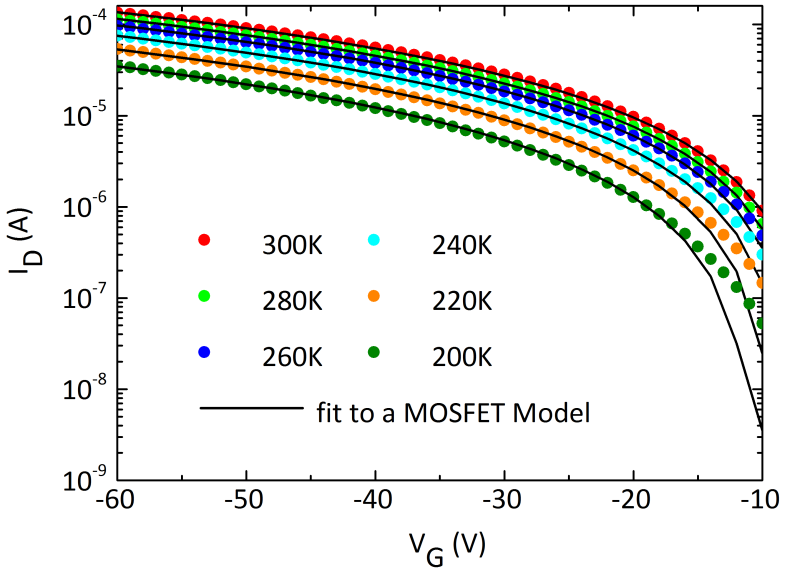

Figure 4.4: A fit of the temperature dependent transfer characteristics in the saturation regime to a simple MOSFET model of Eq. 4.1.

The temperature dependence of the transfer characteristics of the FET in the saturation regime ($V_D = -60$ V) are shown in Fig. 4.2 (b). We investigated the temperature dependence of the FET transfer characteristics in this regime by analysing the power law dependence of $I_D \propto (V_G - V_{th})^\gamma$. A good fit, shown in Fig. 4.4, can be made to the temperature dependent transfer curves of Fig. 4.2 (b) using a common MOSFET-type equation for the drain current,

$$I_D = \frac{\mu_{sat} C_{ox} W}{2L}(V_G - V_{th})^2, \tag{4.1}$$

where all parameters in Eq. 4.1 retain their usual meanings. It is striking to observe that IDTBT exhibits a textbook-like square dependence ($\gamma = 2$, where γ is the exponent of $(V_G - V_{th})$ in Eq. 4.1) of drain current on gate voltage, a feature which to our knowledge has not been reported in a polymer until now. $\gamma = (T_0/T) + 1$ is typically observed in polymer FETs interpreted using a disorder model of transport where the parameter T_0 is a measure of the exponential width of the DOS of the polymer [54, 53]. A temperature evolution of IDTBT transfer characteristics across the entire temperature range can be simulated using this disorder-free MOSFET-like model, Fig. 4.4, that assumes a simple square gate voltage dependence with a thermally activated mobility.

The temperature dependent thermally activated mobilities are extracted from a plot of the square root of the saturation drain current versus gate voltage, shown in Fig. 4.5 (a). From this plot, it is clear that the curves remain linear for a considerable range of gate voltages at all investigated temperatures. The threshold voltages extracted from Fig. 4.5 (a) are shown in Fig. 4.5 (b), and vary from -5 V at 300 K to -12 V at 200 K. A plot of the temperature activated mobility, Fig. 4.6 (a), is a direct measure of the linearity of the high field region in Fig. 4.5 (a) since the mobility is estimated from the derivative of the square root of the saturation drain current. In IDTBT devices the FET mobility reaches a gate-voltage invariant plateau for $|V_G| > 20$ V at 300 K and for temperatures down to 200 K. In contrast, the mobility of PBTTT is strongly gate voltage dependent at 300 K and for lower temperatures as previously shown in Fig. 3.9. Within the framework of a disorder model, such a gate voltage dependent mobility is a characteristic associated with the filling up of a strongly disorder broadened DOS. The FET characterisation of IDTBT hence provides clear evidence for the energetic disorder in IDTBT being significantly lower than in PBTTT. The activation energy estimated from the mobility, Fig. 4.6 (b), is only 53 meV, much smaller than that measured previously for PBTTT.

4.3 Seebeck coefficient in IDTBT

To perform accurate measurements of the Seebeck coefficient as a function of gate voltage and temperature we used a similar microfabricated device architecture with integrated heater and temperature sensors used for both PBTTT and the ambipolar polymer PSeDPPBT in this thesis. Although Chap. 5 is exclusively dedicated to measurements on the ambipolar polymer PSeDPPBT, a few results from there are included in this Chapter so as to draw a comparison

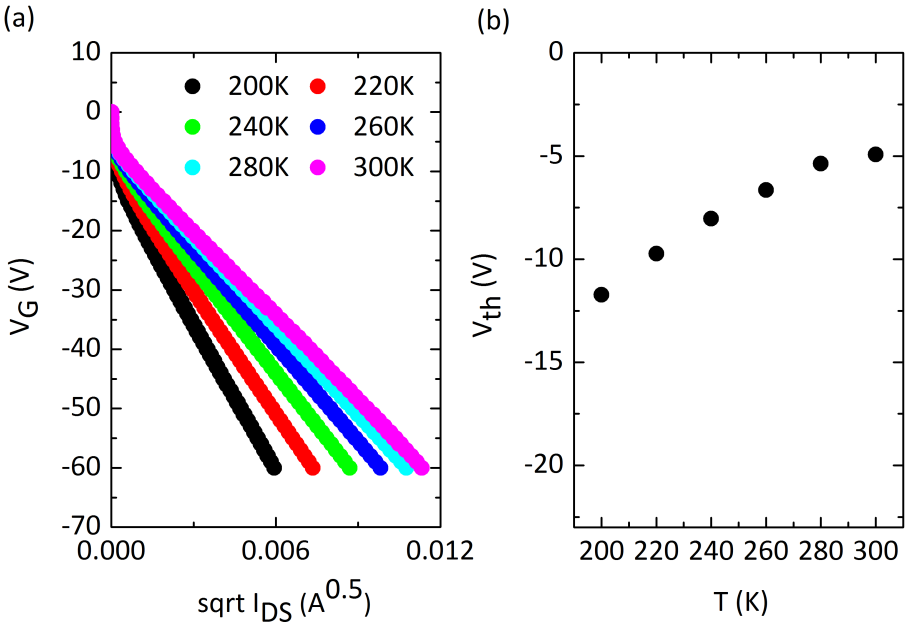

Figure 4.5: (a) A plot of the square root of the drain current in the saturation regime versus the applied gate voltage (b) the threshold voltages at different temperatures were extracted as the y-intercept of Fig. 4.5 (a).

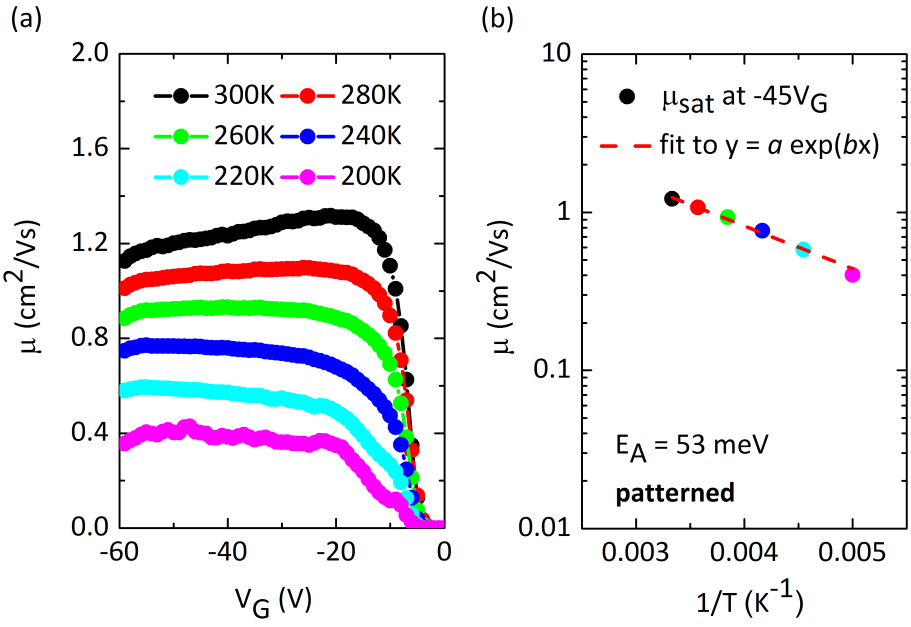

Figure 4.6: (a) Gate voltage invariant plateaus of the mobility in the temperature range 300 K to 200 K (b) Activation energy of the mobility in IDTBT.

with IDTBT. In the case of PBTTT and PSeDPPBT, the heater and temperature sensors were defined by thin, resistive wires of a Pt/Au bilayer (17 nm/3 nm). In the case of the IDTBT devices however, a Ti/Au bilayer (3 nm/12 nm) was used since electrical injection from pure Au into IDTBT proved far superior, from a standpoint of both mobility and threshold voltage, than using a Pt/Au bilayer. Once again, the two thermometer wires, which allowed two and four-point measurements of their resistivity, were also used as voltage probes in the Seebeck measurements and as source-drain electrodes for normal FET measurements. The chip layout was the same as shown in Fig. 2.1, except that the IDTBT film was patterned to a width W = 1 mm (in the PBTTT device W = 1.5 mm). Here too, the semiconductor was patterned using the patterning process [101] in order to isolate the heater from the semiconductor and avoid electrical crosstalk with the thermal voltage probes during a Seebeck measurement. Patterning the organic semiconductor also reduces the gate leakage current, a prerequisite for measuring the thermal voltage with high accuracy. The patterned organic semiconductor was top-gated using a spin-coated polymer dielectric and an evaporated aluminium gate. 500 nm Cytop was used as the dielectric layer for IDTBT. As a reminder, it should be mentioned that 300 nm PMMA was used for the PBTTT and the ambipolar polymer PSeDPPBT devices. The on-chip integrated architecture allowed us to perform more accurate measurements of the gate voltage and temperature dependence of the Seebeck coefficient across common FET channel lengths between 20 - 50 μm than would have been possible with conventional, mechanically glued thermocouples and macroscopic heaters.

Fig. 4.7 shows a gate-modulated thermal voltage measurement on the IDTBT device at 300 K. As routinely done, for each gate voltage the on-chip heater power is modulated parabolically (top panel) and the gate voltage is progressively stepped up from -30 V to -70 V (middle panel). The thermal voltage is measured simultaneously during the sequence of heater power and gate voltage sweeps. The thermal voltage follows the trace in heater power as expected, but has a reduced magnitude at high gate voltages, i.e., under increasing channel accumulation. The error in the thermal voltage measurement is ± 1 μV, representing less than 0.1 % of the maximum measured thermal voltage. The temperature differentials on-chip for the parabolic heater power trace in Fig. 4.7 were determined by measuring the resistances of the electrodes on the hot and cold ends of the patterned organic layer and converting these into a temperature after calibrating the temperature coefficient of the resistance of the electrodes. Finally, the Seebeck coefficient is extracted from the linear slope of ΔV versus ΔT at different gate voltages. Specific plots of ΔV versus ΔT will not be shown here since the outcomes are similar to those shown previously for PBTTT. The plots were however included in the supplementary information of a letter on this work that has recently been submitted for review to the journal *Nature*.

Capacitance measurements were performed on the Cytop-gated IDTBT device and is shown in the top panel of Fig. 4.8. From C-V measurements, the onset of accumulation was estimated to be at ≈ -13 V. Seebeck coefficient measurements in IDTBT were measured only in full accumulation, shown in the bottom panel of Fig. 4.8. The onset of accumulation estimated here

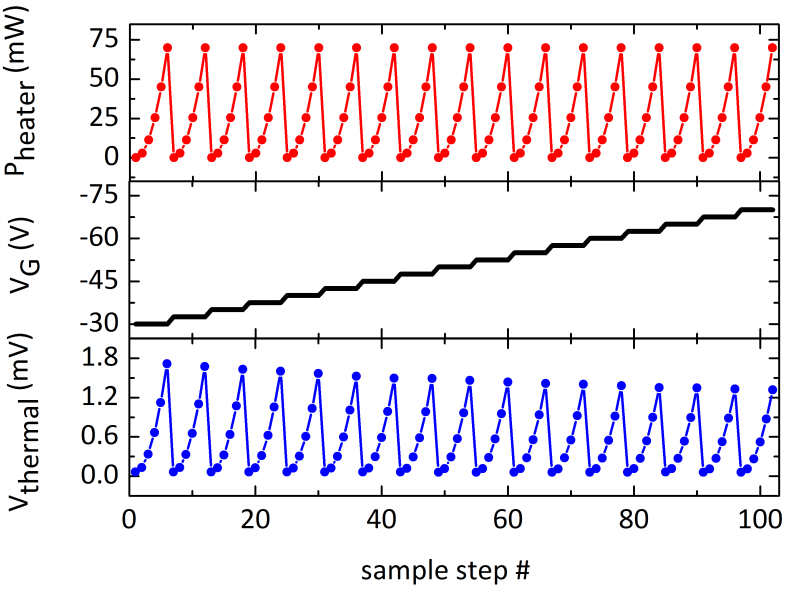

Figure 4.7: Built-in thermal voltage across IDTBT as a function of heater power and gate voltage sweeps. The gate voltage was swept from −30 V to −70 V in steps of −2.5 V.

was used when shifting the Seebeck coefficient on an $S - \log(n)$ plot to estimate its slope.

Fig. 4.9 (a) shows the temperature and carrier concentration dependence of the Seebeck coefficient in IDTBT in comparison to PBTTT. Fig. 4.9 (b) shows the field-effect modulated Seebeck coefficient of holes at room temperature in IDTBT in comparison to PBTTT and PSeDPBBT. The carrier concentration in the accumulation layer was calculated from the dielectric capacitance including the correction for a voltage onset of accumulation, −13 V for IDTBT. The voltage onset correction is necessary to account for any deep trap states that need to be filled before being able to induce an accumulation layer of mobile charges. There are three important general observations: (i) The Seebeck coefficients are large, several times k_B/e. (ii) They exhibit a clear reduction with increasing carrier concentration in the accumulation layer with a slope that is significantly larger for PBTTT and PSeDPPBT than for IDTBT. (iii) For all three polymers the Seebeck coefficient is temperature invariant within the maximum measurement error (±70 μV/K for the IDTBT device). It was noted previously that a temperature invariant Seebeck coefficient has been observed in crystalline small molecule semiconductors, such as pentacene and rubrene [66]. These measurements prove that in spite of their different transport physics, high mobility conjugated polymers exhibit a similar behaviour to small molecules as far as the Seebeck is concerned.

The large values of the Seebeck coefficient and its temperature independence can be explained by the simple polaronic model which makes the key assumption that the density of states is sufficiently narrow compared to k_BT so that all molecular sites remain thermally accessible across the measured temperature range. The entropy of mixing contribution to the Seebeck coefficient α_{mixing} is then given by $\alpha = \Delta S_{\text{mixing}}/e = (k_B/e)\ln[2(1-c)/c]$ with c being the

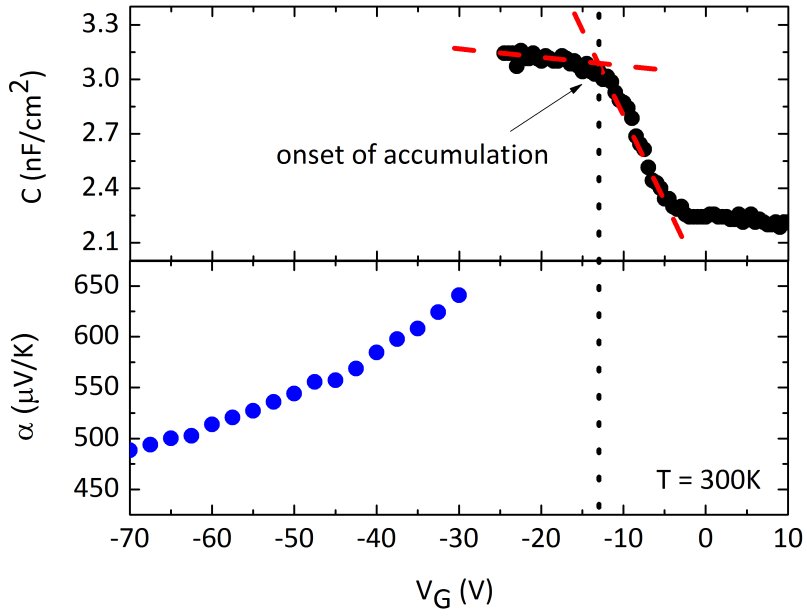

Figure 4.8: (top panel) Capacitance - Voltage measurements showing the onset of accumulation at ≈ -13 V within the device. (bottom panel) The Seebeck coefficient measured in full accumulation.

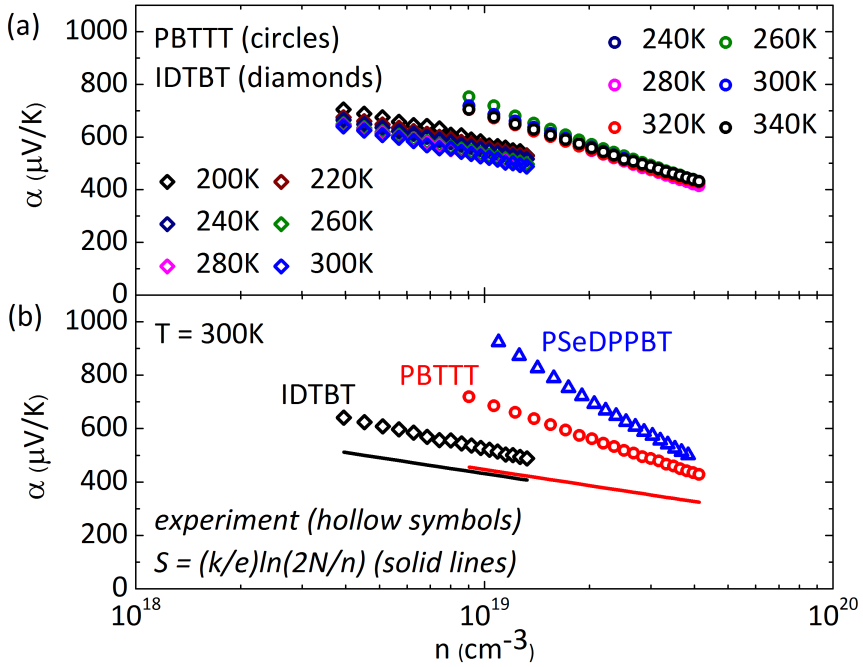

Figure 4.9: (a) Temperature invariance and carrier concentration dependent Seebeck coefficient for IDTBT in comparison to PBTTT (b) The carrier concentration dependence of IDTBT, PBTTT and PSeDPPBT at 300 K showing that IDTBT has the smallest slope.

fractional occupancy of states $c = n/N$ [99]. Here, n charge carriers are distributed over N thermally available states. The factor of 2 comes from the inclusion of spin 1/2 degeneracy. In the limit $c \ll 1$, as is typically the case in an organic FET, this formula takes the form $\alpha = k_B/e \times \ln(2N/n)$ such that the slope of $\alpha - \log(n)$ is $-k_B/e \times \ln(10) \approx -200$ μV/K/decade. The solid red and black lines in Fig. 4.9 (b) are plots of this narrow band formula for IDTBT and PBTTT, respectively. For this we estimated the total number of available states per unit volume, N, by assuming that each repeat unit of the polymer contributes one state, i.e., $N = 7.44\times10^{20}$ cm^{-3} (IDTBT) and $N = 8.86\times10^{20}$ cm^{-3} (PBTTT) based on the reported unit cell parameters for the two polymers [94, 82]. The narrow band polaron Seebeck formula provides an explanation of the temperature independence of α and is also consistent with the large magnitude of the measured Seebeck coefficient. However, the slope of $\alpha - \log(n)$ is higher in both polymers than what is expected in theory. Note that the slope is independent of the choice of N as N only effects the magnitude of α.

To explain the deviation of the slope from the ideal value we once again take into account that a certain concentration n_{trap} of the total concentration of gate voltage induced charges n may not participate in conduction because they become trapped. The same model was invoked when explaining the Seebeck coefficient in PBTTT in Chap. 3. If these trap states are sufficiently shallow, i.e., within an energy k_BT of the narrow band of charge transporting states assumed above (refer to appendices), then the chemical potential for holes will be significantly above both the charge transporting and the trap states and we expect the Seebeck coefficient to remain temperature independent. The narrow band polaron Seebeck formula in the presence of a trap density of states was already shown to be;

$$\alpha = \alpha_{\text{vib}} + \frac{k_B}{e}\ln(2) + \frac{k_B}{e}\ln\left(\frac{N}{n - n_{\text{trap}}}\right). \tag{4.2}$$

Here we have also included a carrier concentration independent term due to the vibrational entropy ΔS_{vib}. The slope of the Seebeck coefficient plotted against the logarithm of the carrier density is

$$\frac{\partial\alpha}{\partial\log(n)} = -\frac{k_B}{e}\ln(10)\left(\frac{n}{n - n_{\text{trap}}}\right) = -\frac{k_B}{e}\ln(10) \times f. \tag{4.3}$$

Thus, one sees that losing some carriers to shallow traps increases the magnitude of the slope from its trap free value $-(k_B/e)\ln(10)$ by a factor $f = 1/(1 - n_{\text{trap}}/n)$. As is evident from Fig. 4.9, the slope of $\alpha - \log(n)$ is the smallest for IDTBT compared to PBTTT and PSeDPPBT. The slope in IDTBT is $-(k_B/e)\ln(10) \times 1.5$, while that for PBTTT and PSeDPPBT are $-(k_B/e)\ln(10) \times 2.2$ and $-(k_B/e)\ln(10) \times 3.8$, respectively. Using the above enhancement factors $f = 1.5$, 2.2 and 3.8 for IDTBT, PBTTT and PSeDPPBT, the corresponding ratios of the trap density to the carrier density n_{trap}/n are 0.3, 0.5 and 0.7 respectively. Within the measured gate voltage range this ratio does not appear to vary significantly with gate voltage. This is consistent with the assumption made above that the trap states are shallow and lie within an energy k_BT of the narrow band of charge transporting states, as shown in the appendices. We arrive at the

important conclusion that while in PBTTT and PSeDPPBT the majority of gate-induced charge carriers remain trapped, in IDTBT we are approaching a disorder/trap-free transport regime in which the majority of gate-induced carriers participate in transport.

Eq. 4.2 can also be used to estimate the contribution of vibrational entropy α_{vib} to the measured Seebeck coefficient. α_{vib} is found to be between 50 - 100 μV/K for IDTBT. Although there are no documented estimates of α_{vib} in semiconducting polymers, α_{vib} was reported to be on the order of 100 μV/K in Boron Carbides [62]. In small molecules like pentacene, α_{vib} may be further enhanced to values up to $\sim$ 265 μV/K due to the presence of additional vibrational modes as reported earlier [70]. The estimate of α_{vib} is sensitive to the choice of N. If N were smaller, α_{vib} would have to be larger to explain the large magnitude of the measured Seebeck coefficient. We emphasize that the magnitude, the carrier concentration dependence and temperature invariance of the experimental Seebeck coefficient was very reproducible across multiple devices fabricated from the three polymers.

The simple framework adopted here to interpret the Seebeck data does not depend on specific assumptions about the nature of the charge transporting electronic states, i.e. whether they are localized or extended, or the detailed shape of the density of states. What is needed to explain the experimental data consistently, in particular the temperature invariance and large magnitude of the Seebeck coefficient, is the assumption that the density of states, including any tails due to localized states not contributing to transport, must be sufficiently narrow relative to $k_{\mathrm{B}}T$, such that the chemical potential does not enter the density of states but the majority of mobile states within the density of states remain thermally accessible. If there were a broad distribution of localized trap states below a mobility edge or transport level, E_{μ} , as is the case for example, in amorphous silicon [72], [73] or in disordered organic materials [86], the statistical shift of the chemical potential, E_{F}, with temperature would only be weak. In this case one would expect a pronounced temperature dependence of the Seebeck coefficient according to $\alpha \approx \Delta S_{\mathrm{mixing}}/e \approx (k_{\mathrm{B}}/e)((E_{\mathrm{F}} - E_{\mu})/(k_{\mathrm{B}}T) + A)$ [64], [70], where A is the so-called heat-of-transport constant. Our data are also not consistent with a percolation model of transport in which charge transport happens only along a few ordered tie chains interconnecting polymer crystallites embedded in an otherwise disordered and amorphous polymer network [92], since this would imply a too small number N of accessible states. To explain the large magnitude of the Seebeck coefficient without having to invoke nonphysically large vibrational contributions we need to assume a value of N close to the maximum consistent with the structure of the polymer, i.e., one state contributed per polymer repeat unit. Similarly, if the distribution/bandwidth of the mobile states was much wider than $k_{\mathrm{B}}T$, it would also be difficult to rationalize the large magnitude of the Seebeck coefficient. With the simple model used here it is difficult to provide a sufficiently accurate upper limit for the bandwidth in order to judge whether the narrow bandwidth is merely a result of weak disorder and the intrinsically weak intermolecular interactions or whether polaron bandwidth narrowing effects [41] need to be invoked.

Finally, to obtain a complementary assessment of the differences in energetic disorder between

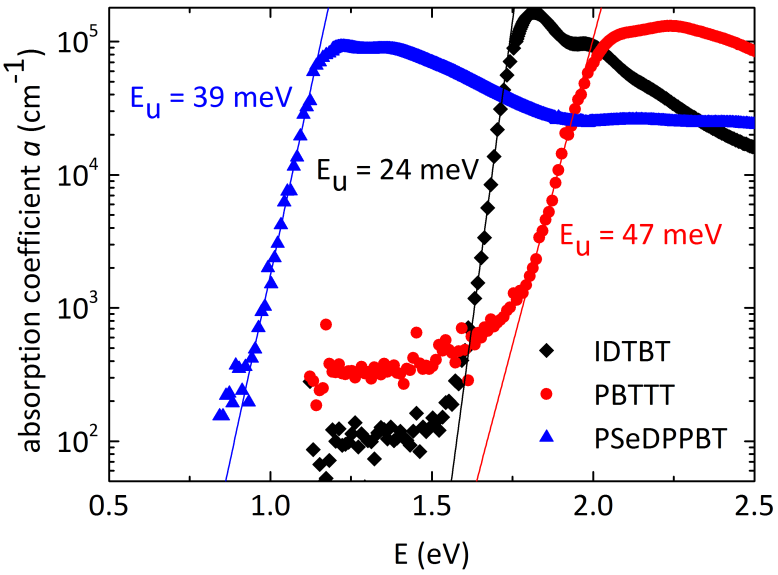

Figure 4.10: Absorption coefficient measured from Photothermal Deflection Spectroscopy on the three different polymers PBTTT, PSeDPPBT and IDTBT. Measurements courtesy of Mark Nikolka and Aditya Sadhanala.

the three polymers we measured their thin film optical absorption using the Photothermal Deflection Spectroscopy (PDS) technique (Fig. 4.10). PDS provides a very sensitive method to detect sub band-gap tail states from the optical absorption spectra using a parameter known as the Urbach energy, E_u. E_u is the parameter within the optical absorption coefficient $a(E) = a_0 \exp((E - E_\mathrm{g})/E_\mathrm{u})$, for $E < E_\mathrm{g}$, and provides a quantitative measure of energetic disorder in the excitonic joint density of states close to the band edge, measured in units of energy/decade. We have previously found that for a wide range of polymers the Urbach energy extracted from PDS is not only strongly correlated with the T_0 values extracted from fits of device characteristics, but in fact $E_\mathrm{u} \approx k_\mathrm{B}T_0$ [54]. An absolute value of the absorption coefficient was obtained by scaling PDS with UV-vis absorption spectra and corresponding film thicknesses. We find that IDTBT exhibits a very low Urbach energy of 24 meV, which is less than $k_\mathrm{B}T$ at room temperature and to the best of our knowledge the lowest value ever reported in a conjugated polymer semiconductor. In comparison, PBTTT and PSeDPPBT exhibit higher Urbach energies of 47 meV and 39 meV, respectively. In addition, the Urbach energy for amorphous silicon was measured to be around 50 meV [102]. The PDS results are fully consistent with the exceptionally low degree of energetic disorder in IDTBT deduced from the transistor characteristics and the Seebeck measurements.

4.4 Summary

This work provides important insights into the transport physics and guidelines for the molecular design of high mobility conjugated polymers. We have produced consistent evidence from independent transport and spectroscopic measurements that the density of states in IDTBT is exceptionally narrow compared to other conjugated polymers and that the majority of states is thermally accessible near room temperature, i.e., the energetic disorder among transport sites and the width of any tails of shallow trap states is comparable or less than $k_{\mathrm{B}}T$. In polymers such as IDTBT we are approaching an intrinsic transport regime that is no longer dominated by energetic disorder and in which all molecular sites are thermally accessible and the majority ($\approx 70\%$) of gate-induced charge carriers contributes to transport. Our results clearly demonstrate that in polymers without well-defined crystallinity, but extended backbone linearity, coplanarity and well defined molecular orientation across the entire film [93] it is possible to achieve an exceptionally low degree of energetic disorder that facilitates both the fast intrachain transport along the polymer backbone as well as the occasional interchain hopping in locations where adjacent chains come close. In this transport regime it should be possible to further optimize charge carrier mobilities by improving intrinsic, molecular transport parameters, including intermolecular transfer integrals, polaronic reorganisation energies and possibly thermal fluctuations. The insight gained in this work on the microscopic origin of the high mobility in IDTBT should inspire new molecular motifs for the design of even higher mobility conjugated polymers and should allow entering a regime of transport and photophysics that has previously not been accessible.

Chapter 5

Ambipolar Seebeck coefficients in PSeDPPBT

5.1 Introduction to PSeDPPBT

PSeDPPBT is a low band-gap ambipolar co-polymer whose monomer contains a selenophene flanked diketopyrrolopyrrole (DPP) unit together with a benzothiadiazole (BT) unit. The ambipolar polymer PSeDPPBT falls under a class of donor-acceptor (D-A) co-polymers, popular for their high performance ambipolar charge transport as a consequence of their highly delocalised π-conjugated HOMO and LUMO, strong intermolecular $\pi - \pi$ interactions and a low band-gap [103, 104]. The strong intermolecular interactions are a consequence of charge transfer between the donor and acceptor units within the polymer, also contributing to improved coplanarity within the polymer backbone. Fig. 5.1 shows the structure of PSeDPPBT, pointing out the DPP unit and the BT unit. The DPP unit is functionalised with a branched alkyl side chain. Both the DPP and the BT units are electron acceptors, while the thiophene or selenophene rings that flank the DPP unit behave as electron donors thus rationalising the D-A moiety within the polymer. Substituting thiophene rings by selenophene within PDPPBT has been shown to improve the mobility of the electrons within the ambipolar copolymer as a consequence of lowering the LUMO level thus facilitating better electron injection. A. J. Kronemeijer compared the electrical performance of PSeDPPBT with its thiophene cousin PDPPBT and found that the effect of selenium substitution leads to enhanced electron and hole field-effect mobilities of 0.84 and 0.46 cm^2/Vs, respectively, within PSeDPPBT as compared to PDPPBT [105].

Fig. 5.2 shows the HOMO and LUMO energy levels of PSeDPPBT in relation to the Fermi level of Au. The bandgap of PSeDPPBT is between 1.05 eV and 1.32 eV, smaller in comparison to the 1.48 eV seen in PDPPBT [105]. PSeDPPBT is also known to have an enhanced order in the solid state compared with PDPPBT [105], a feature that is most probably tied to the fact that selenium is larger in size compared to sulphur. Quantum chemical calculations that model the molecular orbital distributions and the extent of delocalisaion within the PSeDPPBT polymer backbone are shown in Fig. 5.3, taken from [105]. The calculations were done on a

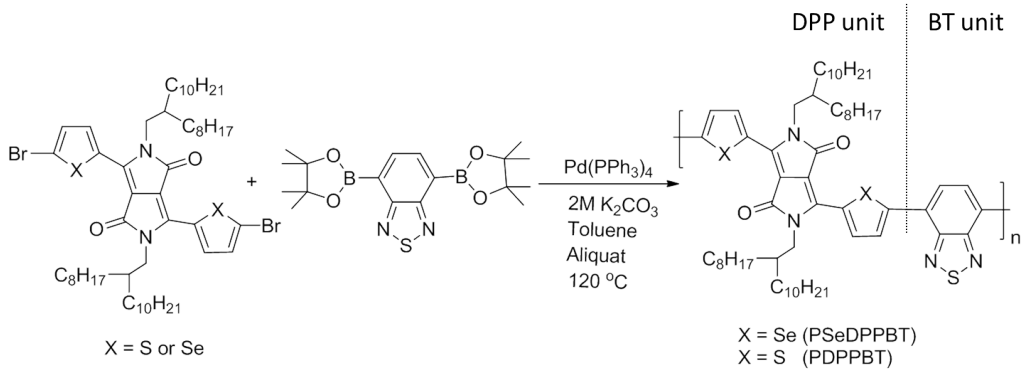

Figure 5.1: Synthesis route for PSeDPPBT (and PDPPBT) polymers by Suzuki polycondensation. Shown using a dotted demarcation are the two units that compose PSeDPPBT, the DPP unit and the BT unit. Image adapted from [105].

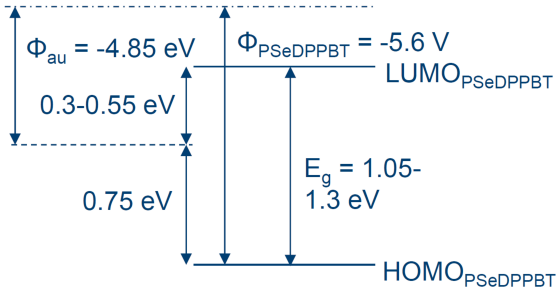

Figure 5.2: Energy levels within the low band-gap ambipolar polymer PSeDPPBT.

PSeDPPBT polymer with methyl functional units on the DPP. The molecular orbitals, HOMO and LUMO, are extensively delocalised on the polymer backbone as shown. This contrasts many D-A copolymers where the LUMO is localised on the electron accepting core of the polymer, and ends up limiting electron transport since intermolecular hopping is most effective only when the localised LUMO levels line up with each other [106]. It is the extensive delocalisation of the molecular orbitals on the polymer backbone that explain good ambipolar transport within this polymer, making it useful for practical applications such as ambipolar logic [105].

The results contained in this Chapter demonstrate a successful measurement of both electron and hole Seebeck coefficients within PSeDPPBT. At high channel accumulation the Seebeck of electrons and holes are shown to be balanced, and evidence is presented for hole transport being under an increased influence of disorder compared to electrons. This result is consistent with the mobilities measured for the two species within the ambipolar FET.

5.2 Electrical characteristics of the on-chip PSeDPPBT device

Fig. 5.4 shows representative output characteristics of a bottom-contact top-gate patterned ambipolar polymer PSeDPPBT device. A layer of 300 nm PMMA was used as the gate dielectric and the device looked exactly as that pictured in Fig. 2.1 shown for PBTTT. The channel length

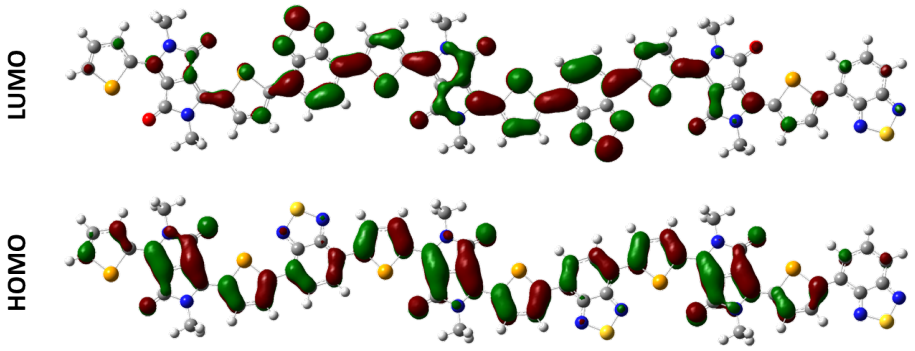

Figure 5.3: Energy-minimised structure (B3LYP/6-31G(d)) of a methyl-substituted SeDPPBT trimer with a visualisation of the LUMO and HOMO molecular orbitals at the top and bottom, respectively. The two colours red and green pertain to the phase of the electronic wavefunction. Image adapted from [105].

of the device was once again 50 μm while the channel width was patterned to be 1000 μm (not 1500 μm as was done in the PBTTT device). The electrodes fabricated were once again 17 nm Pt / 3 nm Au as in the case of the PBTTT device, and the metal gate electrode comprised 20 nm Al.

The regime for which V_G, $V_D < 0$ V shows hole accumulation within the channel, while the regime V_G, $V_D > 0$ V is that for electron accumulation. A textbook-like output curve showing distinct linear and saturation regions is however only seen for $|V_G| \geq 40$ V. For $V_G = 0$ V, the rise in drain current I_D is nonlinear and a plateau in I_D is not observed. This non-linearity is a signature of ambipolar transport. When both V_G and $V_D = -60$ V, the voltage between the gate and the drain is 0 V while the voltage between the gate and the source is -60 V. This causes holes to be injected from the source into the channel, thus contributing to a current in the saturation regime. On the other hand, when $V_G = 0$ V and $V_D = -60$ V, the voltage between the gate and the drain is 60 V while the voltage between the gate and the source is 0 V. This causes electrons to be injected at the drain, registering a finite current. Both electrons and holes are injected into the polymer using the same Pt/Au bilayer contact. For proper injection, the HOMO and LUMO levels of PSeDPPBT have to line themselves up with the Fermi level of the electrodes.

Fig. 5.5 (a) and (b) show the transfer curves for the device. The transfer curves exhibit a large $I_{ON} - I_{OFF}$ ratio of $\approx 10^6$ at $V_D = \pm 20$ V. The $I_{ON} - I_{OFF}$ ratio displays a decreased value at higher source-drain voltages due to a shift in the threshold voltage that results from applying different V_{DS}. The 'branching point', the voltage at which I_D shows a discontinuity, is the voltage at which the charge carriers that contribute to conduction invert in polarity. This branching point moves towards higher gate voltages for higher applied source-drain voltages since it takes a greater accumulation of charge carriers of one polarity to overcome the effect of injection due to the other.

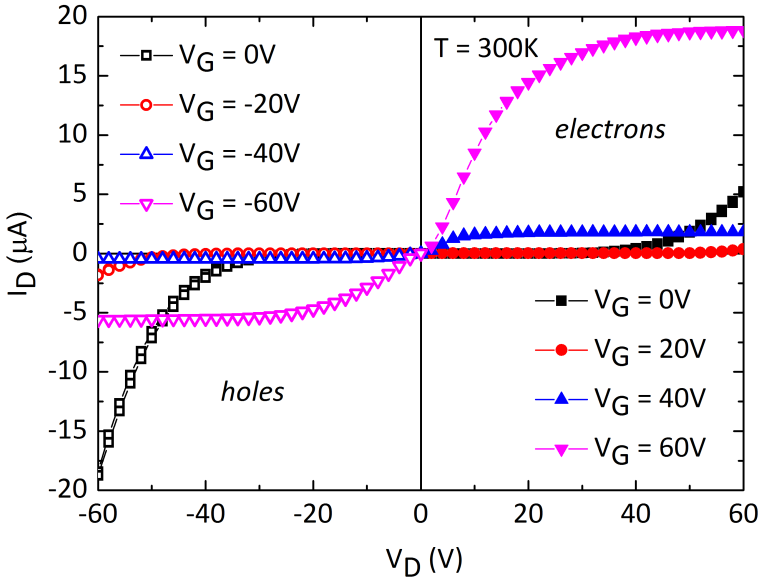

Figure 5.4: Representative output curves of a patterned PSeDPPBT device showing electron and hole accumulation at high $|V_G|$.

The saturation mobilities for electrons were extracted from Fig. 5.5 (b) for $V_D = -60$ V by using the slope of the square root of I_D between $V_G = 20$ V and 40 V. The saturation mobilities for holes were extracted, once again with $V_D = -60$ V, but using the slope of the square root of I_D in the field region between -60 V and -40 V at high temperatures or between -60 V to -50 V at lower temperatures. At lower temperatures a narrower window in the gate voltage, where the slope of the square root of drain current was estimated, needed to be used so as to circumvent the issue with increasing threshold voltages. Ideally, the saturation mobility of holes should have been estimated from Fig. 5.5 (a) in the region between $V_G = -40$ V and -20 V for $V_D = 60$ V so as to be consistent in estimating both electron and hole mobilities around the region where the drain-gate voltage $|V_{DG}| = 100$ V. On the device shown in this work, only transfer curves with measurement parameters shown in Fig. 5.5 (b) were measured at every temperature, and the mobilities were extracted from this data. It should be mentioned that had the saturation mobilities of holes been extracted from Fig. 5.5 (a) in the region between $V_G = -40$ V and -20 V, the reported hole mobility would be higher. As a quick example at 300 K, the hole mobility extracted from Fig. 5.5 (a) between $V_G = -40$ V and -20 V for $V_D = 60$ V is 0.17 cm^2/Vs while that extracted from Fig. 5.5 (b) between $V_G = -60$ V and -40 V for $V_D = -60$ V is 0.06 cm^2/Vs.

Fig. 5.6 shows the activation energies of (a) holes and (b) electrons in the range 340 K - 240 K. Both these activation energies were extracted from temperature dependent transfer curves similar to those shown in Fig. 5.5 (b). The activation energy of electrons was found to be 70 meV, while that for holes was 206 meV. The large discrepancy in the activation energies between electrons and holes shown here is most probably due to the reason explained earlier, i.e.,

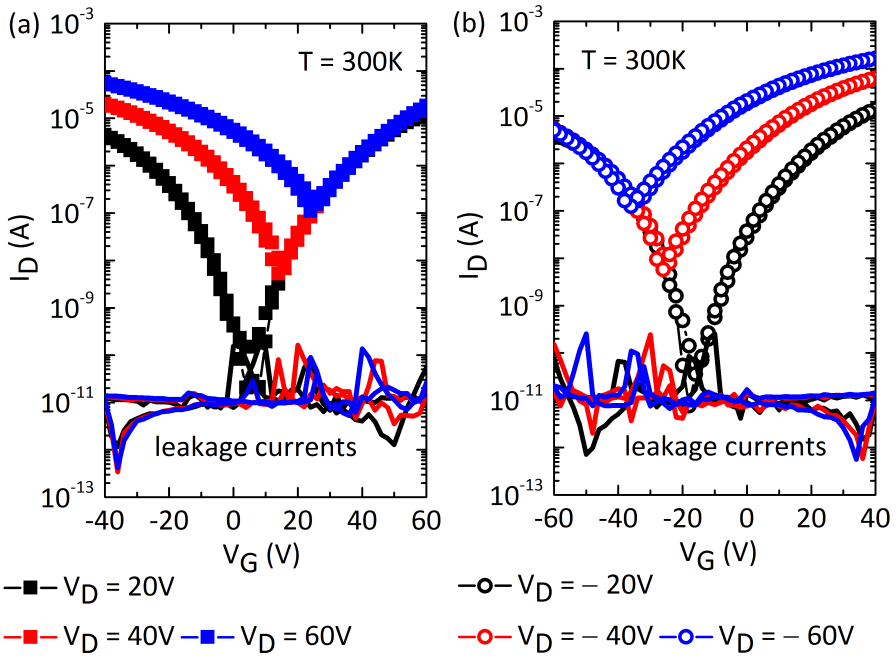

Figure 5.5: Representative transfer curves of a patterned PSeDPPBT device at 300 K showing electron and hole conduction for (a) positive applied V_D and (b) negative applied V_D.

both activation energies being extracted from measurements of the sort shown in Fig. 5.5 (b). Should the activation energy of holes have been extracted from Fig. 5.5 (a), the value would have been smaller. Unfortunately, such an estimate could not have been made because temperature dependent curves under the conditions shown in Fig. 5.5 (a) were not measured.

The mobilities for holes and electrons found in this patterned PSeDPPBT device at 340 K were 0.17 and 0.5 cm^2/Vs and 0.06 and 0.4 cm^2/Vs at 300 K respectively. These mobilities are slightly lower than the previously published values by Kronemeijer *et al.*, where the hole and electron mobilities were reported to be 0.46 and 0.84 cm^2/Vs respectively. This discrepancy once again is probably ascribed to the harsh patterning conditions that the device was subject to during which degredation may have taken place. Kronemeijer *et al.* also report an activation energy of electrons as being 200 meV, much higher than the 70 meV that was found in this device. For this, the explanation is that in the work of Kronemeijer *et al.*, the Au gold electrodes on the devices were subject to an oxygen plasma ashing step prior to deposition of the organic polymer so as to increase the work function of the Au electrodes bringing it closer to the HOMO level of the polymer to achieve better hole injection. Since carrier mobility in an organic FET is really sensitive to the treatment and type of electrodes used, the organic field-effect mobility is always a device dependent property, and not just a material specific property. The Seebeck devices on which the electrical characteristics were measured here were not subject to any ashing step. The work function of Au was hence comparatively closer to the LUMO level to facilitate better electron injection displaying a lower activation energy.

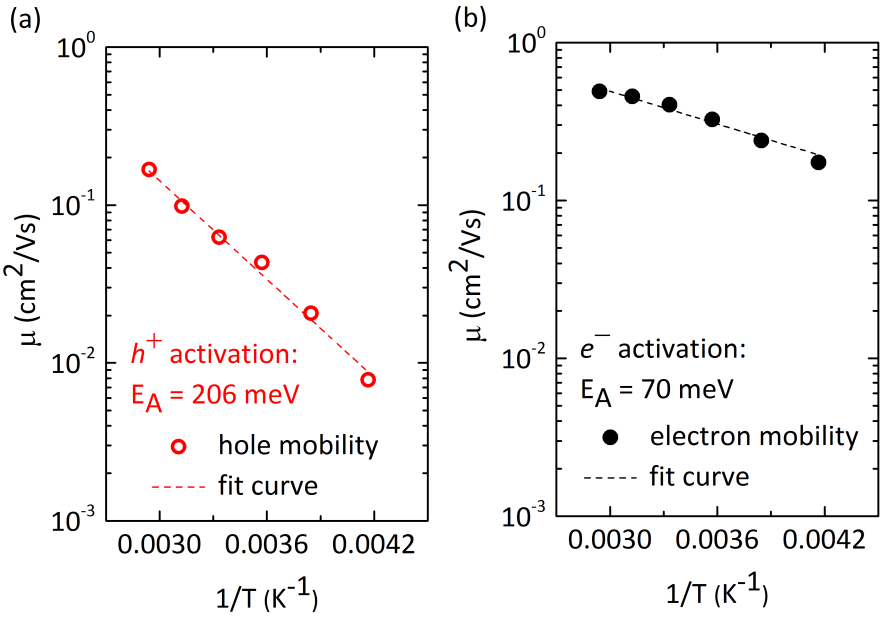

Figure 5.6: High field activation energies at for (a) holes (b) electrons in the PSeDPPBT device.

5.3 Seebeck coefficients in PSeDPPBT

Fig. 5.7 shows a typical sequence of measurements of the built-in thermal voltage in the ambipolar polymer PSeDPPBT as a function of heater power and gate voltage. As is the adopted procedure of measurements of the Seebeck in this thesis, the heater power was swept parabolically upto 60 mW for every applied gate voltage, and the thermal voltage (also seen to be parabolic) was measured simultaneously. The sequence is similar to that shown in Fig. 2.7 for PBTTT, but includes both positive and negative gate voltages. PSeDPPBT exhibits balanced electron and hole conduction with comparable magnitudes of electron and hole mobilities. As shown previously, for the device whose Seebeck coefficient is measured here, the electron mobility at high gate fields is 0.5 cm^2/Vs while the hole mobility at high gate fields is 0.2 cm^2/Vs at 340 K. The activation energy for holes was observed to be higher than that for electrons. When the gate voltage is swept from -80 V to $+80$ V, the thermal voltage initially increases in magnitude and eventually changes its polarity. The magnitude of the measured thermal voltage depends on the density of charge carriers in the accumulation layer while the polarity of the thermal voltage depends on the type of charge carriers being induced in the channel. In the gate voltage regime around 0 V where the channel turns off, the resistance of the organic semiconductor is large and begins to approach the input impedance of the voltmeter. In this region, a reliable measurement of the thermal voltage is not possible. What has not explicitly been shown here is the elaborate calibration of the on-chip thermometers and the estimate of the on-chip differentials. The procedure for this is the same as that illustrated previously in Chap. 2. The TCR of the sensors on the PSeDPPBT chip was 5.1 Ω/K. It was different from that for the PBTTT device, and the other devices, only because of an inhomogeneity in the film

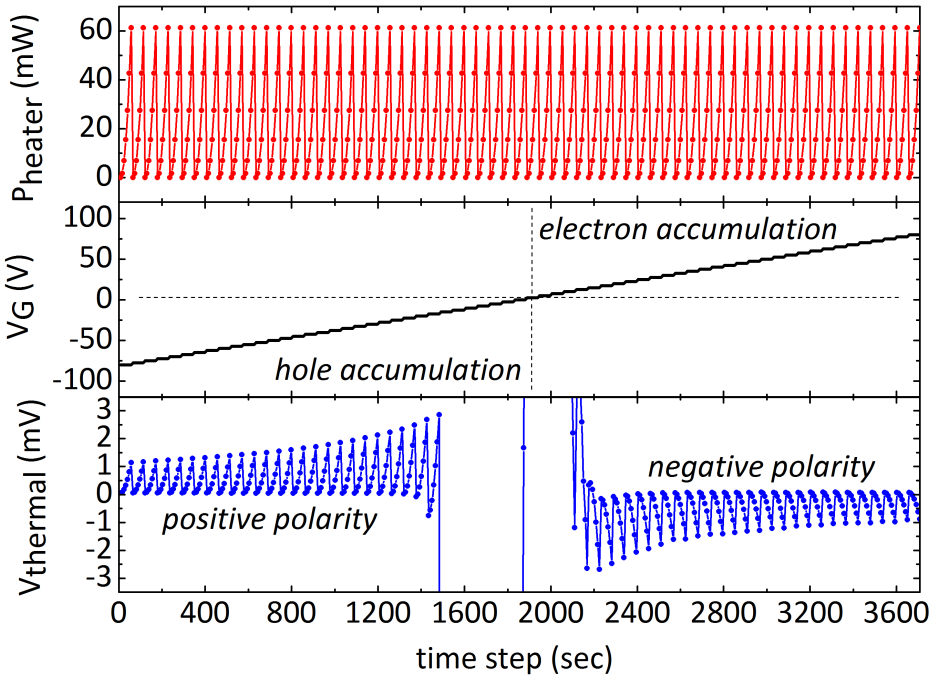

Figure 5.7: Measured thermal voltage as a function of a parabolic sweep in heater power at different gate voltages in the ambipolar polymer PSeDPPBT. In the hole accumulation regime, the thermal voltage has a positive polarity. In the electron accumulation regime, the thermal voltage has a negative polarity.

thickness that results during deposition of Pt and Au. Many devices were processed at the same time and those that were mounted slightly off axis from the center of maximum flux would have a slightly lesser thickness or a thickness that is non-uniform across the device. This is however of no negative consequence to the measurement of the Seebeck coefficient as long as the TCR and the temperature differentials on every chip were calibrated/estimated independently.

Fig. 5.8 shows a plot of the thermal voltage measured in Fig. 5.7 as a function of the estimated temperature differential ΔT for a few gate voltages, both positive and negative. The temperature differentials were estimated using the same heater power sweep shown in the upper panel of Fig. 5.7, and went up to a maximum of 1.6 K across the 50 μm channel length. The offset voltage measured, i.e, the voltage measured across the channel in the absence of a temperature difference was always around 50 μV. This was a typical offset voltage seen in all our measurements, and is about 3 % the magnitude of the maximum measured thermal voltage. Its effect can hence be neglected. Once the polymer film starts getting resistive either owing to insufficient channel accumulation (low applied gate voltages) or low temperatures, the offset increases. As an example, for an applied gate voltage of $\pm$20 V shown in Fig. 5.8 using wine coloured triangles, the voltage offset increased to around 80 μV. For any offset beyond 100 μV, the Seebeck coefficient extracted from the thermal voltage measurements starts becoming unreliable and should not be misunderstood for a real effect.

The Seebeck coefficients extracted from the raw thermal traces shown in Fig. 5.7 are plotted in the bottom panel of Fig. 5.9 at 300 K. The measured gate voltage modulated Seebeck coefficient of the ambipolar polymer clearly contrasts that of PBTTT at low gate fields, $0 < |V_{\mathrm{G}}| < 15$ V. A plateau is not observed since the device is not unintentionally doped and hence turns off completely.

The top panel of Fig. 5.9 shows a measurement of the device capacitance. For positive applied gate voltages, the electrons are accumulated in the channel while for negative applied gate voltages, holes are accumulated. The capacitance measurement was done between $\pm$35 V as this was the limit to the capability of the impedance analyser used for these measurements. The onset of accumulation was the voltage at which the linear region at low voltages and the plateau at high voltages intersect. In the case of holes, this onset voltage V_{ON}, was about -18 V as shown. For electrons, the onset voltage was extracted to be around $+25$ V. It was impossible to measure a meaningful thermal voltage signal between -20 V and $+20$ V as the device was highly resistive in this region owing to insufficient accumulation of charge carriers in the channel. Once again, it should be mentioned that a comparison between the gate voltage modulated Seebeck coefficient and the device capacitance is more appropriate as both measurements are performed under the absence of a source-drain voltage, and the accumulation of charge carriers within the channel is solely important for the measured quantities.

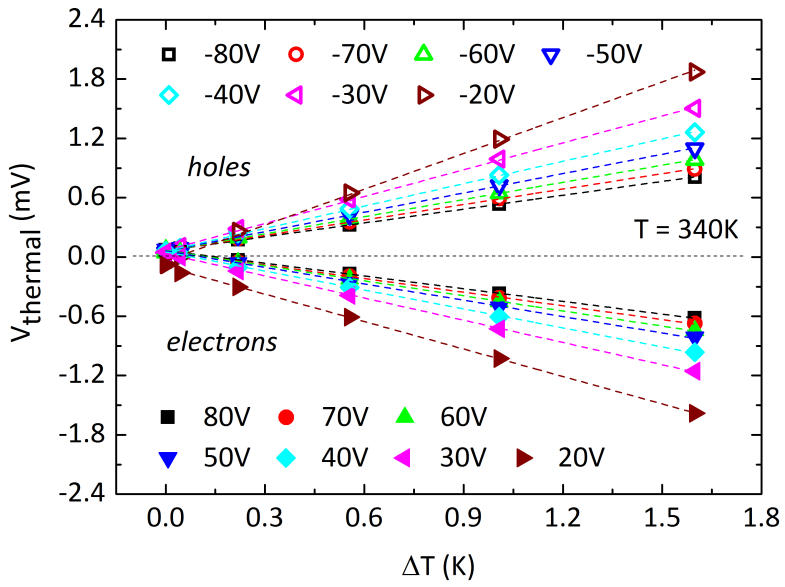

Figure 5.8: The Seebeck coefficient of electrons and holes are slopes of V_{thermal} versus ΔT for different gate voltages.

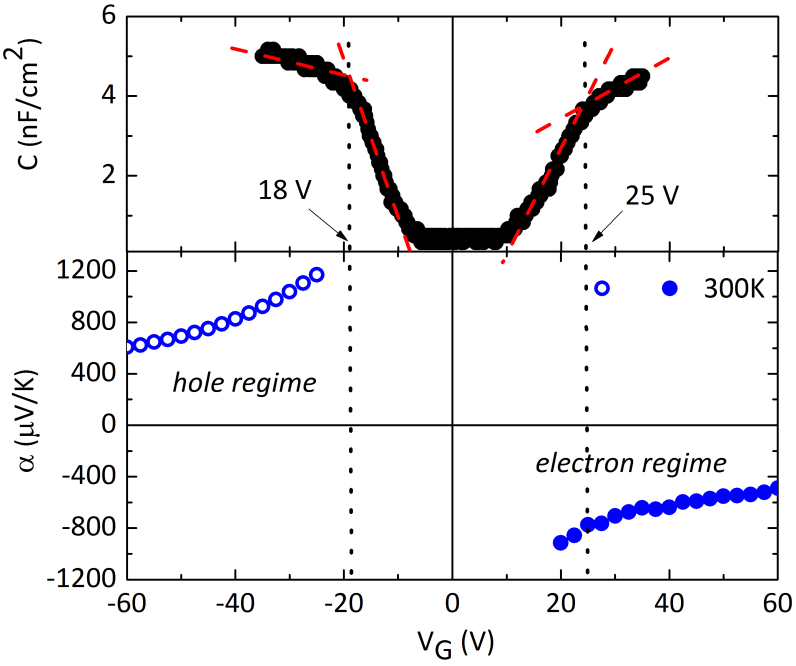

Figure 5.9: Measurements of device capacitance (C-V) estimate the turn-on voltage V_{ON} of the device. Shown is a comparison of the C-V measurement with a gate voltage modulated Seebeck measurement at 300 K. The Seebeck coefficient can be measured only once accumulation within the device is complete.

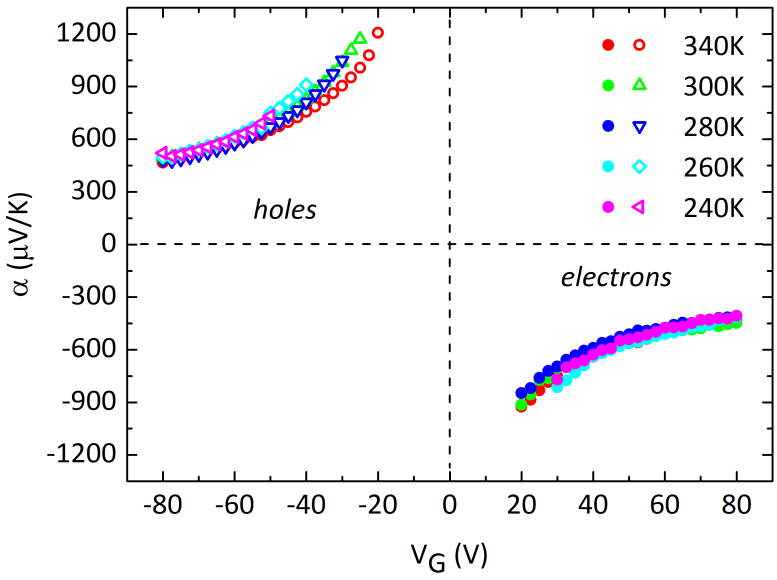

Figure 5.10: Temperature and gate voltage dependence of the Seebeck coefficient in PSeDPPBT.

5.4 Temperature dependence of the Seebeck in PSeDPPBT

An unambiguous insight into the underlying charge transport mechanism in organic semiconducting FETs is got by studying the temperature dependence of the Seebeck coefficient. In the case of PBTTT, it was shown that the Seebeck coefficient was temperature invariant within the measurement window 240 K - 340 K. Fig. 5.10 probes the Seebeck in the same temperature window, for both electrons and holes. At low temperatures, it became increasingly difficult to reliably measure the Seebeck as the organic polymer became increasingly resistive. This is also the reason why at 240 K for example, the Seebeck coefficient for holes could be measured only between $V_G = -50$ V and -80 V. As the temperature is raised from 240 K to 340 K, this gate voltage window where the Seebeck can be successfully probed widens. A similar effect is seen in the case of electrons, but is not as pronounced as for holes since the electrons in the system are far more mobile than holes. The activation energy of electrons is also far smaller. The Seebeck coefficient of electrons can hence be reliably measured between $V_G = 30$ V and 80 V all the way down to 240 K.

As can be seen from Fig. 5.10. The Seebeck coefficients are large, several times k_B/e, they are modulated using an applied gate field, and are temperature invariant. These three observations rationalise the use of a polaronic model for the Seebeck coefficient which agree with all the aforementioned characteristics. In addition, from Fig. 5.10, one sees that the Seebeck coefficient at $V_G = \pm 80$ V approaches the same value of 450 μV/K. At $V_G = \pm 80$ V, the charge induced in the accumulation layer is the same being $CV_G/e = 5.16\times10^{19}$ cm^{-3}. The fact that the Seebeck coefficients are the same for both electrons and holes at high gate fields, despite them having disparately different carrier mobilities and activations, means the Seebeck coefficient is

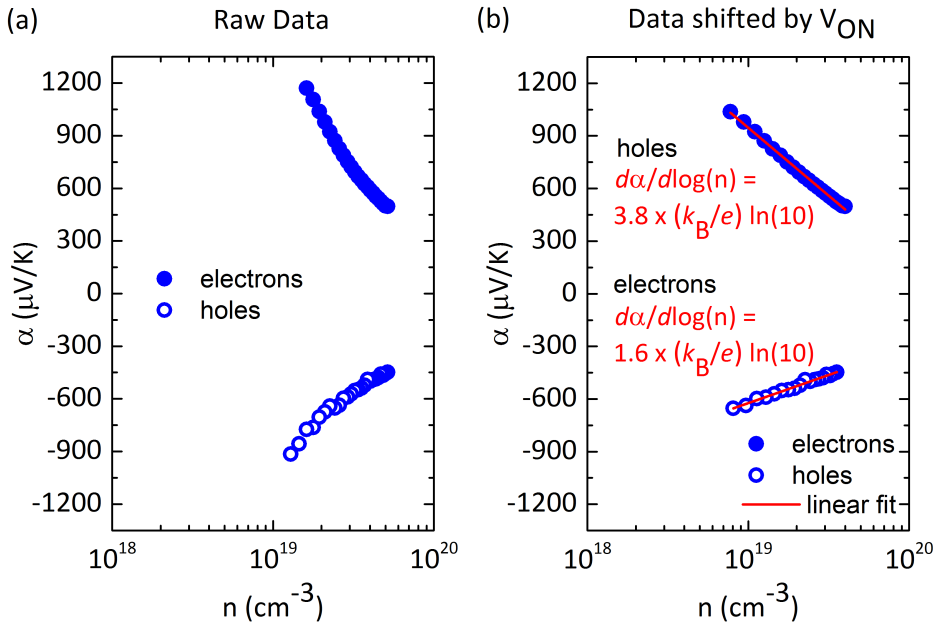

Figure 5.11: (a) The Seebeck coefficient of electrons and holes plotted as a function of carrier concentration, the latter computed directly from CV_G/e. (b) The Seebeck coefficient of electrons and holes plotted as a function of carrier concentration $n = C\left(|V_G| - V_{ON}\right)/e$. V_{ON} is extracted from capacitance measurements.

dominated by an entropy-of-mixing contribution that depends on the ratio of the induced charge carrier density to the total number of available states. From of disorder view point, one can speculate that the energetic disorder which dominates charge transport at low charge carrier accumulation is overcome at high applied gate fields, thus causing the Seebeck coefficient of electrons and holes to equalise.

5.4.1 Seebeck coefficient interpreted within a narrow band model

Using a trap dependent narrow band polaron model of the form of Eq. 3.12, the extent to which trapping is important for electron and hole transport can be quantified. Fig. 5.11 (a) plots the Seebeck coefficient of electrons and holes at 300 K against the carrier concentration in the channel that does not account for an onset voltage. Fig. 5.11 (b) shows the slopes of the Seebeck coefficient with carrier concentration when an onset voltage is accounted for. The onset voltages used for holes and electrons were $V_{ON} = -18$ V and +25 V respectively. Shown also in Fig. 5.11 (b) are the relevant slopes for electrons and holes. It is clear that the slope in the Seebeck coefficient for electrons is smaller than that for holes, thus hinting at a smaller influence of traps in electron transport in comparison. The enhancement factor f is 3.8 for holes and 1.6 for electrons. The smaller slope of the Seebeck versus electron carrier concentration is also supported by the observation of a smaller activation energy as well as a higher carrier mobility. A possible explanation for the different extents to which holes and electrons are influenced by traps

may be related to torsional effects in the polymer backbone. It is likely that holes get trapped to a larger extent than electrons when the polymer chain is under the influence of torsion. This is a conclusion one arrives at when comparing PSeDPPBT to IDTBT. IDTBT is a polymer that is known to have a relatively planar backbone in comparison, a consequence of which leads to low disorder and a smaller f parameter. Torsion in the polymer backbone increases the extent of disorder, and hence the extent of carrier trapping. At this time however, such a claim remains preliminary and will need to be backed up with results from theoretical simulations.

In Chap. 4, the slope of the Seebeck for holes in PSeDPPBT was compared to the same in PBTTT and IDTBT. A comparison of the Seebeck slopes across polymer systems is arguably more effective when drawing general conclusions than is from a single result as that shown in Fig. 5.11 (b).

5.5 Summary

The Seebeck coefficient of the ambipolar polymer PSeDPPBT was investigated within the channel of an FET. The polymer showed Seebeck coefficients due to both holes and electrons depending on the applied gate voltage polarity, and approached the same magnitude at high applied gate fields. The slope of the Seebeck coefficient versus carrier concentration for electrons was smaller than that for holes hinting at a reduced effect of trapping on electrons. This reduced electron trapping was also reflected in a lower carrier activation as well as a higher saturation mobility for electrons as compared to holes in PSeDPPBT. Whether these differences between electrons and holes are an intrinsic property of the ambipolar polymer is a question that will need to be answered in the future.

Chapter 6

Band-like transport revisited

There has been a recent bout of interest in studying high mobility organic semiconductors, small molecules in particular, with the intent of classifying the nature of charge transport as being either band-like or hopping-like. Organic small molecules such as rubrene show field-effect mobilities on the order of 10 cm^2/Vs [66], and often outperform amorphous Si in their electrical performance. The possibility of having a mobility-edge or a conduction band within the energetic landscape of such high mobility organic semiconductors can hence not be excluded. This Chapter briefly enumerates the implication of voltage modulated Seebeck coefficient measurements on the classification of transport in organic semiconductors. Although the technique may not unambiguously confirm the presence of band-like transport in organic semiconductors, it can classify transport in materials as being either trap-free or trap-dominated. High mobility organic semiconductors displaying trap-free transport as characterised by the gate modulated Seebeck coefficient are potential candidates for band-like transport.

6.1 Band-like, hopping and trap-free transport regimes

The classification of transport regimes in organic semiconductors have traditionally been divided into either band-like or hopping-like. To classify organic semiconductors under either of these transport regimes, two techniques have been in regularly use. These techniques are (a) temperature dependent field-effect mobility and (b) the Hall effect. Hopping transport in organic semiconductors is characterised by a temperature variation in mobility of $\partial\mu/\partial T > 0$, where the mobility is thermally activated and obeys an Arrhenius law. Band-like transport on the other hand is characterised by the observation of $\partial\mu/\partial T < 0$, seen previously in the small molecules rubrene [107] and TIPS-pentacene [108]. The ideal Hall effect was successfully measured in rubrene [109, 110] and pentacene [111], small molecular systems that make convincing cases for the presence of a mobility edge within them beyond which band-like (or extended state) transport may take place. The Hall effect was also successfully measured in TIPS-pentacene, a result that strengthened the claim of band-like transport in this material [112]. More recently, the Hall effect was measured in an elecrochemically gated polymer poly(3-hexylthiophene) (P3HT) [113].

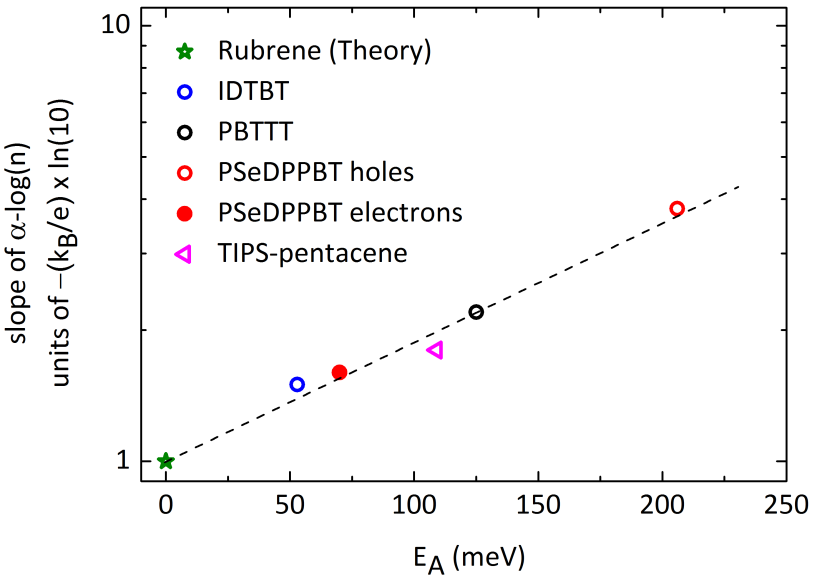

Figure 6.1: A super-plot of the slope of the Seebeck $\alpha-\log(n)$ in a variety of organic semiconductors studied in this thesis, as a function of their activation energies. When the temperature dependent mobility ceases to be thermally activated, i.e., $E_{\mathrm{A}} = 0$ meV and the slope of $\alpha-\log(n)$ has a magnitude equal to $-(k_{\mathrm{B}}/e) \times \ln(10)$, this is an indicator of activationless trap-free transport.

The P3HT device of Wang and co-workers had a mobility of 0.8 $\mathrm{cm}^2/\mathrm{Vs}$ and a small activation of 2.5 meV. The argument presented by them in support of band-like transport in P3HT was that using an ionic liquid gated device, a high induced carrier density $\sim 10^{21}$ cm^{-3} could be achieved thus filling up the density of disordered trap states, making the mobility edge accessible for transport.

All told, a true indicator of band transport in inorganic semiconductors is the measurement of Shubnikov de Haas oscillations as demonstrated in Graphene recently [114]. Shubnikov de Haas oscillations are oscillations in the resistivity of a material as a function of an applied magnetic field. The measurement is typically done at cryogenic temperatures. It gives an estimate of the effective mass in the material [115], a quantity that is strictly defined as a function of the curvature of the band through which transport takes place. When organic semiconductors are cooled to cryogenic temperatures, the charge carriers within them cease to be thermally active. This manifests itself as an increased resistance and makes a measurement of the Shubnikov de Haas effect very difficult if not impossible.

6.1.1 Correlation between $\partial\alpha/\partial\log(n)$ and activation energy E_{A}

In an attempt to find a third technique operable at high temperatures that can complement the measurements of temperature dependent mobility and the Hall effect in understanding the nature

of transport in organic semiconductors, a possible classification using the Seebeck coefficient is suggested here. The classification attempts to determine how close an organic semiconductor comes to displaying trap-free transport.

Within the wide-band picture, the Seebeck coefficient in a hole system is

$$\alpha = \frac{k_{\mathrm{B}}}{e}\left[\frac{E_{\mathrm{F}} - E_{\mathrm{V}}}{k_{\mathrm{B}}T} + A_{\mathrm{V}}\right]. \tag{6.1}$$

The slope of the Seebeck coefficient with carrier concentration n in this picture was shown previously to be

$$\frac{\partial\alpha}{\partial\log(n)} = -\frac{k_{\mathrm{B}}}{e}\ln(10). \tag{6.2}$$

This fact prompted a few research groups studying inorganic oxide materials to compare the slope in their experimentally measured Seebeck coefficient $\alpha - \log(n)$ with $-(k_{\mathrm{B}}/e) \times \ln(10)$ ≈ -200 μV/K/decade as an indicator for ideal band transport [85, 116, 117]. In the case of organic semiconductors under the influence of trap states, the slope of the Seebeck coefficient with carrier concentration n is enhanced by a multiplicative factor f depending on the extent of carrier trapping and

$$\frac{\partial\alpha}{\partial\log(n)} = -\frac{k_{\mathrm{B}}}{e}\ln(10)\left(\frac{n}{n - n_{\mathrm{trap}}}\right) = -\frac{k_{\mathrm{B}}}{e}\ln(10) \times f. \tag{6.3}$$

The measured slope is normally enhanced from what one expects for ideal band transport as demonstrated in the cases of PBTTT, IDTBT and PSeDPPBT in this thesis.

In the previous Chapters, when using the narrow band form of the Seebeck coefficient, the quantity $f = 1/(1 - n_{\mathrm{trap}}/n)$ was a constant, independent of both gate voltage and temperature owing to all the trap states being thermally accessible. If the narrow band model is to be set aside for once, and the disorder model invoked again, the density of mobile carriers within organic semiconductors can be considered thermally activated with an activation energy E_{A}, i.e,

$$n - n_{\mathrm{trap}} \propto \exp\left(-\frac{E_{\mathrm{A}}}{k_{\mathrm{B}}T}\right) \tag{6.4}$$

From the above two equations it then becomes clear that $\dfrac{\partial\alpha}{\partial\log(n)}$ is related to the activation energy E_{A} by

$$\ln\left(\frac{\partial\alpha}{\partial\log(n)}\right) \propto -\frac{k_{\mathrm{B}}}{e}\ln(10) + \frac{E_{\mathrm{A}}}{k_{\mathrm{B}}T} \tag{6.5}$$

Fig. 6.1 plots the slope of $\alpha - \log(n)$ together with the activation energy of a few organic semiconductors. Included in this plot is also the measurement of the Seebeck coefficient in TIPS-pentacene, the material whose crystalline form demonstrated band-like transport [108]. From this Figure, it is clear that as transport becomes gradually less thermally activated, the slope in the Seebeck coefficient also approaches the limit for ideal band transport. When organic semiconductors start to demonstrate a reduced influence from thermally activated transport, i.e, when $E_{\mathrm{A}} \to 0$ meV as in the case of rubrene [66] and TIPS-pentacene [108] at high temperatures, the slope of $\alpha - \log(n) \to -(k_{\mathrm{B}}/e) \times \ln(10)$. Indeed, in the case of rubrene, Wang and co-workers

theoretically computed the slope in the Seebeck and found it to be exactly $-(k_B/e) \times \ln(10)$ [16] as shown in Fig. 6.1.

From Fig. 6.1, it may be tempting to conclude that the observation of a diminishing activation energy together with a close to ideal slope in the Seebeck hints at band-like transport. After discussions with Prof. Sirringhaus however, it became clear that such a conclusion is ambiguous. The reason for this is two fold. (1) In an ideal inorganic semiconductor with well defined bands, the presence of trap states may also enhance the Seebeck's slope from its ideal value. (2) In an organic semiconductor under the influence of very few traps, the Seebeck's slope may approach its ideal value even though a hopping mechanism may still be at play. Although these two scenarios were not encountered in this thesis, the arguments remain valid and require a comprehensive set of measurements to either prove or disprove them. At this early stage however, it is conclusive to say that within a trap picture of charge transport, the gate modulated Seebeck coefficient can be used to characterise materials as being either trap-free, or trap-dominated. Materials with a small activation energy and a close to ideal slope in the Seebeck are less influenced by traps (since $f \to 0$) as opposed to those with either a higher activation energy and/or higher Seebeck slope.

Part of the future work plan is to measure both the field effect modulated Seebeck coefficient as well as mobility activation on a variety of solution processed organic semiconductors and oxides, and populate Fig. 6.1 with many more data points to arrive at a convincing universal trend. The work contained in this thesis has brought us to a point where a universal trend in the Seebeck coefficient's slope with activation energy seems to start appearing. It is hoped that this technique of measuring the gate modulated Seebeck coefficient will strengthen our understanding of the influence of traps in transport, and also that it shines light on whether organic semiconductors with activation-less transport and an ideal Seebeck slope hint at band-like transport in addition to trap-free transport.

6.2 Seebeck coefficient in TIPS-pentacene

The transfer curves of the TIPS-pentacene device included in Fig. 6.1 are shown in Fig. 6.2 (a) at 300 K. Unfortunately all the TIPS-pentacene devices fabricated and studied in this thesis had relatively low mobilities hovering only around 0.1 cm^2/Vs. These low mobilities may be due to the absence of long range order and the presence of structural defects incorporated in the TIPS-pentacene film during fabrication. Since the devices have a channel length of 50 μm, grain boundaries may have also been a limiting factor for the mobility. The 5 μm channel length TIPS-pentacene devices of Dr. Sakanoue had mobilities in excess of 1 cm^2/Vs and so a direct comparison cannot be drawn between the two. In the device shown here, TIPS-pentacene displayed an activation energy of 109 meV measured in the temperature range 325 K to 225 K. The corresponding slope of $\alpha - \log(n)$ at high applied gate voltages was around $-(k_B/e)\ln(10) \times 1.8$. In arriving at this value, the Seebeck curves were shifted using the usual procedure by the onset voltage determined from the capacitance (not shown), which in this case

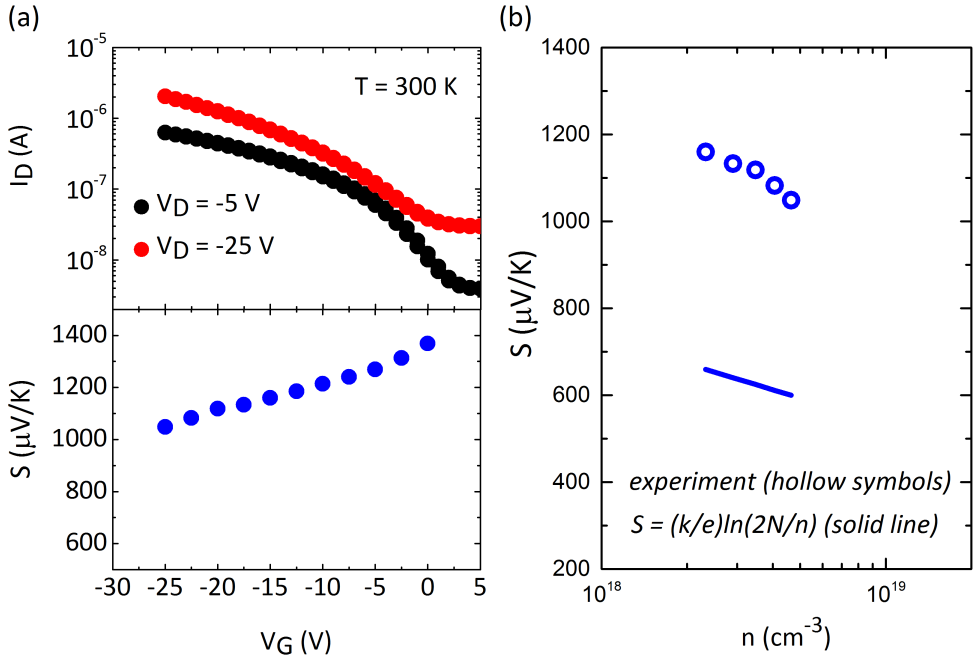

Figure 6.2: (a) Linear and saturation transfer curves in a patterned TIPS-pentacene device with W = 1.5 mm and L = 50 μm (top panel). The mobility of this device is $\mu_{\text{sat}} \sim 0.1$ cm^2/Vs. Seebeck coefficient measured within the same device at 300 K (bottom panel). (b) Seebeck coefficient as a function of carrier concentration.

was $V_{\text{ON}} = -5$ V. Fig. 6.2 (b) is a plot of the measured Seebeck coefficient in TIPS-pentacene for high applied gate voltages together with the narrow band prediction. In arriving at the theoretical estimate, one available state was assumed per TIPS-pentacene molecule having lattice constants documented in [118]. The total number of available states N was computed to be 2.43×10^{21} cm^{-3}. The Seebeck coefficient in the TIPS-pentacene device shown here could not be measured beyond $V_{\text{G}} = -25$ V since the gate leakage current increased substantially thus introducing errors in the measurement of the thermal voltage.

TIPS-pentacene has a much larger magnitude of the Seebeck coefficient compared to the investigated organic polymers. It is not difficult to notice that the Seebeck coefficient would have been around 1 mV/K at $V_{\text{G}} = -30$ V. Contrasting this with the Seebeck coefficient in IDTBT of Fig. 4.8 where at $V_{\text{G}} = -30$ V, $\alpha = 650$ μV/K, one notices a substantial difference. This is despite both the TIPS-pentacene and the IDTBT devices making use of a 500 nm Cytop gate dielectric. A large Seebeck coefficient on the order of a 1 mV/K was previously observed in the small molecules rubrene [66] and pentacene [70]. The difference of a few hundred μV/K in the Seebeck coefficient between small molecules and polymers is a feature that was previously explained as a contribution from enhanced vibrational entropy in small molecules [70]. Small molecules such as TIPS-pentacene are known to have strong intermolecular lattice thermal fluctuations as experimentally measured using thermal diffuse electron scattering [119]. Such intermolecular vibrational modes are not as strong in organic polymers. This is potentially a

reason for α_{vib} being larger in organic small molecules, thus enhancing the magnitude of the overall Seebeck coefficient. A systematic study of the enhanced vibrational contribution to the Seebeck coefficient seen in small molecules currently remains an open question and constitutes work planned for the future. Here, only a mention of this anomaly together with an elementary result that shows promise, is intended.

6.3 Summary

This Chapter made an attempt to illustrate a possible technique to probe the extent of trap-free charge transport in organic semiconductors. It linked the gate modulated Seebeck coefficient measurements on PBTTT, PSeDPPBT, IDTBT, TIPS-pentacene and rubrene with their respective activation energies for charge transport onto a universal plot. This plot demonstrated that a reduction in the activation energy of transport is accompanied by a reduction in the slope of $\alpha - \log(n)$. For ideal trap-free transport, $E_{\mathrm{A}} \rightarrow 0$ meV and $\partial\alpha/\partial\log(n) \rightarrow -(k_{\mathrm{B}}/e) \times \ln(10)$. Organic semiconductors that show an ideal trap-free behaviour in the Seebeck coefficient, together with the ideal Hall effect and a trend in mobility $\partial\mu/\partial T < 0$, may be candidates for ideal band-like transport.

Chapter 7

Conclusions and Outlook

This PhD thesis was about the measurement of a thermoelectric transport property called the Seebeck coefficient in solution-processed organic semiconductors. The research project itself was an idea that I came up with when I began my PhD at the University of Cambridge in 2010. The work contained herein provided an insight into the nature of disorder as seen from a thermoelectric standpoint, and helped make some significant scientific conclusions. This said, the pursuit of every blue-skies research project also uncovers important questions that need to be understood through further experimental investigation. It remains extremely difficult to bring ones research effort to the logical end within the time frame of a typical PhD thesis, and thus many of the unanswered questions will have to be accepted as guidelines or starting points for future research. This Chapter briefly recounts the salient contributions that the work contained in this thesis has made to the field of organic electronics. It also throws light on the few questions that are waiting to be answered.

The first novel contribution, previously never used in the study of thermoelectric properties on solution-processed organic semiconductors, was the use of a custom designed microfabricated architecture with integrated temperature sensors and a heater. The microfabricated device allowed for conventional FET measurements, as well as novel gate voltage modulated Seebeck measurements within the channel of the FET. The errors involved in the measurement of the Seebeck coefficient using such a microfabricated device are about 50 % smaller than that estimated by the few other groups that previously performed Seebeck measurements on organic semiconductors without such an on-chip architecture.

The second major scientific contribution of this thesis was in understanding the nature of disorder in organic polymers from a Seebeck standpoint. Three organic polymers were studied and the extent of gate voltage or carrier induced modulation in their Seebeck coefficients were correlated with their charge transport properties. The claim that charge transport in the polymer IDTBT is disorder-free as substantiated by its FET characteristics, was strongly supported by measurements of the gate voltage modulated Seebeck coefficient. In addition, the polymer PBTTT was shown to have a greater disorder than that in IDTBT from voltage modulated measurements of the Seebeck coefficient, as well as from conventional FET charge transport.

The Seebeck coefficient measured within the channel of the ambipolar polymer PSeDPPBT, was shown to have signatures of both electrons and holes depending on the applied gate voltage. The extent of modulation in the Seebeck coefficient of the two charge species was found to be different with electrons displaying a smaller influence of disorder than for holes. This result agreed with the fact that the mobility of electrons was higher than for holes and that the activation energy of holes was higher than for electrons.

The third major outcome was in the experimental confirmation that the Seebeck coefficient in small molecules is a few hundred μV/K larger than that measured in the organic polymers.

A minor side contribution of this thesis was in the development and use of a simple model for the Seebeck coefficient that accounted for its various entropic contributions. This model was developed together with Prof. David Emin at the University of New Mexico and does away with the many variable parameters used in disorder hopping models. While the entropy-of-mixing contribution remained dominant for organic polymers, experimental evidence was shown in favour of a large vibrational entropy contribution in organic small molecules. The model also included the presence of trap states that influence charge transport in organic semiconductors. It was shown that this model is applicable if the trap states are shallow and within a few $k_{\mathrm{B}}T$ of the states through which transport occurs. Since most organic semiconductors have narrow bandwidths on the order of 4 to 5 times $k_{\mathrm{B}}T$, the use of such a model is not unreasonable.

On careful scrutiny of the results contained in this PhD thesis, it becomes clear that two questions remain unanswered. The first pertains to the ambipolar polymer PSeDPPBT. Seebeck coefficients measurements on this polymer showed that electrons are under the influence of reduced disorder as compared to holes. This reduced influence of disorder on electrons is supported by the observation that electrons have a higher mobility as compared to holes. It was mentioned that a plausible reason for this is that torsion in the polymer backbone leads to greater trapping of holes than for electrons. Whether this difference between electrons and holes is intrinsic to the polymer is to be confirmed through simulation and is collaborative work planned for the future.

The second of the unanswered questions pertains to the Seebeck coefficient in small molecules being higher than that for organic polymers by a few hundred μV/K. An explanation for this observation was given based on the presence of stronger intermolecular vibrational modes in organic small molecules compared to organic polymers. This observation will need to be substantiated through further investigation of a spectrum of organic small molecules to ascertain its validity. Such a comprehensive set of Seebeck measurements on a few small molecules would be a potential topic of research, ideal for an M.Phil thesis in future.

Finally, it is my strong opinion that applied science must aim to develop technology that impacts society positively. To this end, a future research interest in Organic Thermoelectrics would be to quantify the thermal conductivity in a variety of organic semiconductors and document the thermoelectric figures of merit (ZT) for each of them. Such a listing of ZT values for different organic polymers is a first step in the development of commercial organic

thermoelectric modules that convert waste heat to useful energy at temperatures close to room temperature.

Appendices

Appendix A

Ambipolar Field-Effect Transistors based on DPP and Benzotriazole

This section of the appendices is not directly related to the measurement of the Seebeck coefficient, but constitutes part of the collective work done for this PhD thesis. It has been included here for reasons of comprehensiveness. The section is about ambipolarity in co-polymers with a diketopyrrolopyrrole (DPP) monomer unit and a functionalised Benzotriazole (BTz) monomer.

A.1 Introduction

Solution-processed polymer semiconductors are heavily investigated in order to realize flexible cost-efficient organic electronic devices. In order to improve the performance of organic electronic components, it is a prerequisite to determine structure-property relationship in these systems. Polymeric semiconductors have been developed over the last decade resulting in a steady increase in the mobility of charge carriers in these systems. The development has been driven mainly by chemical derivatisation. The recent rising star of polymer materials that has experienced an unprecedented amount of attention in the polymer electronics community is the class of co-polymers based on diketopyrrolopyrrole (DPP) [120, 121]. The DPP-based approach has been the result of the co-polymerisation of electron-rich and electron-poor monomers in order to obtain low band-gap donor-acceptor conjugated polymers. The DPP acceptor core is often used in conjunction with two thiophene donor cores resulting in a D-A-D triad building block. This building block has been co-polymerised with a vast assortment of donor and acceptor co-monomers resulting in a large library of polymer semiconductors.

Conjugated polymers bear flexible alkyl sidechains in order to render them soluble in common (organic) solvents, a prerequisite for their solution-processability. Different linear and branched sidechain motifs are used and are by themselves of critical importance for the resulting molecular packing, film morphology and thus device performance [122, 97, 98, 123]. Branched sidechains are believed to be more disruptive to intermolecular $\pi - \pi$ stacking because of steric hindrance between neighbouring sidechains by virtue of the unavoidable out-of-plane bending of the chains

at the sp^3 hybridized branching point. Possible solutions to this problem invoke moving the branching point away from the main backbone [97] or the use of linear sidechains. Linear sidechains can however jeopardize solubility, particularly for polymers with a strong tendency to aggregate like DPP containing polymers. In DPP-based co-polymers branched sidechains are generally attached to the DPP unit to ensure solubility. Here we explore a route to soluble DPP-based polymer semiconductors with linear sidechains by co-polymerising with an electron poor benzotriazole co-monomer that bears a linear sidechain by itself as well, thus increasing the density of sidechains on the repeat unit. We directly compare transistor performance of the polymer with linear sidechains (abbreviated *l*-PDPPBTz) with the parent polymer that exhibits the usual branched sidechains on the DPP core (*b*-PDPPBTz) and correlate the electrical characteristics with thin film morphology. Superior balanced ambipolar transport and film morphology is observed for the *l*-PDPPBTz derivative, demonstrating that the inclusion of a co-monomer that bears sidechains by itself is a promising synthetic way forward in order to obtain soluble DPP-based donor-acceptor co-polymers bearing linear sidechains, resulting in improved charge transport properties.

A.2 Results and Discussion

A.2.1 Design and Synthesis

An attractive approach to obtaining high performance, low bandgap ambipolar polymers has been the co-polymerisation of the DPP unit with an electron poor co-polymer. For example, co-polymerisation of DPP with the strongly electron accepting benzothiadiazole (BT) [105, 124] or benzobisthiadiazole (BBT) [125] has led to polymers with mobilities of around 1 cm^2/Vs for both holes and electrons. However the strong acceptors utilised in both cases do not carry solubilising groups and therefore long and branched alkyl chains need to be included on the DPP unit. Benzotriazole (BTz) is an attractive alternative acceptor because it is possible to alkylate the N in the 2-position to provide additional solubility, thus potentially allowing the use of straight alkyl chains on the DPP unit itself. Although benzotriazole is less electron accepting than either BT or BBT, the additional solubility prompted us to investigate the properties of the DPP-BTz co-polymers. Despite the plethora of interest in DPP containing polymers, to the best of our knowledge this is the first report of such polymers. It should be noted that BTz co-polymers have demonstrated promising performance as low band-gap polymers for a number of applications such as organic photovoltaic cells [126] and electrochromics [127].

Our approach to the DPP-BTz co-polymers is based upon the recently reported direct C-H arylation approach using phosphine free conditions described by Scherf and co-workers [128]. The direct arylation method facilitates the synthesis since organometallic coupling groups do not need to be introduced onto the DPP or BTz monomers [129, 130]. Thus, as shown in Fig. A.1, the thiophene containing DPP monomer bearing either linear or branched alkyl sidechains was directly reacted with 4,7-dibromo-2-octyl-2,1,3-benzotriazole in the presence of palladium

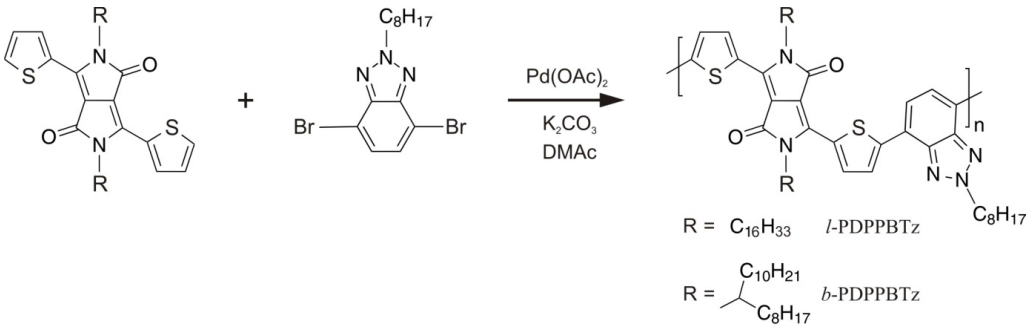

Figure A.1: Synthesis by direct arylation and molecular structures of the polymer semiconductors *l*-PDPPBTz and *b*-PDPPBTz.

acetate and potassium carbonate for 72 h. Following purification by solvent extraction and preparative GPC, the two polymers were isolated in yields of ≈ 40%. Both polymers were soluble in chlorinated solvents like chlorobenzene and chloroform, although the branched polymer was noticeably more soluble. The molecular weights of both polymers, as measured by GPC against polystyrene standards, were high with number average (Mn) values and polydispersities of 92,500 (1.5) and 27,600 (2) g/mol for *b*-DPPBTz and *l*-DPPBTz, respectively. These values are significantly higher than those of You *et al.* [130], who also reported similar direct arylation polymerisation of DPP containing monomers but with different catalyst/solvent combinations. We believe the higher molecular weight of the branched polymer may have been related to the improved solubility of the polymer in the reaction solvent compared to the linear polymer. Premature precipitation of the growing polymer chains would inhibit further polymerisation and reduce the molecular weight.

A.3 Properties

The UV-Vis absorption of chlorobenzene solutions and spun-cast thin films are shown in Fig. A.2. Both polymers exhibit a vibronic progression with a characteristic double peak absorption seen for many DPP polymers [105], with *l*-PDPPBTz exhibiting a λ_{max} at 778 nm with a shoulder at 852 nm in solution. Upon film formation the spectrum broadens slightly but the peak positions are unchanged. The branched chain polymer exhibits a λ_{max} at 837 nm with a shoulder around 780 nm. Again both the film and solution spectra are very similar. Typically for DPP polymers the double peak structure is associated with aggregation in solution or the solid state, which suggests that the incorporation of the branched alkyl group is not significantly hindering aggregation compared to the linear sidechain. In both cases the polymers appear to be aggregated already in solution at room temperature, and this aggregation is maintained during film formation.

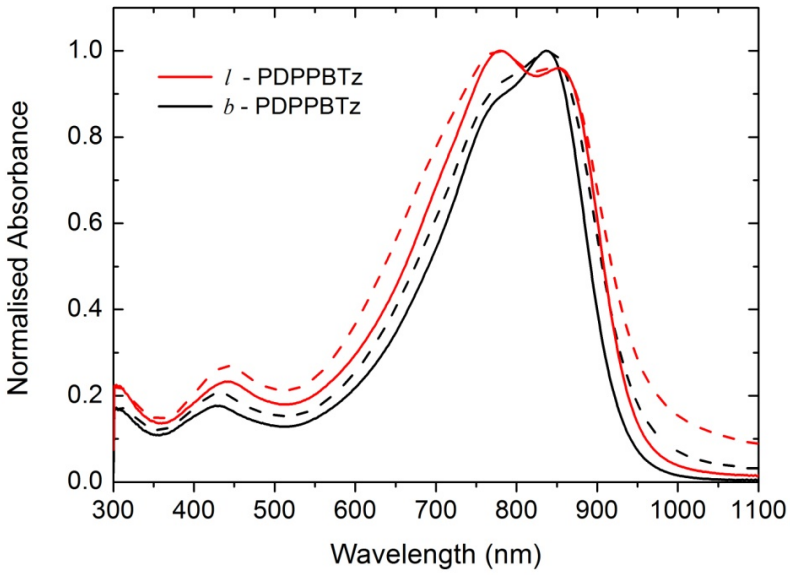

Figure A.2: UV/Vis absorption spectra of *l*-PDPPBTz (red) and *b*-PDPPBTz (black), as measured in chlorobenzene (solid lines) and as spin-cast thin films (dashed lines). Measurements courtesy of Auke Jisk Kronemeijer.

A.4 Film Microstructure

The 2D GIWAXS patterns of annealed films of *b*-PDPPBTz and *l*-PDPPBTz are presented in Fig. A.3. The scattering pattern of *b*-PDPPBTz is essentially featureless indicating a lack of long-range periodic order - the ring at $q \approx 0.38$ Å^{-1} is due to scattering from a Kapton window used in the experiment. In contrast, films of *l*-PDPPBTz exhibit a series of (h00) scattering peaks oriented along q_z corresponding to edge-on orientated lamella. The (100) peak is located at $q_z \approx 0.27$ Å^{-1} corresponding to a lamellar stacking distance of ≈ 2.3 nm. A faint (010) stacking peak is observed at $q_{xy} \approx 1.75$ Å^{-1} as well, corresponding to a $\pi - \pi$ stacking distance of ~ 3.6 Å^{-1}. The *l*-PDPPBTz with linear sidechains on the DPP core is quite obviously more ordered in thin films. The pronounced difference in morphology between films of *b*-PDPPBTz and *l*-PDPPBTz presumably stems from the (in)compatibility between the linear and branched sidechains of the DPP core with the linear C_8H_{17} sidechain of the benzotriazole co-monomer.

A.4.1 Ambipolar polymers

Fig. A.4 A and Fig. A.4 B show representative transfer characteristics of bottom-contact top-gate transistors fabricated with *l*-PDPPBTz and *b*-PDPPBTz. The transistors used gold source and drain electrodes and the dielectric used was 300 nm PMMA. Ambipolar transport with balanced hole and electron mobilities is observed for both polymer semiconductors. The extracted hole and electron mobilities as a function of annealing temperature are shown in Fig. A.4 C. The highest mobilities were achieved when the active layer was annealed at 300 °C for two

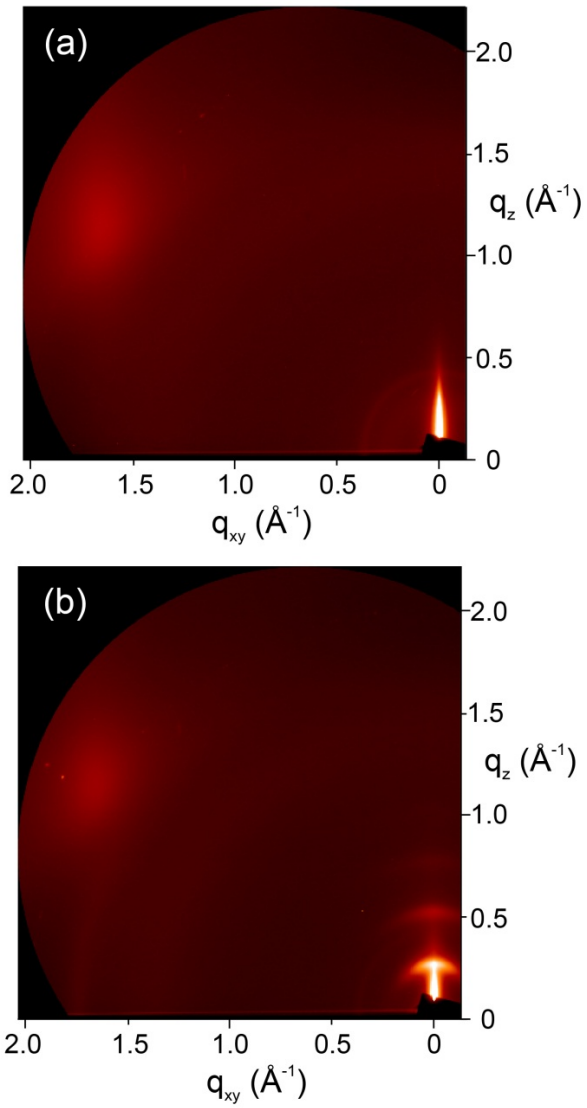

Figure A.3: 2D GIWAXS patterns of (a) *b*-PDPPBTz and (b) *l*-PDPPBTz films annealed at 200 °C. Measurements courtesy of Chris McNeill, Monash University.

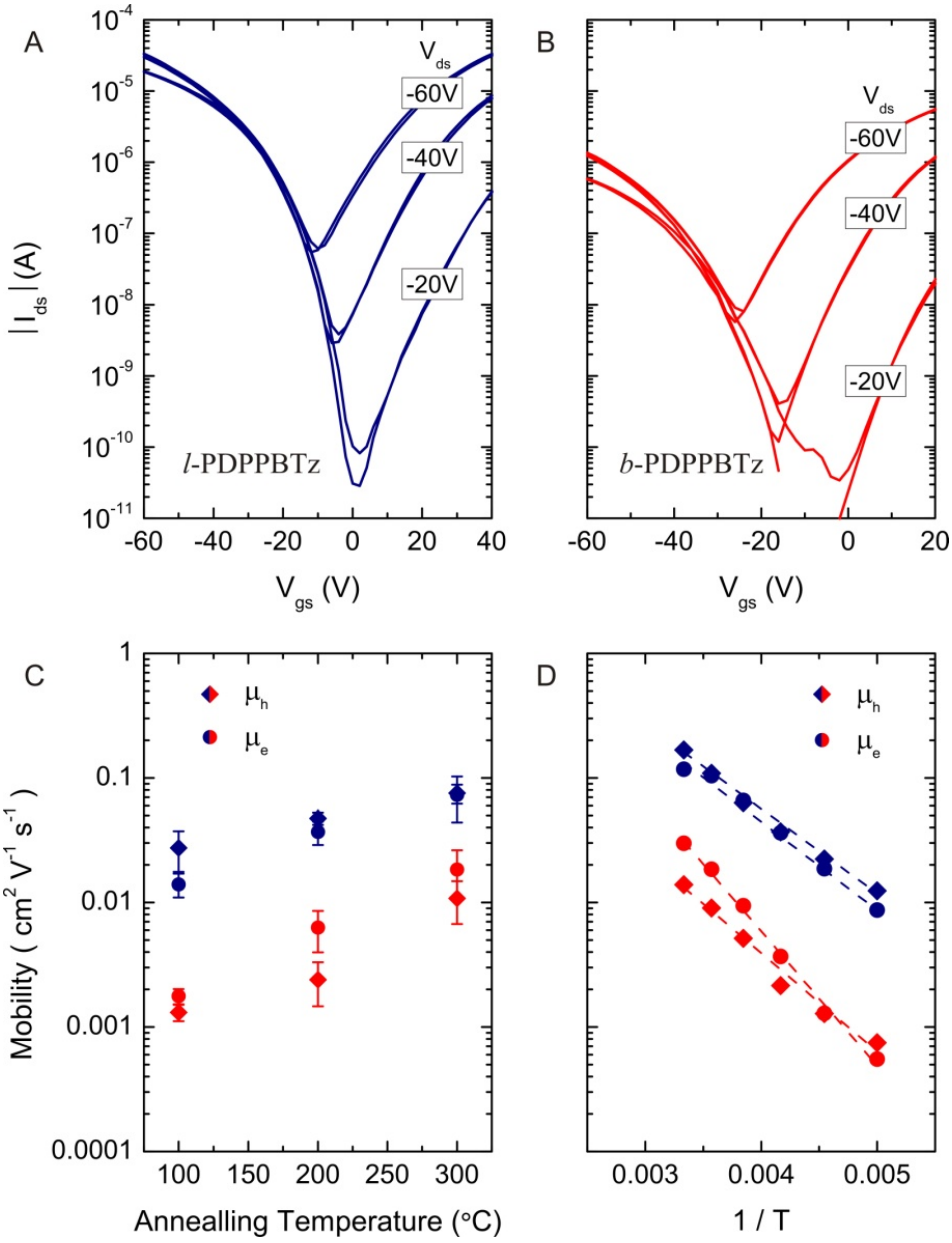

Figure A.4: (A), (B) Transfer characteristic of *l*-PDPPBTz and *b*-PDPPBTz ambipolar transistors, L = 20 μm, W = 1000 μm. (C) Extracted saturation hole and electron mobilities from the transfer characteristics as a function of annealing temperature of the polymer thin films. (D) Temperature-dependence of the extracted mobilities of *l*-PDPPBTz and *b*-PDPPBTz after 300 °C annealing as a function of 1/T.

hours during the fabrication of the transistor. Both polymers show a similar trend with higher annealing temperatures resulting in higher field-effect mobilities. The field-effect mobilities of both electrons and holes in *l*-PDPPBTz are higher than those in *b*-PDPPBTz. This is due to a higher ordering in the film as previously evidenced by GIWAXS. The extracted maximum values of the electron mobilities (after 300 °C annealing) amount to 0.074 cm^2/Vs for *l*-PDPPBTz and 0.015 cm^2/Vs for *b*-PDPPBTz. The maximum hole mobility for *l*-PDPPBTz is roughly the same as the electron mobility, while the maximum hole mobility of *b*-PDPPBTz is $\sim$ 0.01 cm^2/Vs.

Temperature dependent measurements were performed on transistors annealed at 300 °C. Fig. A.4 D shows the dependence of the extracted mobilities as a function of temperature. The carrier mobilities are Arrhenius activated as demonstrated by the linear dependence on a 1/T scale. Activation energies for hole and electrons respectively are 135 meV and 141 meV for *l*-PDPPBTz, while for *b*-PDPPBTz the corresponding values are 157 meV and 214 meV. These values of the activation energies are considerably high and suggest the presence of substantial energetic disorder, although an amorphous phase may not be entirely responsible for this [92]. Differences between electron and hole activation observed for *b*-PDPPBTz have been also observed in the selenophene based DPP polymer with branched sidechains [105], whose Seebeck coefficient was measured in Chap. 5.

The transistor measurements demonstrate that the linear sidechain variant *l*-PDPPBTz performs better with respect to carrier mobility. It should be noted that although the mobilities are higher, symmetry in the threshold voltages is better for *b*-PDPPBTz. The determined carrier mobilities are consistent with the GIWAXS data revealing the microstructure of the films. Thin films of *l*-PDPPBTz are more ordered showing both lamellar and $\pi - \pi$ stacking in contrast to *b*-PDPPBTz. This results in better orbital overlap between polymer chains and more easy charge transport. The activation energies measured are also consistent with this difference in film morphology. Higher activation is expected for more disordered semiconductors, which explains the observed 157 and 214 meV activation observed for *b*-PDPPBTz. For the more ordered *l*-PDPPBTz however, the activation energies are still quite high. This indicates that still a significant fraction of the films are amorphous, leading to bottlenecks for charge transport that need to be overcome. It is not unreasonable to assume these bottlenecks have relatively similar activation as observed for the more amorphous *b*-PDPPBTz. The film morphologies observed by simple spincoating and annealing open up the opportunity to increase the performance of *l*-PDPPBTz by more elaborate processing techniques resulting in increased order in the films. Morphology is a key parameter for the mobility and activation energy of polymer semiconductors. The current results show that for simple processing techniques multiple linear sidechains can be superior from both points of view, indicating that in the DPP-based polymer semiconductors the introduction of linear sidechains on the co-monomers is a promising advance towards ordered thin films from soluble polymer semiconductors.

A.5 Summary

We prepared two low band-gap DPP co-polymers by direct arylation polymerisation with a co-monomer that also contains a solubilising sidechain. The resultant improvement in solubility for both co-polymers allows the introduction of a straight linear sidechain on the DPP, as well as the more usual branched alkyl chain. The polymer with a linear sidechain, *l*-PDPPBTz, showed a more ordered microstructure in contrast to the largely amorphous corresponding branched sidechain co-polymer, *b*-PDPPBTz, which is commonly used in DPP-based semiconductors. The order in the microstructure was reflected in the charge transport properties of the *l*-PDPPBTz co-polymer where balanced ambipolar transport in field-effect transistors was observed with maximum hole and electron mobilities of 0.074 cm^2/Vs, compared to and 0.015 cm^2/Vs for *b*-PDPPBTz. The difference in morphology was observed in the activation energies of charge transport as well, although the high activation of *l*-PDPPBTz still indicated a large fraction of amorphous phase in the thin films. We have shown that introducing multiple linear side chains in this class of polymer semiconductors is a promising way forward towards ordered thin films from soluble polymer semiconductors containing only linear sidechains. The demonstrated synthetic strategy can be applied to new donor-acceptor co-polymers as a means to improve performance.

Appendix B

Simple Modelling of the trends seen in the Seebeck coefficient

B.1 Seebeck within a parabolic density of states (DOS)

If the density of states N is assumed to be parabolic and has the usual $T^{3/2}$ dependence given by $N = \left(\frac{2\pi m^* k_B T}{h^2}\right)^{3/2}$, one can use the equation $\alpha = k_B/e\left[\ln(N/n) + A\right]$ with this parabolic density of states to estimate the Seebeck coefficient. Fig. B.1 shows the results of such a calculation with different values of effective mass m^*. Where the heat of transport constant A is not mentioned on the plot, we've chosen $A = 0$. What is clear from this plot is that the absolute magnitude of the Seebeck coefficient in IDTBT starts to agree with the magnitude of the measured Seebeck coefficient within a parabolic density of states only when $m^* = 10\ m_e$, and for $A = 2$. $A =$ 1 - 2 is normally seen in semiconductors like silicon. We do not intend to use this result to estimate the value of m^* in IDTBT, but this simple calculation shows that in this band-like model one would need a high effective mass in order to explain the magnitude of the Seebeck coefficient. The temperature variation of the Seebeck in this picture goes as a function of $\ln(T)$. The temperature dependence of the Seebeck is thus very weak, and the trend if any, would unfortunately be buried within the error of our measurement.

B.2 The chemical potential for n_c carriers in an energy band of width W

With electrons injected into a conduction band the chemical potential is often envisioned as lying within it. However, this picture relies on the width of the energy band being very much greater than the thermal energy $k_B T$. For narrower energy bands the chemical potential usually resides outside of the energy band. Here we present a simple calculation to illustrate this point. The chemical potential for n_c fermions added to an N-state band of width W is found from

$$n_c = \int_{-W/2}^{W/2} dE \frac{g(E)}{\exp\left[(E-\mu)/k_B T + 1\right]} \tag{B.1}$$

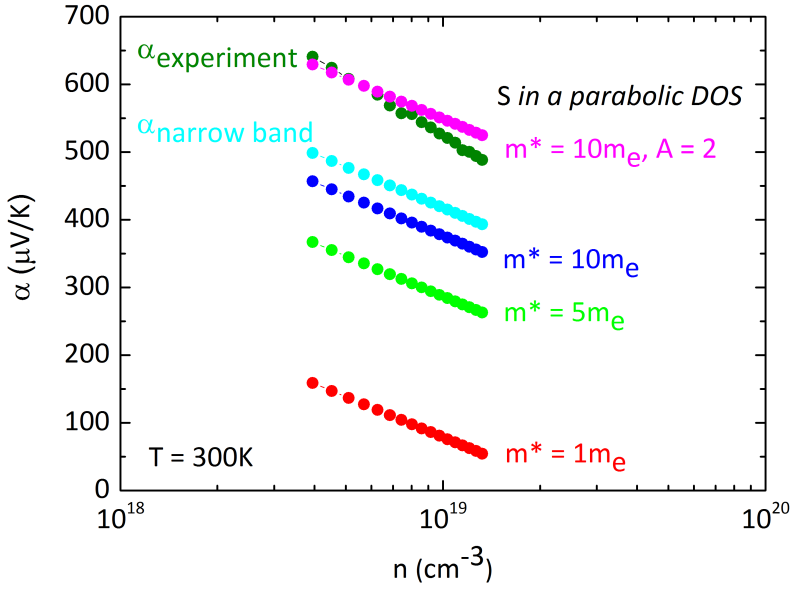

Figure B.1: Seebeck coefficient versus carrier concentration in a parabolic DOS as a function of different effective masses.

where $g(E)$ denotes the density-of-states. Consider for simplicity the "square-band" $g(E) = N/W$ and ignore spin degeneracy. The integration is readily performed to yield

$$n_c = N\frac{k_B T}{W}\ln\left[\frac{\exp\left(W/2+\mu\right)/k_B T+1}{\exp\left(-W/2+\mu\right)/k_B T+1}\right] \tag{B.2}$$

Upon solving this equation for the chemical potential we find:

$$\mu = k_B T \ln\left(\frac{1-\exp(cW/k_B T)}{\exp(-W/2k_B T)\exp(cW/k_B T)-\exp(W/2k_B T)}\right) \tag{B.3}$$

where $c \equiv n_c/N$. In Fig. B.2, $\mu/k_B T$ is plotted against $W/k_B T$ for different values of c between 0.001 and 0.9, where the dashed lines indicate the upper and lower edges of the energy band. In the wide-band limit, $W/k_B T \to \infty$:

$$\mu \to W\left(c-\frac{1}{2}\right) \tag{B.4}$$

In this limit the chemical potential is pinned within the energy band. The chemical potential then delineates states within the energy band that are occupied from states that are unoccupied. The domain of the wide-band limit generally increases as the carrier concentration c approaches 0.5. A qualitatively different situation prevails in the narrow-band limit, $W/k_B T \to 0$:

$$\mu \to k_B T \ln\left(\frac{c}{1-c}\right) \tag{B.5}$$

In this regime the chemical potential usually lies outside of the energy band. Furthermore the chemical potential moves farther from the energy band as the temperature is raised. The domain of the narrow-band limit increases as the carrier concentration c departs from 0.5. The Seebeck

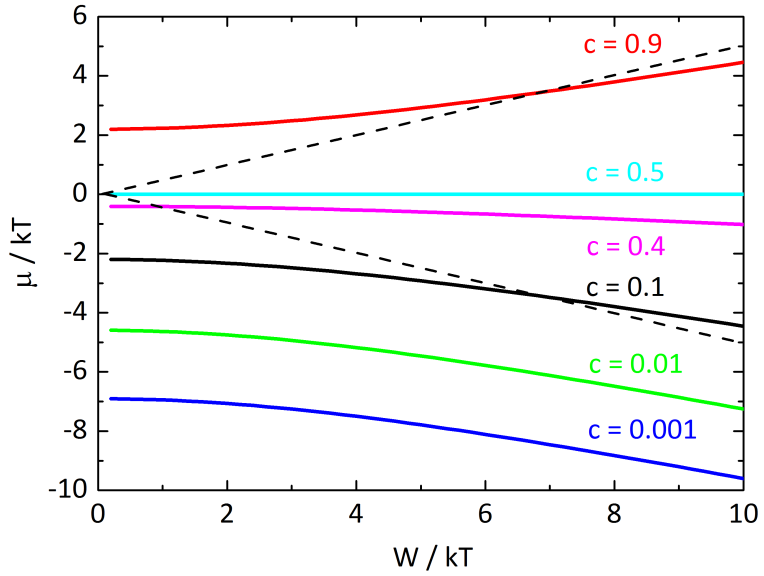

Figure B.2: μ/k_BT plotted against W/k_BT for different values of c. The dashed lines indicate the top ($W/2$) and the bottom ($-W/2$) of the energy band.

coefficient for this model is just the entropy change ΔS associated with increasing the carrier number from N_c to $N_c + 1$ divided by the carrier's charge e:

$$\alpha = \frac{\Delta S}{e} = \frac{1}{e}\frac{d}{dN_c}\left(\frac{U - \mu N_c}{T}\right) = \frac{k_B}{e}\left(\frac{E-\mu}{k_BT}\right) \tag{B.6}$$

where U represents the internal energy and $E = dU/dN_c$. In the narrow-band limit the Seebeck coefficient becomes:

$$\alpha = \frac{k_B}{e}\ln\left(\frac{1-c}{c}\right) \tag{B.7}$$

B.3 Trap DOS within a few k_BT from the center of a narrow band DOS

To illustrate the effect of trapping of charge carriers, we model the band in the organic semiconductor as a Gaussian DOS of width $\sigma = 20$ meV;

$$\text{GDOS} = \frac{N}{\sqrt{2\pi\sigma^2}}\exp\left(-\frac{E^2}{2\pi\sigma^2}\right) \tag{B.8}$$

shown in Fig. B.3. We model a Gaussian trap DOS with a width $\sigma_t = 10$ meV close to the center of the primary GDOS band, but shifted in energy by $\Delta = 20$ meV, 30 meV, 40 meV and 50 meV.

$$\text{trap DOS} = \frac{N_t}{\sqrt{2\pi{\sigma_t}^2}}\exp\left(-\frac{(E+\Delta)^2}{2\pi{\sigma_t}^2}\right) \tag{B.9}$$

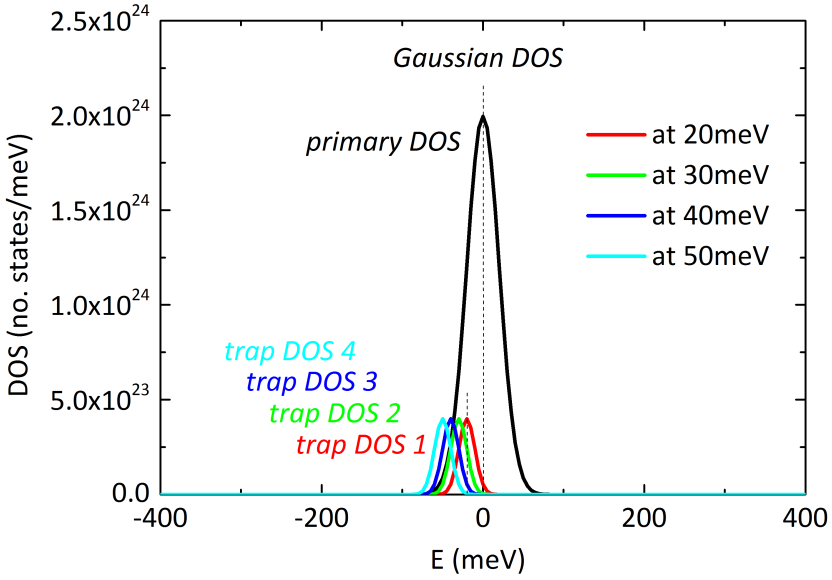

Figure B.3: A primary Gaussian DOS of width 20 meV modeled together with a trap DOS of width 10 meV shifted from the center of the primary DOS by different energies.

To estimate the number of charges that enter the trap DOS and hence cause an increase in the Seebeck coefficient, we first numerically estimate the position of the chemical potential μ using

$$n = \int (\text{GDOS} + \text{trap DOS}) \times \text{FD}(E, \mu) dE \tag{B.10}$$

n is known from a measurement of device capacitance. FD is the Fermi-Dirac distribution. On knowing μ, the number of charges that end up in the trap DOS is given by

$$n_{\text{trap}} = \int (\text{trap DOS}) \times \text{FD}(E, \mu) dE, \tag{B.11}$$

while the fraction of charges that are not trapped and end up in the primary Gaussian DOS is given by

$$n_{\text{DOS}} = \int (\text{GDOS}) \times \text{FD}(E, \mu) dE \tag{B.12}$$

Fig. B.4 shows the fraction of charges that are trapped in the secondary trap DOS. As long as the trap DOS is centered sufficiently close to the center of the main band, i.e., within within 30 - 40 meV at room temperature, the ratio of n_{trap}/n does not vary much with gate voltage. This provides a justification for considering the factor f as independent of gate voltage across the range of applied gate voltages.

Fig. B.5 shows two Gaussian trap DOS with the same width centered at 20 meV from the center of the primary Gaussian DOS. Trap DOS 2 has twice the number of states compared with Trap DOS 1. Fig. B.6 shows the ratio of the number of carriers lost to traps to those that enter the primary Gaussian DOS. When the number of trap states is doubled in the case of trap DOS 2, the number of carriers that are trapped increases. As shown in the main text, the

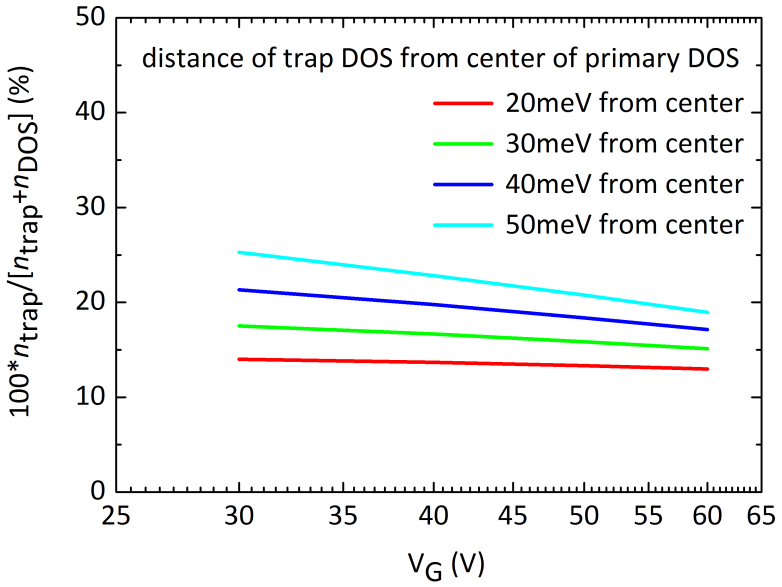

Figure B.4: Fraction of carriers that are trapped in a Gaussian trap DOS close to the center of a primary Gaussian DOS band ($N = 10^{26}$ cm^{-3}, $N_t = 10^{25}$ cm^{-3}).

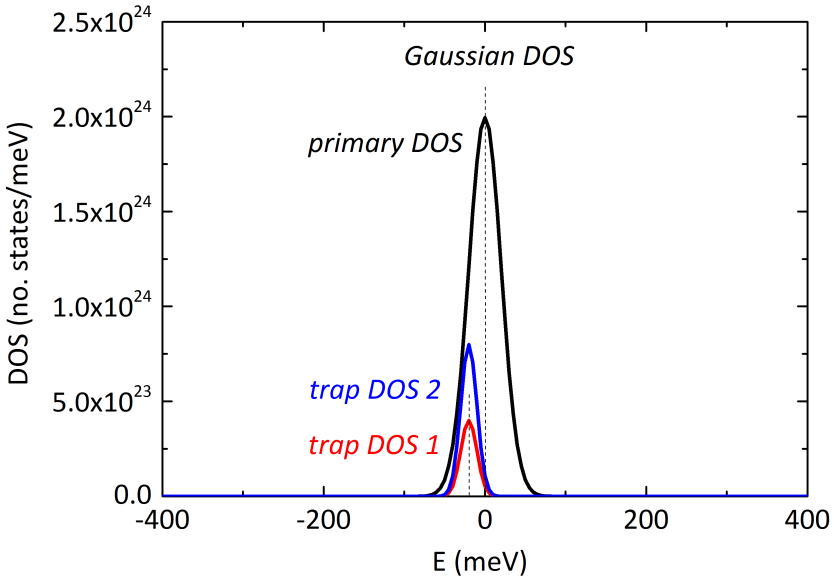

Figure B.5: Two different trap DOS, one with twice the number of trap states, located at 20 meV from the center of the Gaussian band DOS.

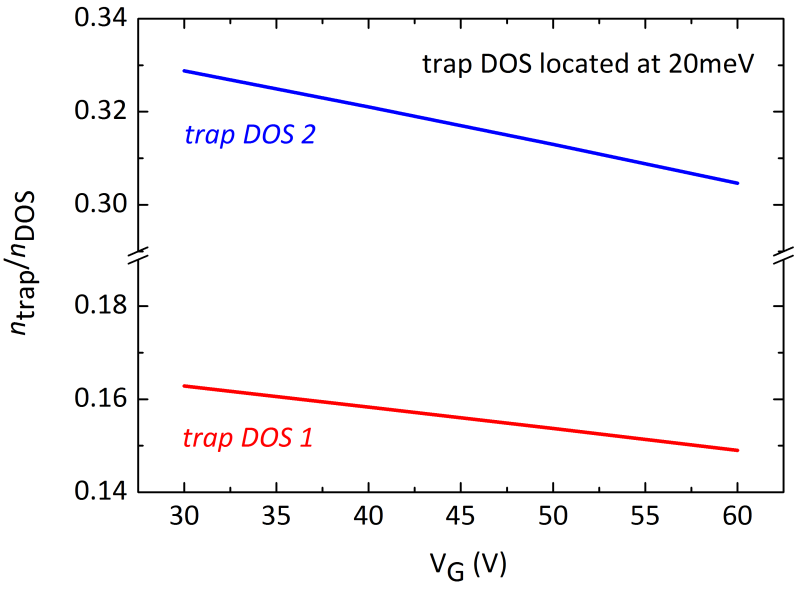

Figure B.6: $n_{\text{trap}}/n_{\text{DOS}}$ for two different trap density of states, trap DOS 2 > trap DOS 1.

magnitude of the slope of the Seebeck coefficient $\propto [1 - n_{\text{trap}}/n]^{-1}$, n being the total number of gate induced charges. From the two different slopes in Fig. B.6, it can be readily deduced that a greater trap DOS within (or close to) the main band, causes both an increase in magnitude of the Seebeck coefficient as well as an increase in the slope of the Seebeck coefficient with gate voltage.

Appendix C

Facilities Development

In the early stages of the work done for this PhD thesis, it was my personal goal to improve the way low temperature measurements on organic semiconductors were done in the Optoelectronics group. One of the ways in which this was achieved was to perform measurements with a specially designed insert that does away with any form of wire bonding or silver dagging. Shown in Fig. C.1 (a) is the insert that was built specially for use with a 10 Tesla magnet field Oxford Instruments Cryostat. It is nothing but a stick that connects the chip at the bottom to a breakout box at the top via a vacuum Fischer connector. Fig. C.1 (b) shows the break out box at the top of the insert. It contains three triax connectors that can be directly wired to an Agilent 4155B SPA. The triax connectors contact the transverse probes on the Hall device so as to use the SPA's high input impedance source-measure units to probe the Hall voltage when such a measurement is being done. The other connectors contact the other components on the chip. Fig. C.2 shows the bottom of the stick that houses the device. The device is placed in the groove shown and the placeholder is screwed onto the head that contains Au plated spring loaded contacts. Contact is seamlessly made via a physical contact between the spring loaded pins and the large contact pads on the chip. This insert was proven successful when used in the doctoral work of Dr. Gueorgui Nikiforov who made use of it to probe channel heating effects in organic semiconductors at cryogenic temperatures. One can have any electronic architecture on the chip as long as the components are wired to up to 13 large 2×2 mm^2 contact pads positioned in a specific geometry to make contact with the spring loaded pins. Fig. C.3 is a picture of a typical fully fabricated Seebeck device using the photomask pattern illustrated earlier. The recognisable large contact pads on the chip make this device compatible with the designed insert. Although all the Seebeck measurements of this thesis were performed in a Lakeshore low temperature probe station, the possibility exists for performing magneto-Seebeck measurements in the future using this insert.

As a quick illustration for the use of the insert with spring loaded contacts, the Hall effect was measured in a solution processed oxide with a high-k polymer dielectric ($\epsilon_r = 40$). The architecture of the Hall bar was the same as that shown in Fig. 2.13 (a). The oxide was a derivative of InZnO and was spin coated on a chip with patterned electrodes by Dr. K. K. Banger

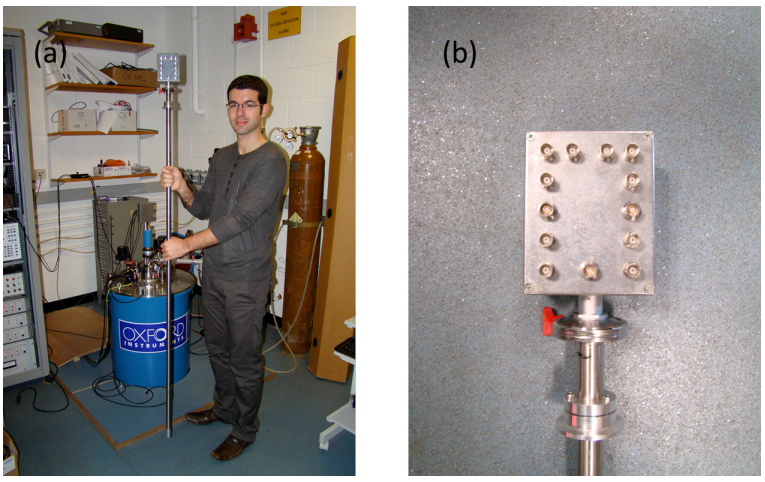

Figure C.1: (a) The Oxford instruments cryostat compatible insert with spring loaded connector pins built for low temperature Hall and Seebeck measurements (b) The breakout box at the head of the insert with biaxial and triaxial connectors. The position of the pins on the face of the box resembles the position of the contact pads on the device.

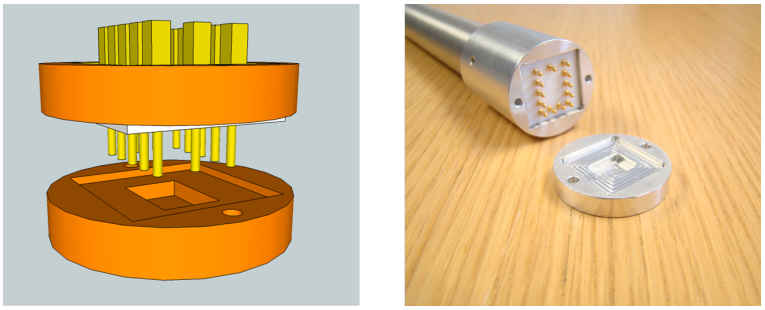

Figure C.2: Schematic and actual picture of the bottom end of the insert with Au coated spring loaded contact pins. The device sits in the groove of the bottom plate that is screwed onto the head till a point where the spring loaded contact pins make contact with the device. This design does away with the need for bonding or silver dagging.

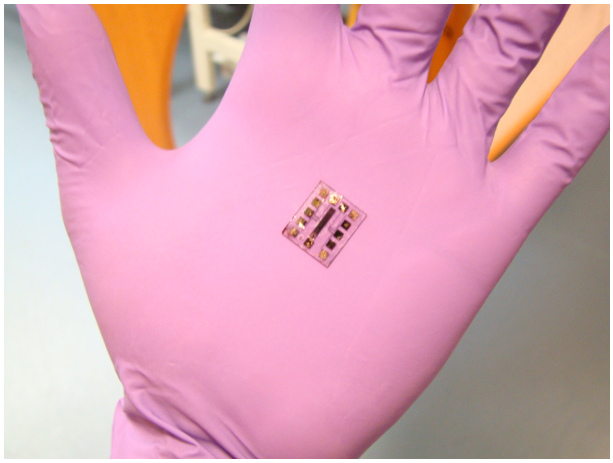

Figure C.3: An image of a fully fabricated functional Seebeck device based on an organic semiconductor.

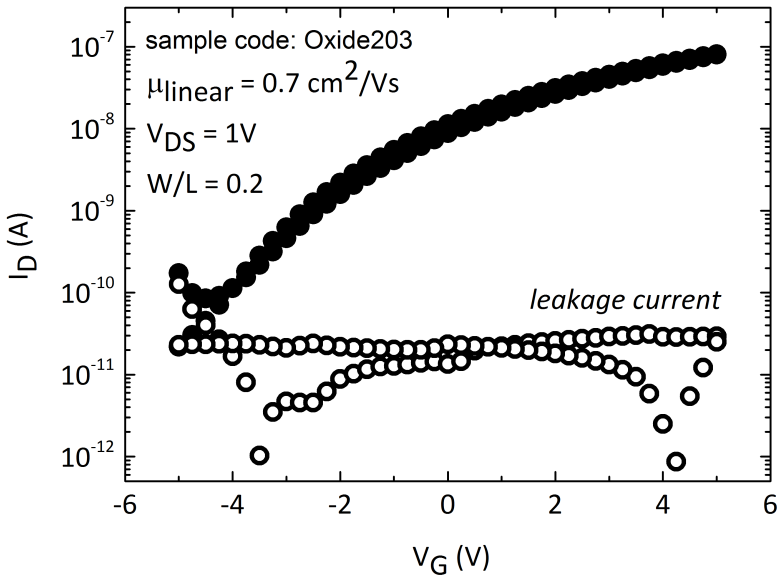

Figure C.4: Transfer characteristics of an amorphous oxide based on doped InZnO gated with a proprietary organic high-k dielectric having a dielectric constant $\epsilon_r = 40$ at low gate voltage. The field effect mobility is 0.7 cm^2/Vs at $V_{DS} = 2$ V. The low device gate leakage current is down to having a patterned oxide.

of the Optoelectronics Group. The Hall bar pattern of Fig. 2.13 (b) was etched into the oxide using a wet chemical etch. A 200 nm polymer dielectric layer was then solution-processed over the patterned oxide and a gate electrode with a 1.5 mm width was evaporated over the polymer dielectric layer. Fig. C.4 shows the linear transfer characteristics of this hybrid oxide-polymer FET. The linear field-effect mobility was around 0.7 cm^2/Vs.

Fig. C.5 shows the measured Hall voltage in this device at 300 K. As the magnetic field B was swept from 0 to 7 T, the hall voltage builds up gradually, following the trace of the applied magnetic field. Fig. C.6 shows a few points in the gate voltage modulated Hall mobility. It is of significance to note that the Hall and field-effect mobilities of this device at high magnetic fields are the same at 300 K.

The physics of solution processed oxide semiconductors shall not be dived into here. This section is only meant to show that the design of the insert and the Hall device was successful and harbours potential. I would be very glad if an interested party puts it to good use in the near future.

In addition, since time was also invested in writing control programs using LabVIEW to program the Semiconductor Parameter Analyser to perform required measurements, I have included the frontend panel of two programs here. The first, "Thermopower-Sampling.vi" measures the thermal voltage as a function of heater power on-chip and the second "Hall-Voltage-Sampling.vi" measures the Hall voltage. The two other regularly used programs "Sensor-Resistance-Sampling.vi" and "Pt-Thermometer-IVcurves.vi" are not shown here for brevity.

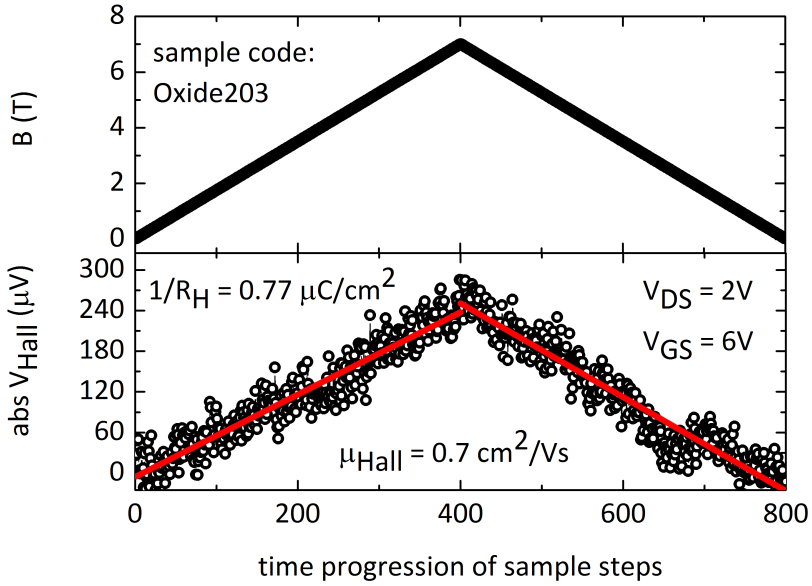

Figure C.5: The measured Hall voltage on the oxide-polymer hybrid FET. The Hall voltage, shown here in absolute value, follows the trace in the perpendicular applied magnetic field.

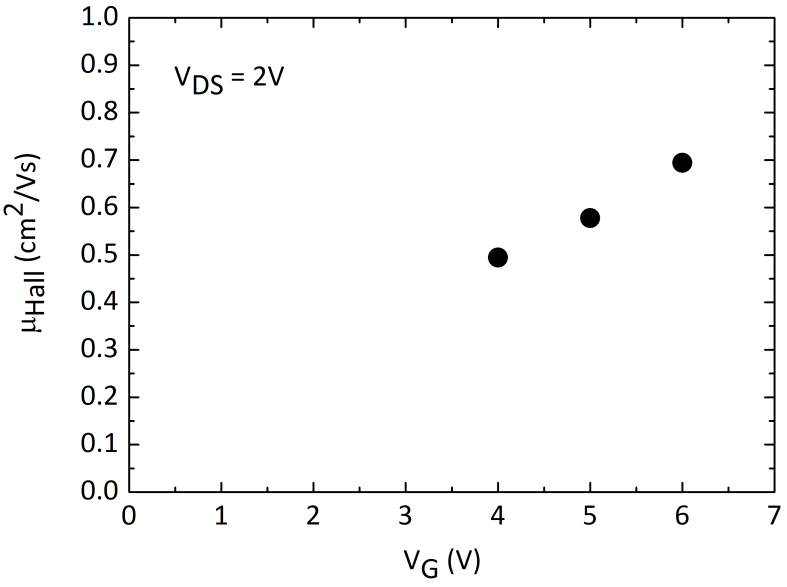

Figure C.6: Gate voltage modulated Hall voltage in the hybrid FET.

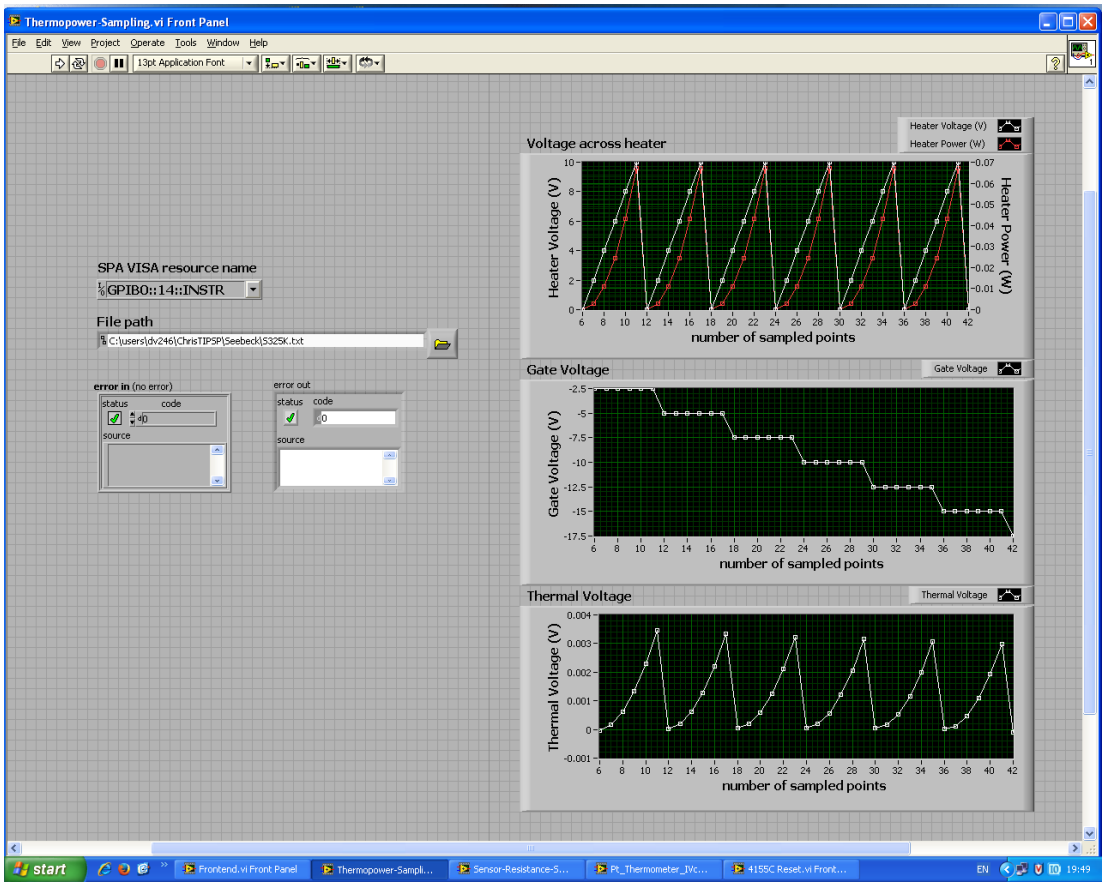

Figure C.7: Thermopower-Sampling.vi; This program is used to measure the thermal voltage across the organic semiconductor on the chip. The top panel shows the voltage applied across the heater and the power dissipated by the heater on chip. The middle panel shows the applied gate voltage and the lower panel shows the measured thermal voltage. The gate voltage steps and the heater voltage steps are all set directly on the rear panel of the LabVIEW program. The measurement is done in the sampling mode.

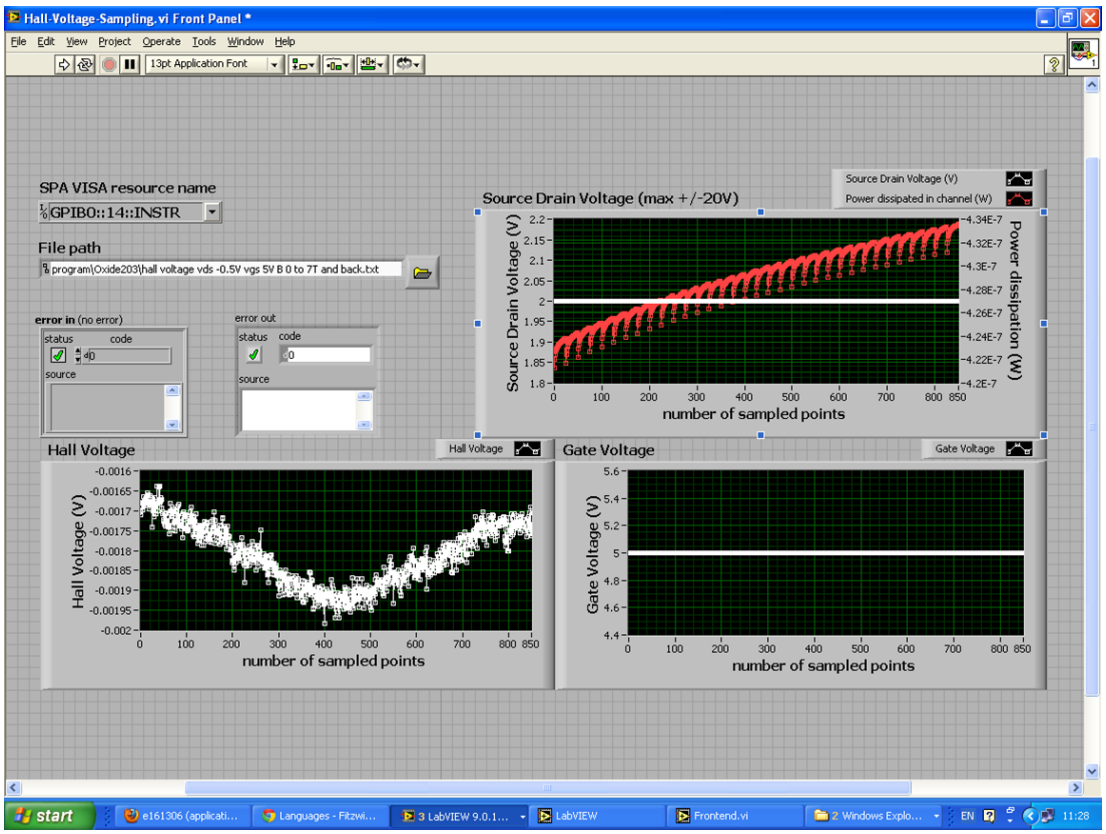

Figure C.8: Hall-Voltage-Sampling.vi; This program is used to measure the Hall voltage that develops across a semiconducting bar in the presence of an applied gate voltage, source drain voltage and an applied magnetic field. The magnetic field is not set from this program, but is set/swept manually. The Hall voltage measured here is a function of a ramp in the magnetic field. The red trace shows the power dissipated between the source and drain electrodes. It registers spikes owing to the nature of the sampling type of measurement employed. It also shows a drift over time. The magnitude of the power dissipation is however not substantial. All parameters are set on the rear end of the program.

Appendix D

Mathematica Programs

Two programs using *Mathematica* were coded to solve (a) Eq. 3.4 to estimate the chemical potential μ_C within an exponential DOS, knowing the carrier concentration n within the FET channel and (b) Eq. 3.9 to estimate the position of the transport energy E^* within the DOS. These two quantities were needed to compute the theoretical estmate of the Seebeck coefficient in Chap. 3. Outlined below are the two codes.

D.1 Code to extract μ_C within an exponential DOS

```
Clear[EDOS, FD, h, efermi];
        (* Clear all variables before running the program *)
T0 = 750;
        (* Width of the Exponential DOS in K *)
k = 1.38*10^-23;
        (* Boltzmann constant in J/K*)
T = 300;
        (* Temperature in K*)
Cdiel = 8.85*10^-12*3.5/(300*10^-9);
        (* Dielectric capacitance of 300 nm PMMA per unit area *)
CarrierConc = (Cdiel/(2*10^-9))/(1.6*10^-19);
        (* volumetric carrier concentration in a 2 nm thick channel in m^-3*)

EDOS[x_] = (10^26/( 1000*k*T0/(1.6*10^-19)))*Exp[x/(1000*k*T0/(1.6*10^-19))];
        (* Exponential DOS in the polymer with 10^26 available states *)

FD [x_, efermi_] = 1/(1 + Exp[(x - efermi)/(1000*k*T/(1.6*10^-19))]);
        (* Fermi Dirac distribution function with energies in meV *)

h[efermi_?NumericQ] := NIntegrate[EDOS[x]* FD[x, efermi], {x, -1000, 1000}]
        (* Solve for the Fermi Energy efermi using Numerical integration *)

sol = FindRoot[h[efermi] == CarrierConc*20, {efermi, -100}]
```

```
sol = FindRoot[h[efermi] == CarrierConc*30, {efermi, -100}]
sol = FindRoot[h[efermi] == CarrierConc*40, {efermi, -100}]
sol = FindRoot[h[efermi] == CarrierConc*50, {efermi, -100}]
sol = FindRoot[h[efermi] == CarrierConc*60, {efermi, -100}]
        (* chemical potentials are roots to the equations at
                        different gate voltages*)
```

Running the above code generates the following output.

```
{efermi -> -195.306}
{efermi -> -169.078}
{efermi -> -150.468}
{efermi -> -136.034}
{efermi -> -124.24}
```

All the energies are in meV. It represents the position of the chemical potential within the chosen exponential DOS at the following gate voltages; 20, 30, 40, 50 and 60 V respectively. Each of these chemical potentials are then used in the following program one by one to estimate the position of the transport energy level.

D.2 Code to extract E^* within an exponential DOS

```
Clear[efermi, shat, f];
        (* Clear all variables before running the program *)
T0 = 750;
        (* width of the exponential DOS in K *)
k = 1.38*10^-23;
        (* Boltzmann constant in J/K *)
alpha = 1/(3.2*10^-10);
        (* inverse localisation length *)
bc = 2.8;
        (* critical number of bonds to other sites *)
T = 300;
        (* Temperature in K *)

efermi = -124.24;
        (* value taken from program to find the chemical potential *)

shat = T0/T;
        (* dimensionless reduced DOS width *)

f[estar_] := ((2*alpha)/3*((3*bc)/(4 pi))^(1/3)*(10^26)^(-1/3)*
    Exp[estar/(1000*k*T0/(1.6*10^-19))])
                /(Exp[estar/(1000*k*T0/(1.6*10^-19))]
                        - Exp[efermi/(1000*k*T0/(1.6*10^-19))])^((4/3))
```

```
sol = FindRoot[f[estar] == shat, {estar, 0}]
        (* Transport energy is the solution to the transcendental equation *)
```

Running the above code generates the following output.

```
{estar -> 96.2217}
```

The transport energy E^* given by this program corresponds to only one value of the chemical potential μ_C. This program is to be run for gate voltage dependent values of μ_C at the same temperature to arrive at the variation of the transport energy with gate voltage. From μ_C and E^*, the Seebeck coefficient can be estimated.

Appendix E

Publications and Presentations

Publications

Deepak Venkateshvaran, Mark Nikolka, Aditya Sadhanala, Vincent Lemaur, Mateusz Zelazny, Michal Kepa, Michael Hurhangee, Auke Jisk Kronemeijer, Vincenzo Pecunia, Iyad Nasrallah, Igor Romanov, Iain McCulloch, David Emin, Yoann Olivier, Jerome Cornil, David Beljonne and Henning Sirringhaus. "Approaching disorder-free transport in high mobility conjugated polymers."
Manuscript submitted to Nature (2013)

Deepak Venkateshvaran, Auke Jisk Kronemeijer, John Moriarty, David Emin and Henning Sirringhaus. "Field-effect modulated Seebeck coefficient in organic polymers using a microfabricated on-chip architecture.".
APL Materials **2**, 032102 (2014)

Auke Jisk Kronemeijer, Vincenzo Pecunia, **Deepak Venkateshvaran**, Aditya Sadhanala, John Moriarty, Monika Szumilo and Henning Sirringhaus. "Two dimensional carrier distribution in top gate polymer field-effect transistors: Correlation between width of density of states and Urbach energy."
Advanced Materials **26**, 728-733 (2014)

Riccardo Di Pietro, **Deepak Venkateshvaran**, Andreas Klug, Emil J.W. List-Kratochvil, Antonio Facchetti, Henning Sirringhaus and Dieter Neher. "Simultaneous extraction of gate voltage dependent mobility and contact resistance from thin film transistors."
Applied Physics Letters **104**, 193501 (2014)

Gueorgui O. Nikiforov, **Deepak Venkateshvaran**, Sebastian Mooser, Aurelie Meneau, Thomas Strobel, Auke Jisk Kronemeijer, Mi Jung Lee and Henning Sirringhaus. "Current-induced Joule heating and electrical field effects in low temperature measurements on TIPS-pentacene thin

film transistors."
Manuscript in preparation for Physical Review B (2014)

Presentations

"**Organic Thermoelectrics**"

Nanoelectronics group (Prof. Arindam Ghosh)
Indian Institute of Science, Bangalore, **India**, March 2013

Cavendish Graduate Student Conference 2013
University of Cambridge, Cambridge, **United Kingdom**, December 2013

Molecular Electronics Group (Prof. K. S. Narayan)
Jawaharlal Nehru Center for Advanced Scientific Research, Bangalore, **India**, February 2014

Energy Materials and Surface Sciences Unit (Prof. Yabing Qi)
Okinawa Institute of Science and Technology, Okinawa, **Japan**, March 2014

Organic Semiconductor Laboratory (Prof. Changhee Lee)
Seoul National University (SNU), Seoul, **South Korea**, March 2014

Flexible Electronic Materials Laboratory (Prof. M. J. Lee)
Kookmin University, Seoul, **South Korea**, March 2014

Bibliography

[1] F. Ritz and C. E. Peterson, "Multi-mission radioisotope thermoelectric generator (MMRTG) program overview," *2004 IEEE Aerospace Conference Proceedings*, p. 2950, 2004.

[2] *Energy-Efficient Technologies for the Dismounted Soldier.* Washington D. C, U. S. A: National Academy Press, 1997.

[3] H. Zervos, *Thermoelectric Energy Harvesting 2013-2023: Devices, Applications, Opportunities.* Cambridge, United Kingdom: IDTechEx, 2013.

[4] C. J. Vineis, A. Shakouri, A. Majumdar, and M. G. Kanatzidis, "Nanostructured thermoelectrics: Big efficiency gains from small features," *Advanced Materials*, vol. 22, p. 3970, 2010.

[5] C. Kittel, *Introduction to Solid State Physics.* Hoboken, New Jersey, U. S. A: John Wiley and Sons, 2005.

[6] A. Majumdar, "Thermoelectricity in semiconductor nanostructures," *Science*, vol. 303, p. 777, 2004.

[7] R. Venkatasubramanian, E. Siivola, T. Colpitts, and B. O'Quinn, "Thin-film thermoelectric devices with high room-temperature figures of merit," *Nature*, vol. 413, p. 597, 2001.

[8] T. C. Harman, P. J. Taylor, M. P. Walsh, and B. E. LaForge, "Quantum dot superlattice thermoelectric materials and devices," *Science*, vol. 297, p. 2229, 2002.

[9] K. Biswas, J. He, I. D. Blum, C.-I. Wu, T. P. Hogan, D. N. Seidman, V. P. Dravid, and M. G. Kanatzidis, "High-performance bulk thermoelectrics with all-scale hierarchical architectures," *Nature*, vol. 489, p. 414, 2012.

[10] C. B. Vining, "An inconvenient truth about thermoelectrics," *Nature Materials*, vol. 8, p. 83, 2009.

[11] H. Liu, X. Shi, F. Xu, L. Zhang, W. Zhang, L. Chen, Q. Li, C. Uher, T. Day, and G. J. Snyder, "Copper ion liquid-like thermoelectrics," *Nature Materials*, vol. 11, p. 422, 2012.

[12] I. Chowdhury, R. Prasher, K. Lofgreen, G. Chrysler, S. Narasimhan, R. Mahajan, D. Koester, R. Alley, and R. Venkatasubramanian, "On-chip cooling by superlattice-based thin-film thermoelectrics," *Nature Nanotechnology*, vol. 4, p. 235, 2009.

[13] J.-F. Li, W.-S. Liu, L.-D. Zhao, and M. Zhou, "High-performance nanostructured thermoelectric materials," *NPG Asia Materials*, vol. 2(4), p. 152, 2010.

[14] G.-H. Kim, L. Shao, K. Zhang, and K. P. Pipe, "Engineered doping of organic semiconductors for enhanced thermoelectric efficiency," *Nature Materials*, vol. 12, p. 719, 2013.

[15] O. Bubnova, Z. U. Khan, A. Malti, S. Braun, M. Fahlman, M. Berggren, and X. Crispin, "Optimization of the thermoelectric figure of merit in the conducting polymer poly(3,4-ethylenedioxythiophene)," *Nature Materials*, vol. 10, p. 429, 2011.

[16] D. Wang, L. Tang, M. Long, and Z. Shuai, "First-principles investigation of organic semiconductors for thermoelectric applications," *The Journal of Chemical Physics*, vol. 131, p. 736, 2009.

[17] K. E. Goodson, "Ordering up the minimum thermal conductivity of solids," *Science*, vol. 315, p. 342, 2007.

[18] W. Bruetting, *Physics of Organic Semiconductors*. Weinheim, Germany: Wiley-VCH, 2005.

[19] V. Coropceanu, J. Cornil, D. A. da Silva Filho, Y. Olivier, R. Silbey, and J.-L. Brédas, "Charge transport in organic semiconductors," *Chemical Reviews*, vol. 107, p. 926, 2007.

[20] Z. Bao and J. Locklin, *Organic Field-Effect Transistors*. Boca Raton, Florida, U. S. A: CRC Press, 2007.

[21] H. Sirringhaus, T. Sakanoue, and J.-F. Chang, "Charge-transport physics of high-mobility molecular semiconductors," *Physica Status Solidi B*, vol. 249, p. 1655, 2012.

[22] H. Sirringhaus, "Device physics of solution-processed organic field-effect transistors," *Advanced Materials*, vol. 17, p. 2411, 2005.

[23] C. Albanesius, "LG unveils massive 77-inch curved OLED 4K HDTV," http://www.pcmag.com/article2/0,2817,2424086,00.asp.

[24] T. Sekitani and T. Someya, "Stretchable, large-area organic electronics," *Advanced Materials*, vol. 22, p. 2228, 2010.

[25] G. Horowitz, "Organic field-effect transistors," *Advanced Materials*, vol. 10, pp. 365–377, 1998.

[26] H. Sirringhaus, "Organic semiconductors: An equal-opportunity conductor," *Nature Materials*, vol. 2, p. 641, 2003.

[27] L. Herlogsson, "Electrolyte-gated organic thin-film transistors," Ph.D. dissertation, Linköping University, Sweden, 2011.

[28] H. Baessler, "Localized states and electronic transport in single component organic solids with diagonal disorder," *Physica Status Solidi B*, vol. 107, p. 9, 1981.

[29] H. Bässler, "Charge transport in disordered organic photoconductors," *Physica Status Solidi (b)*, vol. 175, p. 15, 1993.

[30] M. C. J. M. Vissenberg and M. Matters, "Theory of the field-effect mobility in amorphous organic transistors," *Physical Review B*, vol. 57, p. 12 964, 1998.

[31] H. Bässler, P. M. Borsenberger, and R. J. Perry, "Charge transport in poly(methylphenylsilane): The case for superimposed disorder and polaron effects," *Journal of Polymer Science, Part B: Polymer Physics*, vol. 32, p. 1677, 1994.

[32] P. E. Parris, V. M. Kenkre, and D. H. Dunlap, "Nature of charge carriers in disordered molecular solids: Are polarons compatible with observations?" *Physical Review Letters*, vol. 87, p. 126601, 2001.

[33] I. I. Fishchuk, A. Kadashchuk, H. Bässler, and S. Nešpůrek, "Nondispersive polaron transport in disordered organic solids," *Physical Review B*, vol. 67, p. 224303, 2003.

[34] J.-F. Chang, H. Sirringhaus, M. Giles, M. Heeney, and I. McCulloch, "Relative importance of polaron activation and disorder on charge transport in high-mobility conjugated polymer field-effect transistors," *Physical Review B*, vol. 76, p. 205204, 2007.

[35] Y. Y. Deng and H. Sirringhaus, "Optical absorptions of polyfluorene transistors," *Physical Review B*, vol. 72, p. 045207, 2005.

[36] T. Holstein, "Studies of Polaron Motion. Part 1: The Molecular Crystal Model," *Annals of Physics*, vol. 8, p. 325, 1959.

[37] ——, "Studies of Polaron Motion. Part 2: The Small Polaron," *Annals of Physics*, vol. 8, p. 343, 1959.

[38] H. Fröhlich, "Electrons in lattice fields," *Advances in Physics*, vol. 3, p. 325, 1954.

[39] J. T. Devreese, "Fröhlich polarons from 0D to 3D: concepts and recent developments," *Journal of Physics: Condensed Matter*, vol. 19, p. 255201, 2007.

[40] I. N. Hulea, S. Fratini, H. Xie, C. L. Mulder, N. N. Iossad, G. Rastelli, S. Ciuchi, and A. F. Morpurgo, "Tunable fröhlich polarons in organic single-crystal transistors," *Nature Materials*, vol. 5, p. 982, 2006.

[41] K. Hannewald, V. M. Stojanović, J. M. T. Schellekens, and P. A. Bobbert, "Theory of polaron bandwidth narrowing in organic molecular crystals," *Physical Review B*, vol. 69, p. 075211, 2004.

[42] K. Hannewald and P. A. Bobbert, "Ab initio theory of charge-carrier conduction in ultrapure organic crystals," *Applied Physics Letters*, vol. 85, p. 1535, 2004.

[43] K. E. Ziemelis, A. T. Hussain, D. D. C. Bradley, R. H. Friend, J. Rühe, and G. Wegner, "Optical spectroscopy of field-induced charge in poly(3-hexyl thienylene) metal-insulator-semiconductor structures: Evidence for polarons," *Physical Review Letters*, vol. 66, p. 2231, 1991.

[44] H. Sirringhaus, P. J. Brown, R. H. Friend, M. M. Nielsen, K. Bechgaard, B. M. W. Langeveld-Voss, A. J. H. Spiering, R. A. J. Janssen, E. W. Meijer, P. Herwig, and D. M. de Leeuw, "Two-dimensional charge transport in self-organized, high-mobility conjugated polymers," *Nature*, vol. 401, p. 685, 1999.

[45] I. G. Austin and N. F. Mott, "Polarons in crystalline and non-crystalline materials," *Advances in Physics*, vol. 50, p. 757, 2001.

[46] D. Emin, "Phonon-assisted jump rate in noncrystalline solids," *Physical Review Letters*, vol. 32, p. 303, 1974.

[47] E. Gorham-Bergeron and D. Emin, "Phonon-assisted hopping due to interaction with both acoustical and optical phonons," *Physical Review B*, vol. 15, p. 3667, 1977.

[48] R. A. Marcus, "Electron transfer in chemistry. theory and experiment," *Reviews of Modern Physics*, vol. 65, p. 599, 1993.

[49] M. Pope and C. E. Swenberg, *Electronic processes in organic crystals and polymers, 2nd ed.* New York, U. S. A: Oxford University Press, 1999.

[50] M. J. Lee, D. Gupta, N. Zhao, M. Heeney, I. McCulloch, and H. Sirringhaus, "Anisotropy of charge transport in a uniaxially aligned and chain-extended, high-mobility, conjugated polymer semiconductor," *Advanced Functional Materials*, vol. 21, p. 932, 2011.

[51] A. Miller and E. Abrahams, "Impurity conduction at low concentrations," *Physical Review*, vol. 120, p. 745, 1960.

[52] W. C. Germs, K. Guo, R. A. J. Janssen, and M. Kemerink, "Unusual thermoelectric behavior indicating a hopping to bandlike transport transition in pentacene," *Physical Review Letters*, vol. 109, p. 016601, 2012.

[53] J. J. Brondijk, W. S. C. Roelofs, S. G. J. Mathijssen, A. Shehu, T. Cramer, F. Biscarini, P. W. M. Blom, and D. M. de Leeuw, "Two-dimensional charge transport in disordered organic semiconductors," *Physical Review Letters*, vol. 109, p. 056601, 2012.

[54] A. J. Kronemeijer, V. Pecunia, D. Venkateshvaran, M. Nikolka, A. Sadhanala, J. Moriarty, M. Szumilo, and H. Sirringhaus, "Two-dimensional carrier distribution in top-gate polymer field effect transistors: correlation between width of density of localized states and Urbach energy," *Advanced Materials*, vol. 26, p. 728, 2014.

[55] K. Do, D. M. Huang, R. Fallera, and A. J. Moulea, "A comparative MD study of the local structure of polymer semiconductors P3HT and PBTTT," *Physical Chemistry Chemical Physics*, vol. 12, p. 14735, 2010.

[56] I. I. Fishchuk, A. Kadashchuk, S. T. Hoffmann, S. Athanasopoulos, J. Genoe, H. Bassler, and A. Kohler, "Unified description for hopping transport in organic semiconductors including both energetic disorder and polaronic contributions," *Physical Review B*, vol. 88, p. 125202, 2013.

[57] I. G. Lezama, M. Nakano, N. A. Minder, Z. Chen, F. V. D. Girolamo, A. Facchetti, and A. F. Morpurgo, "Single-crystal organic charge-transfer interfaces probed using Schottky-gated heterostructures," *Nature Materials*, vol. 11, p. 788, 2012.

[58] H. B. Callen, *Thermodynamics*. New York, U. S. A: Wiley, 1960.

[59] D. Emin, "Enhanced seebeck coefficient from carrier-induced vibrational softening," *Physical Review B*, vol. 59, p. 6205, 1999.

[60] M. Pfeiffer, A. Beyer, T. Fritz, and K. Leo, "Controlled doping of phthalocyanine layers by co-sublimation with acceptor molecules: A systematic Seebeck and conductivity study," *Applied Physics Letters*, vol. 3202, p. 73, November 1998.

[61] S. Baily and D. Emin, "Transport properties of amorphous antimony telluride," *Physical Review B*, vol. 73, p. 165211, 2006.

[62] T. L. Aselage, D. Emin, S. S. McCready, and R. V. Duncan, "Large enhancement of boron carbides' seebeck coefficients through vibrational softening," *Physical Review Letters*, vol. 81, p. 2316, 1998.

[63] D. Emin, *Wiley Encyclopedia of Electrical and Electronics Engineering Online*. New York, U. S. A: Wiley, 2013.

[64] H. Fritzsche, "A general expression for the thermoelectric power," *Solid State Communications*, vol. 9, pp. 1813–1815, 1971.

[65] G. S. Nolas, J. Sharp, and H. J. Goldsmid, "Thermoelectrics: Basic principles and new materials developments," *Springer Series in Materials Science*, 2001.

[66] K. P. Pernstich, B. Rössner, and B. Batlogg, "Field-effect-modulated Seebeck coefficient in organic semiconductors," *Nature Materials*, vol. 7, p. 321, February 2008.

[67] G. H. Kim, M. Shtein, and K. P. Pipe, "Thermoelectric and bulk mobility measurements in pentacene thin films," *Applied Physics Letters*, vol. 98, p. 093303, March 2011.

[68] R. Schmechel, "Hopping transport in doped organic semiconductors: A theoretical approach and its application to p-doped Zinc-phthalocyanine," *Journal of Applied Physics*, vol. 93, p. 4653, 2003.

[69] D. Emin, "Thermoelectric power due to electronic hopping motion," *Physical Review Letters*, vol. 35, p. 882, 1975.

[70] A. von Mühlenen, N. Errien, M. Schaer, M.-N. Bussac, and L. Zuppiroli, "Thermopower measurements on pentacene transistors," *Physical Review B*, vol. 75, p. 115338, March 2007.

[71] T. L. Aselage, D. Emin, and S. S. McCready, "Conductivities and Seebeck coefficients of boron carbides: Softening bipolaron hopping," *Physical Review B*, vol. 64, p. 054302, 2001.

[72] Z. S. Jan, R. H. Bube, and J. C. Knights, "Field effect and thermoelectric power on arsenic-doped amorphous silicon," *Journal of Electronic Materials*, vol. 8, p. 47, 1979.

[73] T. D. Moustakas, "Sputtered hydrogenated amorphous silicon," *Journal of Electronic Materials*, vol. 8, p. 391, 1979.

[74] N. F. Mott and E. A. Davis, *Electronic Processes in Non-Crystalline Materials.* Oxford, United Kingdom: Oxford University Press, 1971.

[75] O. Bubnova and X. Crispin, "Towards polymer-based organic thermoelectric generators," *Energy and Environmental Science*, vol. 5, p. 9345, 2012.

[76] A. I. Boukai, Y. Bunimovich, J. Tahir-Kheli, J.-K. Yu, W. A. Goddard, and J. R. Heath, "Silicon nanowires as efficient thermoelectric materials," *Nature*, vol. 451, p. 168, 2008.

[77] A. Rajagopal, S. Walavalkar, S. Chen, L. Guo, T. Gwinn, and A. Scherer, "Microscaled and nanoscaled platinum sensors," *Applied Physics Letters*, vol. 97, p. 133109, 2010.

[78] C.-H. Lee, G.-C. Yi, Y. M. Zuev, and P. Kim, "Thermoelectric power measurements of wide band gap semiconducting nanowires," *Applied Physics Letters*, vol. 94, p. 022106, 2009.

[79] Y. M. Zuev, W. Chang, and P. Kim, "Thermoelectric and magnetothermoelectric transport measurements of graphene," *Physical Review Letters*, vol. 102, p. 096807, 2009.

[80] J.-F. Chang and H. Sirringhaus, "Patterning of solution-processed semiconducting polymers in high-mobility thin-film transistors by physical delamination," *Advanced Materials*, vol. 20, p. 2825, 2010.

[81] I. McCulloch, M. Heeney, M. L. Chabinyc, D. DeLongchamp, R. J. Kline, M. Cölle, W. Duffy, D. Fischer, D. Gundlach, B. Hamadani, R. Hamilton, L. Richter, A. Salleo, M. Shkunov, D. Sparrowe, S. Tierney, , and W. Zhang, "Semiconducting thienothiophene copolymers: Design, synthesis, morphology, and performance in thin-film organic transistors," *Advanced Materials*, vol. 21, p. 1091, 2009.

[82] D. M. DeLongchamp, R. J. Kline, E. K. Lin, D. A. Fischer, L. J. Richter, L. A. Lucas, M. Heeney, I. McCulloch, and J. E. Northrup, "High carrier mobility polythiophene thin films: Structure determination by experiment and theory," *Advanced Materials*, vol. 19, p. 833, 2007.

[83] M. L. Chabinyc, M. F. Toney, R. J. Kline, I. McCulloch, and M. Heeney, "X-ray scattering study of thin films of poly(2,5-bis(3-alkylthiophen-2-yl)thieno[3,2-b]thiophene)," *Journal of the American Chemical Society*, vol. 129, p. 3226, 2007.

[84] D. de Leeuw, M. Simenon, A. Brown, and R. Einerhand, "Stability of n-type doped conducting polymers and consequences for polymeric microelectronic devices," *Synthetic Metals*, vol. 87, p. 53, 1997.

[85] H. Koide, Y. Nagao, K. Koumoto, Y. Takasaki, T. Umemura, T. Kato, Y. Ikuhara, and H. Ohta, "Electric field modulation of thermopower for transparent amorphous oxide thin film transistors," *Applied Physics Letters*, vol. 97, p. 182105, November 2010.

[86] G. Kim and K. Pipe, "Thermoelectric model to characterize carrier transort in organic semiconductors," *Physical Review B*, vol. 86, p. 085208, 2012.

[87] R. Coehoorn, W. F. Pasveer, P. A. Bobbert, and M. A. J. Michels, "Charge-carrier concentration dependence of the hopping mobility in organic materials with Gaussian disorder," *Physical Review B*, vol. 72, p. 155206, 2005.

[88] R. D. Pietro and H. Sirringhaus, "High resolution optical spectroscopy of air-induced electrical instabilities in n-type polymer semiconductors," *Advanced Materials*, vol. 24, p. 3367, 2012.

[89] H. Bronstein, D. S. Leem, R. Hamilton, P. Woebkenberg, S. King, W. Zhang, R. S. Ashraf, M. Heeney, T. D. Anthopoulos, J. de Mello, and I. McCulloch, "Indacenodithiophene-co-benzothiadiazole copolymers for high performance solar cells or transistors via alkyl chain optimization," *Macromolecules*, vol. 44, p. 6649, 2011.

[90] R. J. Kline, M. D. McGehee, E. N. Kadnikova, J. Liu, J. M. J. Freéchet, , and M. F. Toney, "Dependence of regioregular poly(3-hexylthiophene) film morphology and field-effect mobility on molecular weight," *Macromolecules*, vol. 38, p. 3312, 2005.

[91] H. Sirringhaus, M. Bird, and N. Zhao, "Charge transport physics of conjugated polymer field-effect transistors," *Advanced Materials*, vol. 22, p. 3893, 2010.

[92] R. Noriega, J. Rivnay, K. Vandewal, F. P. V. Koch, N. Stingelin, P. Smith, M. F. Toney, and A. Salleo, "A general relationship between disorder, aggregation and charge transport in conjugated polymers," *Nature Materials*, vol. 12, p. 1038, 2013.

[93] X. Zhang, H. Bronstein, A. J. Kronemeijer, J. Smith, Y. Kim, R. J. Kline, L. J. Richter, T. D. Anthopoulos, H. Sirringhaus, K. Song, M. Heeney, W. Zhang, I. McCulloch, and D. M. DeLongchamp, "Molecular origin of high field-effect mobility in an indacenodithiophene-benzothiadiazole copolymer," *Nature Communications*, vol. 4, p. 2238, 2013.

[94] W. Zhang, J. Smith, S. E. Watkins, R. Gysel, M. McGehee, A. Salleo, J. Kirkpatrick, S. A. T. Anthopoulos, M. Heeney, and I. McCulloch, "Indacenodithiophene semiconducting polymers for high-performance, air-stable transistors," *Journal of the American Chemical Society*, vol. 132, p. 11437, 2010.

[95] T. Lei, J.-H. Dou, Z.-J. Ma, C.-H. Yao, C.-J. Liu, J.-Y. Wang, , and J. Pei, "Ambipolar polymer field-effect transistors based on fluorinated isoindigo: High performance and improved ambient stability," *Journal of the American Chemical Society*, vol. 134, p. 20025, 2012.

[96] T. Lei, Y. Cao, Y. Fan, C.-J. Liu, S.-C. Yuan, and J. Pei, "High-performance air-stable organic field-effect transistors: Isoindigo-based conjugated polymers," *Journal of the American Chemical Society*, vol. 133, p. 6099, 2011.

[97] T. Lei, J.-H. Dou, and J. Pei, "Influence of alkyl chain branching positions on the hole mobilities of polymer thin-film transistors," *Advanced Materials*, vol. 24, p. 6457, 2012.

[98] J. Mei, D. H. Kim, A. L. Ayzner, M. F. Toney, and Z. Bao, "Siloxane-terminated solubilizing side chains: bringing conjugated polymer backbones closer and boosting hole mobilities in thin-film transistors," *Journal of the American Chemical Society*, vol. 133, p. 20130, 2011.

[99] D. Emin, *Polarons*. Cambridge, United Kingdom: Cambridge University Press, 2013.

[100] H. Sirringhaus, "25th anniversary article: Organic field-effect transistors: The path beyond amorphous silicon," *Advanced Materials*, vol. 26, p. 1319, 2014.

[101] J.-F. Chang, M. C. Gwinner, M. Caironi, T. Sakanoue, and H. Sirringhaus, "Conjugated-polymer-based lateral heterostructures defined by high-resolution photolithography," *Advanced Functional Materials*, vol. 20, p. 2825, 2010.

[102] R. A. Street, *Hydrogenated Amorphous Silicon*. Cambridge, United Kingdom: Cambridge University Press, 2005.

[103] M. Shahid, T. McCarthy-Ward, J. Labram, S. Rossbauer, E. B. Domingo, S. E. Watkins, N. Stingelin, T. D. Anthopoulos, and M. Heeney, "Low band gap selenophenediketopyrrolopyrrole polymers exhibiting high and balanced ambipolar performance in bottom-gate transistors," *Chemical Science*, vol. 3, p. 181, 2012.

[104] H.-W. Lin, W.-Y. Leeb, and W.-C. Chen, "Selenophene-DPP donoracceptor conjugated polymer for high performance ambipolar eld effect transistor and nonvolatile memory applications," *Journal of Materials Chemsitry*, vol. 22, p. 2120, 2012.

[105] A. J. Kronemeijer, E. Gili, M. Shahid, J. Rivnay, A. Salleo, M. Heeney, and H. Sirringhaus, "A selenophene-based low-bandgap donoracceptor polymer leading to fast ambipolar logic," *Advanced Materials*, vol. 24, p. 1558, 2012.

[106] C. L. Donley, J. Zaumseil, J. W. Andreasen, M. M. Nielsen, H. Sirringhaus, R. H. Friend, , and J.-S. Kim, "Effects of packing structure on the optoelectronic and charge transport properties in poly(9,9-di-n-octylfluorene-alt-benzothiadiazole)," *Journal of the American Chemical Society*, vol. 127, p. 12890, 2005.

[107] V. Podzorov, E. Menard, A. Borissov, V. Kiryukhin, J. A. Rogers, and M. E. Gershenson, "Intrinsic charge transport on the surface of organic semiconductors," *Physical Review Letters*, vol. 93, p. 086602, 2004.

[108] T. Sakanoue and H. Sirringhaus, "Band-like temperature dependence of mobility in a solution-processed organic semiconductor," *Nature Materials*, vol. 9, p. 736, 2010.

[109] V. Podzorov, E. Menard, J. A. Rogers, and M. E. Gershenson, "Hall effect in the accumulation layers on the surface of organic semiconductors," *Physical Review Letters*, vol. 95, p. 226601, 2005.

[110] B. Lee, Y. Chen, D. Fu, H. T. Yi, K. Czelen, H. Najafov, and V. Podzorov, "Trap healing and ultralow-noise hall effect at the surface of organic semiconductors," *Nature Materials*, 2013.

[111] Y. Takamatsu, T. Sekitani, and T. Someya, "Temperature dependence of hall effects in organic thin-film transistors on plastic films," *Applied Physics Letters*, vol. 90, p. 133516, 2007.

[112] J.-F. Chang, T. Sakanoue, Y. Olivier, T. Uemura, M.-B. Dufourg-Madec, S. G. Yeates, J. Cornil, J. Takeya, A. Troisi, and H. Sirringhaus, "Hall-effect measurements probing the degree of charge-carrier delocalization in solution-processed crystalline molecular semiconductors," *Physical Review Letters*, vol. 107, p. 066601, 2011.

[113] S. Wang, M. Ha, M. Manno, and C. D. F. C. Leighton, "Hopping transport and the Hall effect near the insulatormetal transition in electrochemically gated poly(3-hexylthiophene) transistors," *Nature Communications*, vol. 3, p. 1210, 2012.

[114] D. Waldmann, J. Jobst, F. Speck, T. Seyller, M. Krieger, and H. B. Weber, "Bottom-gated epitaxial graphene," *Nature Materials*, vol. 10, p. 357, 2011.

[115] B. Fluegel, R. N. Kini, A. J. Ptak, D. Beaton, K. Alberi, and A. Mascarenhas, "Shubnikov-de Haas measurement of electron effective mass in $GaAs_{1-x}Bi_x$," *Applied Physics Letters*, vol. 99, p. 162108, 2011.

[116] H. Ohta, Y. Masuoka, R. Asahi, T. Kato, Y. Ikuhara, K. Nomura, and H. Hosono, "Field-modulated thermopower in $SrTiO_3$-based field-effect transistors with amorphous $12CaO.7Al_2O_3$ glass gate insulator," *Applied Physics Letters*, vol. 95, p. 113505, September 2009.

[117] Y. Nagao, A. Yoshikawa, K. Koumoto, T. Kato, Y. Ikuhara, and H. Ohta, "Experimental characterization of the electronic structure of anatase TiO_2: Thermopower modulation," *Applied Physics Letters*, vol. 97, p. 172112, October 2010.

[118] G. Giri, E. Verploegen, S. C. B. Mannsfeld, S. Atahan-Evrenk, D. H. Kim, S. Y. Lee, H. A. Becerril, A. Aspuru-Guzik, M. F. Toney, and Z. Bao, "Tuning charge transport in solution-sheared organic semiconductors using lattice strain," *Nature*, vol. 480, p. 504, 2011.

[119] A. S. Eggeman, S. Illig, A. Troisi, H. Sirringhaus, and P. A. Midgley, "Measurement of molecular motion in organic semiconductors by thermal diffuse electron scattering," *Nature Materials*, vol. 12, p. 1045, 2013.

[120] C. B. Nielsen, M. Turbiez, and I. McCulloch, "Recent advances in the development of semiconducting DPP-containing polymers for transistor applications," *Advanced Materials*, vol. 25, p. 1859, 2013.

[121] L. Biniek, B. C. Schroeder, C. B. Nielsen, and I. McCulloch, "Recent advances in high mobility donor-acceptor semiconducting polymers," *Journal of Materials Chemistry*, vol. 22, p. 14803, 2012.

[122] F. Zhang, Y. Hu, T. Schuettfort, C. an Di, X. Gao, C. R. McNeill, L. Thomsen, S. C. B. Mannsfeld, W. Yuan, H. Sirringhaus, , and D. Zhu, "Critical role of alkyl chain branching of organic semiconductors in enabling solution-processed n-channel organic thin-film transistors with mobility of up to 3.50 cm^2V^{-1} s^{-1}," *Journal of the American Chemical Society*, vol. 135, p. 2338, 2013.

[123] H. N. Tsao, D. M. Cho, I. Park, M. R. Hansen, A. Mavrinskiy, D. Y. Yoon, R. Graf, W. Pisula, H. W. Spiess, and K. Mllen, "Ultrahigh mobility in polymer field-effect transistors by design," *Journal of the American Chemical Society*, vol. 133, p. 2605, 2011.

[124] P. Sonar, S. P. Singh, Y. Li, M. S. Soh, and A. Dodabalapur, "A low-bandgap diketopyrrolopyrrole-benzothiadiazole-based copolymer for high-mobility ambipolar organic thin-film transistors," *Advanced Materials*, vol. 22, p. 5409, 2010.

[125] J. D. Yuen, J. Fan, J. Seifter, B. Lim, R. Hufschmid, A. J. Heeger, and F. Wudl, "High performance weak donoracceptor polymers in thin film transistors: Effect of the acceptor on electronic properties, ambipolar conductivity, mobility, and thermal stability," *Journal of the American Chemical Society*, vol. 133, p. 20799, 2011.

[126] L. Zhang, C. He, J. Chen, P. Yuan, L. Huang, C. Zhang, W. Cai, Z. Liu, and Y. Cao, "Bulk-heterojunction solar cells with benzotriazole-based copolymers as electron donors: Largely improved photovoltaic parameters by using PFN/Al bilayer cathode," *Macromolecules*, vol. 43, p. 9771, 2010.

[127] A. Balan, D. Baran, and L. Toppare, "Benzotriazole containing conjugated polymers for multipurpose organic electronic applications," *Polymer Chemistry*, vol. 2, p. 1029, 2011.

[128] S. Kowalski, S. Allard, and U. Scherf, "Synthesis of poly(4,4-dialkyl-cyclopenta[2,1-b:3,4-b']dithiophene-alt-2,1,3-benzothiadiazole) (PCPDTBT) in a direct arylation scheme," *Macro Lett*, vol. 1, p. 465, 2012.

[129] J.-R. Pouliot, L. G. Mercier, S. Caron, and M. Leclerc, "Accessing new DPP-based copolymers by direct heteroarylation polymerization," *Macromolecular Chemistry and Physics*, vol. 214, p. 453, 2013.

[130] Q. Guo, J. Dong, D. Wan, D. Wu, and J. You, "Modular establishment of a diketopyrrolopyrrole-based polymer library via Pd-catalyzed direct C-H (hetero)arylation: a highly efficient approach to discover low-bandgap polymers," *Macromolecular Rapid Communications*, vol. 34, p. 522, 2013.